Propeller Design for Conceptual Turboprop Aircraft

Y.A.P. Teeuwen

Flight Performance and Propulsion

TU Delft

Cover image: Guittet, A. http://mycockpitview.com/

Propeller Design for Conceptual Turboprop Aircraft

by

Y.A.P. Teeuwen

in partial fulfilment of the requirements for the degree of

Master of Science in Aerospace Engineering at the Delft University of Technology,

to be defended publicly on Thursday October 12, 2017 at 01:00 PM.

Student nr.:	4026152	
Thesis registration nr.:	164#17#MT#FPP	
Supervisor:	Dr. ir. R. Vos	
Thesis committee:	Prof. dr. ir. L. L. M. Veldhuis,	TU Delft
	Dr. ir. R. Vos,	TU Delft
	Dr. ir. C. J. Simão Ferreira,	TU Delft

TU Delft

Preface

This report marks the conclusion of my Master of Science program at the faculty of Aerospace Engineering. It concerns propeller design in the conceptual design phase of turboprop airliners. Propellers remain an interesting choice for aircraft propulsion, due to their high propulsive efficiency when compared to alternative forms of propulsion. The findings of this research show the implications of propeller design choices on aircraft maximum take-off mass.

This report came to fruition with the support of others, to whom I wish to extend my gratitude. I would like to thank Roelof Vos for his guidance and support during this research project and the further committee members Leo Veldhuis and Carlos Simão Ferreira for their time and effort in assessing this report. A further acknowledgement of Tom Stokkermans and Peter Klein for their insights in propeller theory as well as Malcolm Brown and Jelle Boersma for their contributions to my programming skills and comprehension of the Initiator design software. Finally, to the friends and loved ones with a special mention of my parents and girlfriend. I have a deep appreciation of your love and support which allowed me to reach this highlight in my accomplishments so far.

Yorick Teeuwen
Delft, October 2017

Abstract

In the conceptual design phase of a turboprop aircraft, the configuration is determined and primary components like the wing, fuselage and propulsion are sized. Exact subsystem performance remains unknown. Propeller performance is estimated to size the aircraft propulsion.

This thesis explores the consequences on the aircraft's maximum take-off mass if the propeller estimation is removed in favor of a higher fidelity design approach. The influence is determined by implementing an optimization routine which minimizes aircraft maximum take-off mass by adjusting the propeller design.

A rapid conceptual design tool is used to establish the interdependence between propeller and aircraft: 'The Aircraft Design Initiator'. This tool is able to quickly conceive realistic aircraft designs to investigate the effect of new technologies and aircraft configurations. The Initiator is employed to create a design objective. This objective contains the information needed to achieve an optimum between propeller aerodynamic efficiency and its implication on the mass of the propulsion unit. These two factors determine the fuel required for the mission, as well as the mass of the propeller engine combination. In turn, these masses impact the maximum take-off mass of the aircraft.

To establish a propeller design, a set of tools is developed. Aerodynamic performance is calculated from blade element momentum theory. Mass estimation is performed by a class II sizing approach. A limited structural tool is used to size the propeller blade root. Propeller optimization is performed with two strategies: a gradient descent optimization and a genetic algorithm. It is concluded that the propeller design space features a lot of local minima and is poorly suited for gradient based optimization. Genetic optimization is better suited for propeller design. This strategy results in certain conclusions regarding propeller design influences on the aircraft's maximum take-off mass.

The influence of the propeller on the maximum take-off mass is determined to be less than 1% compared to initial performance estimations. The applicability to conceptual aircraft design is therefore limited. However, the results do clearly show the influence of the propeller design parameters on the aircraft's maximum take-off mass.

Contents

List of Figures

List of Tables

Nomenclature

Acronyms

Symbol	Description	Units
AEO	All engines operative	-
BEM	Blade element momentum	-
FAR	Federal aviation regulations	-
MTOM	Maximum take-off mass	kg
OEI	One engine inoperative	-
OEM	Operative empty mass	kg
PSFC	Specific fuel consumption	$\frac{\text{kg}}{\text{kW hr}}$
SFC	Specific fuel consumption	$\frac{\text{kg}}{\text{N hr}}$
SHP	Shaft horse power	hp
TLR	Top level requirements	-
TOFL	Take-off field length	m

Greek Symbols

Symbol	Description	Units
α	Angle of attack	deg/rad
α_{zl}	Airfoil zero lift angle of attack	deg/rad
β	Geometric airfoil section pitch angle	deg/rad
β_p	Geometric blade pitch angle	deg/rad
γ	Ratio of specific heats	-
η_p	Propulsive efficiency	-
κ	Technology factor for transonic performance	-
μ_k	Kaplan correction	-
μ_{PG}	Prandtl-Glauert correction	-
ρ	Density	$\frac{\text{kg}}{\text{m}^3}$
σ	Normal stress	Pa
σ_s	Propeller solidity	-
ϕ	Inflow angle	rad
Ω, ω	Rotational rate	rad s^{-1}

Roman Symbols

Symbol	Description		Units
AR	Aspect ratio		-
a	Acceleration		$\frac{\mathrm{m}}{\mathrm{s}^2}$
B	Number of blades		-
b	Wingspan		m
C	Climb gradient		-
C_D	Coefficient of drag		-
c_d	Section drag coefficient		-
C_L	Coefficient of lift		-
c_l	Section lift coefficient		-
C_P	Coefficient of power	$\frac{P}{\rho n^3 D_p^5}$	-
C_T	Coefficient of thrust	$\frac{T}{\rho n^2 D_p^4}$	-
$c_{d\mathrm{min}}$	Section minimum drag coefficient		-
c_{d_0}	Section zero lift drag coefficient		-
$c_{l\mathrm{md}}$	Lift coefficient at minimum drag		-
C_{l_i}	Airfoil camber		-
D	Drag		N
D_p	Propeller diameter		m
E	Elastic modulus		Pa
e	Oswald factor		-
F	Tip loss factor		-
GR	Gear ratio		-
h_f	Height vertical stabilizer		m
J	Propeller advance ratio	$\frac{V}{nD_p}$	-
K	Surface durability		$\frac{\mathrm{m}^2}{\mathrm{s}^2}$
k_p	Drag due to lift parameter		-
L	Lift		N
l_f	Moment arm fuselage		m
l_p	Moment arm propeller		m
M	Mach number		-
M_{dd}	Drag divergence Mach number		-
n	Rotations per second		s^{-1}
N_{pl}	Number of planetary gears		-

P	Power	W
p	Pressure	Pa
$P_{DS,\text{limit}}$	Power limit at reference rotor speed	hp
Q	Torque	N m
q	Dynamic pressure	Pa
R	Aircraft range	km
R	Propeller radius	m
r	Radial position	m
Re	Reynolds Number	-
S	Wing area	m^2
t	Airfoil thickness	m
U_∞	Free stream speed	$\frac{m}{s}$
V	Velocity of aircraft	$\frac{m}{s}$
v_i	Induced velocity	$\frac{m}{s}$
W	Aircraft weight	N
X	location of separation	-
A	Area	m^2
I	Second moment of area	m^4
M	Moment	N m

1 Introduction

Screws that move a fluid have been in use for a long time. Among the engineers who have studied them are legendary names such as Archimedes, da Vinci and the Wright brothers. Screws used for propulsion, propellers, were first used in ships and later were the first successful propulsion method for aircraft.

Traditionally, propeller design is performed by specialist companies. A propeller is typically not designed by the aircraft manufacturer. A current generation turboprop aircraft, the ATR72, has the same propeller installed in several different variants of its design. The Hamilton Standard 568F propeller is installed in variants that range in maximum take-off mass (MTOM) and take-off power from 17900 kg with 1980 SHP to 22800 kg with 2475 SHP for the ATR42-400 and the ATR72-600 respectively[1]. That is a difference of roughly 25% in MTOM and SHP. The large variation in power absorbed means the propeller operates under a range of load factors and thus it can be assumed that the propeller is not optimized for a specific aircraft. This research aims to investigate the improvements that are possible when a propeller and aircraft are designed in unison. An optimal propeller design is thereby defined as a design that results in a minimal aircraft maximum take-off mass.

The Flight Performance and Propulsion group at Delft University of Technology has a design tool available that can rapidly establish conceptual aircraft designs. This software tool named 'The Aircraft Design Initiator', or the Initiator for short, allows the effects of the propeller on the aircraft design to be established. With the ability to predict the influence of the propeller on the aircraft design, an optimization routine can be employed to establish the optimal propeller for a specific aircraft.

In this Master thesis, the state-of-the-art in propeller modeling, conceptual aircraft design and propulsion integration will be used to develop a method for optimizing a propeller design for a minimal aircraft maximum take-off mass.

Research goal and questions

In this thesis the necessary knowledge and tools are obtained to design a propeller for a conceptual turboprop aircraft. The design of a propeller determines its efficiency at critical flight conditions. The efficiency achieved for these flight conditions determines either the power required from or the fuel burned by the engine. The fuel and engine mass influence the aircraft's MTOM. This relation will be further elaborated in Chapter 2.

Design handbooks state to assume a propeller efficiency for these critical conditions in order to size the aircraft. For the critical climb condition a propulsive efficiency between 73% [2, p. 165] and 80%[3, p. 135 Part I] is stated. For the cruise condition an efficiency of 80%[4, p. 19] to 85%[2, p. 153],[3, p. 165 Part I] is to be assumed. These assumptions for the propeller are traditionally used for conceptual aircraft design and will be evaluated against the calculated propulsive efficiencies of an optimized propeller.

In order to study what an optimum propeller design delivers in terms of improvement to the performance of the aircraft, the maximum take-off mass of the aircraft design is used as a performance indicator. The goal is to obtain a feasible aircraft design that satisfies its design requirements and constraints with its maximum take-off mass as low as possible. A propeller design that results in a minimum take-off mass can be defined as an optimum propeller design for its aircraft and mission. This optimization routine is guided by the following research questions:

What is the influence of the propeller design parameters on the sizing of the propulsive unit and the maximum take-off mass of a conceptual turboprop aircraft?

What propeller design parameters are relevant and feasible to include in the propeller design space?

What level of of improvement can be expected from a propeller and propulsion optimization routine?

Scope of thesis

It is not feasible to incorporate all disciplines of propeller design in this thesis. Therefore, some aspects of propeller design are neglected. Additionally, the work performed in this research is intended to be useful for further development of the Initiator. This imposes a time constraint on the optimization routines of this thesis. As a consequence, aspects of propeller design are performed with lower fidelity tools. Propeller design elements within the scope of this research consist of: aerodynamic analysis, structural analysis and mass estimation. Further neglections and simplifications specific to these individual aspects are stated as they become apparent. Relevant but excluded from design consideration is propeller noise.

2

Methodology

This chapter is started with a brief discussion on conceptual aircraft design with the Initiator. This is followed by an investigation on how the propeller design influences the propulsive mass and the fuel mass of a conceptual turboprop aircraft and thereby the aircraft's maximum take-off mass.

With the influence of the propeller on the propulsive mass and the fuel mass known, a methodology for propeller design is made. The aim of this research is to find a propeller design methodology which results in minimal aircraft MTOM. The dependence of the propulsive mass and fuel mass on the MTOM is made into a design objective. With the influence of propeller design on these two masses known, the influence of propeller design on MTOM is determined.

The chapter is closed with the establishment of several optimization strategies to answer the research questions posed in the introduction.

2.1. Conceptual design of an aircraft with the Initiator with emphasis on the propulsive unit

The design of a propeller powered aircraft in the Initiator is an iterative methodology where weights, geometry and aerodynamic properties are calculated and reiterated until a feasible and consistent aircraft design is found. A schematic representation of this routine is depicted in the N2 chart of Figure 2.1.

The structure of the Initiator is such that the power required from the propulsive unit and thereby its size is calculated by means of a wing power loading diagram (further elaborated in Section 2.1.2). The mass of the engine is calculated from the power requirement. Inside a class II weight convergence indicated by the orange loop of Figure 2.1, the fuel mass is determined by the Brequet range equation and a lost range methodology. The sizing of the propulsive unit and calculation of fuel mass within the class II design loop is simplified to illustrate the explanation above. Only the modules and variables directly pertaining to the propulsive unit mass and fuel mass are depicted in Figure 2.2.

Further convergence loops (indicated in the green and blue loops) feature a more intricate method of calculating the fuselage, fuel and wing mass. These higher fidelity methods are not used. For this research, only the orange class II design loop is considered and will be used to create the propeller design space.

2.1.1. Calculation of mission fuel weight

Fuel mass is determined in the class I weight estimation module. The fuel needed for the mission is determined by standards set by the ESDU. The fuel mass is determined in fractions of the weight of the total aircraft. The fuel required to meet the desired range R set by the aircraft designer can be derived from the Breguet range equation:

$$R = \frac{V}{g}\frac{1}{\mathrm{SFC}}\frac{L}{D}\ln\left(\frac{W_i}{W_f}\right) \tag{2.1}$$

The fuel mass is determined from the Breguet range equation by supplying the cargo mass and range from top level requirements (TLR) set by the designer. The operative empty mass and aerodynamic parameters are initially supplied from reference data and later reiterated from the current design. The difference in initial weight W_i and final weight W_f is equal to the fuel burned in cruise.

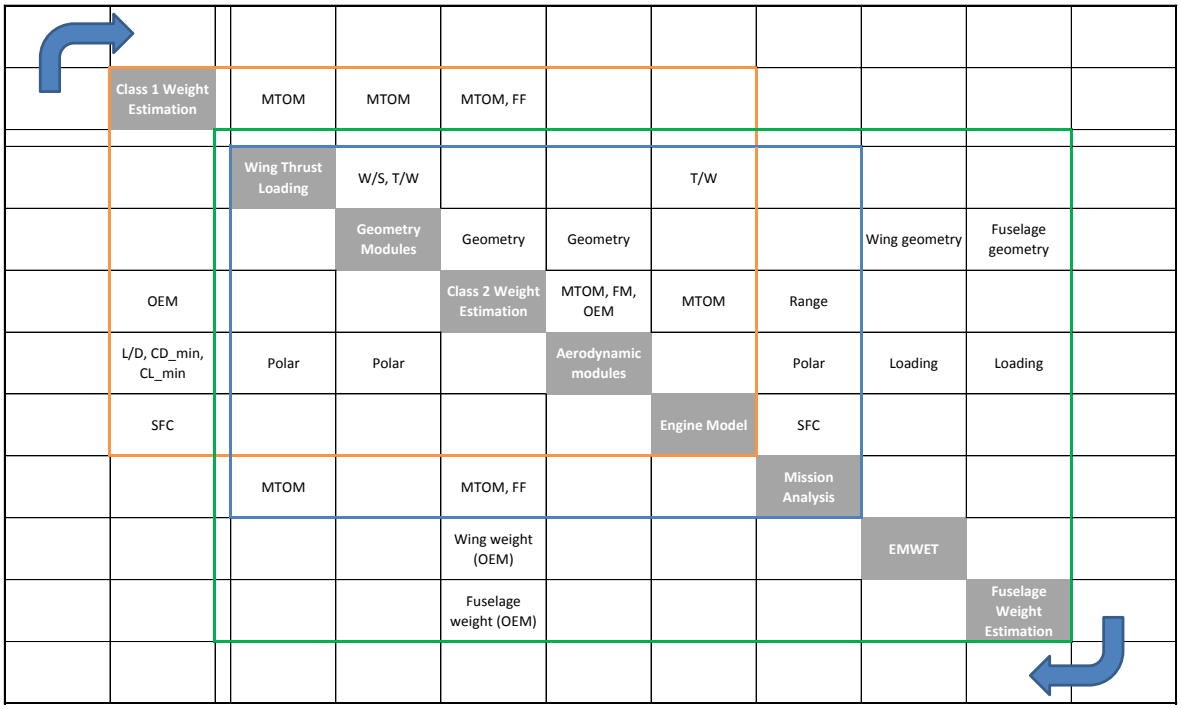

Figure 2.1: Convergence N2 diagram showing main aircraft parameters between modules during a design convergence run.[5]

Determining the fuel mass from the SFC is generally a good approximation for turbofan aircraft as the thrust and fuel flow do not vary rapidly with forward speed. For propeller aircraft the thrust produced by the power plant is a function of airspeed. The shaft power produced at a given height varies with air speed as well, however to a lesser degree then the thrust. Therefore, it is more appropriate to define the specific fuel consumption as the fuel flow per unit engine output-shaft power PSFC $\left(\frac{\text{kg}}{\text{kW h}}\right)$. [6] The rewritten Brequet range equation shows the propulsive efficiency in cruise and the PSFC impacting the fuel needed to complete the mission with the range R in km:

$$R = \frac{\eta_{p,\,\text{cruise}}}{g} \frac{3600}{\text{PSFC}} \frac{L}{D} \ln\left(\frac{W_i}{W_f}\right) \tag{2.2}$$

The fuel needed for a mission is not only used to obtain the cruise range required. A portion of fuel is used for climb take-off, landing, diversion and taxi. These fractions can be calculated by the lost range formulation derived by the ESDU. The lost range due to climb and decent is derived from the change in energy due to a change in altitude; the energy needed for a unit mass to change a unit length in height. This change in energy height is used in a empirical relation for turboprops together with the weight fraction of cruise fuel to get the fraction of fuel required for these flight movements. [7]

2.1.2. Calculation of the thrust requirement, engine size and propulsive mass

Top level requirements of the aircraft performance dictate the engine to aircraft and wing to aircraft matching[8]. This is done by decomposing the main forces on the aircraft and calculating the required wing and engine size for a desired performance. The performance constraints are set by regulatory agencies and the aircraft manufacturer. These requirements dictate a minimum climb and take-off performance. Certain climb gradients must be achieved for given aircraft configurations often with one engine inoperative (OEI). To take these requirements into account during the conceptual design phase, the aircraft is simplified to a point mass. Upon this mass the simplified forces of lift, drag, thrust and weight are decomposed. The required combination of wing area and thrust can be calculated to attain the following requirements:

- For different aircraft configurations, climb gradients or climb rates
- Turn rate (mostly military)

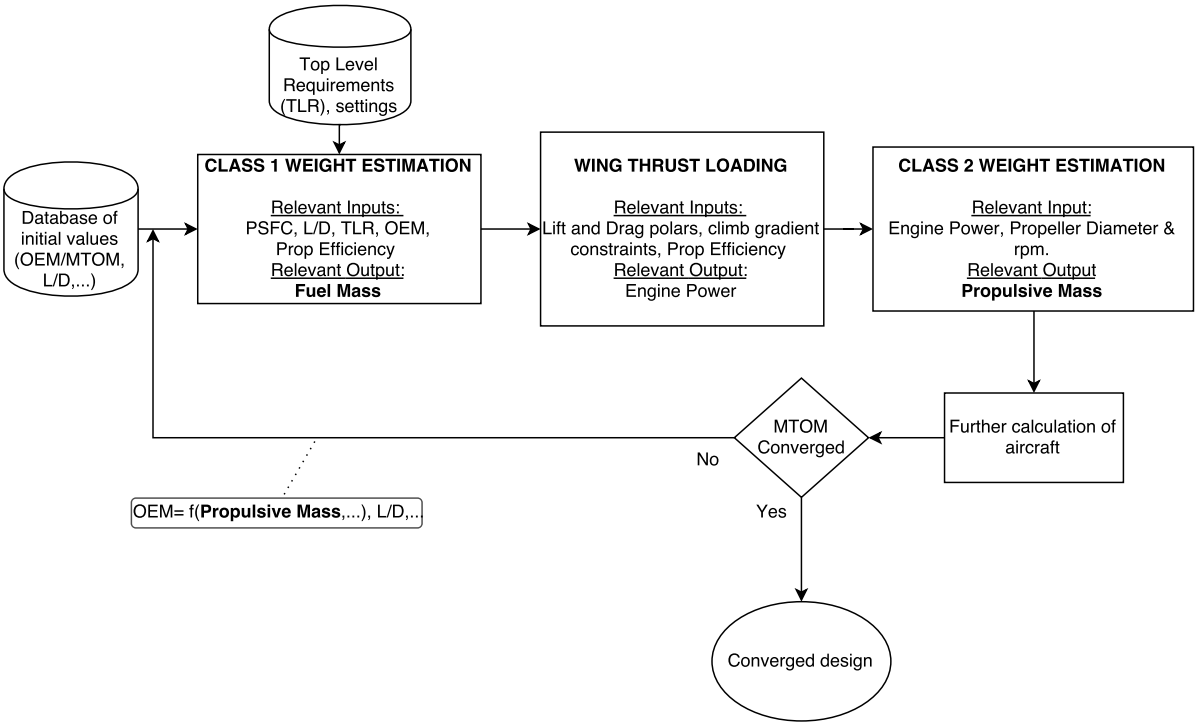

Figure 2.2: Simplified class II design convergence for a turboprop aircraft showing the influence of the propulsive unit on the aircraft mass.

- Cruise speed
- Take-off field length
- Engine out altitude capability (applicable to long range cruise over water or isolated areas)
- Landing field length

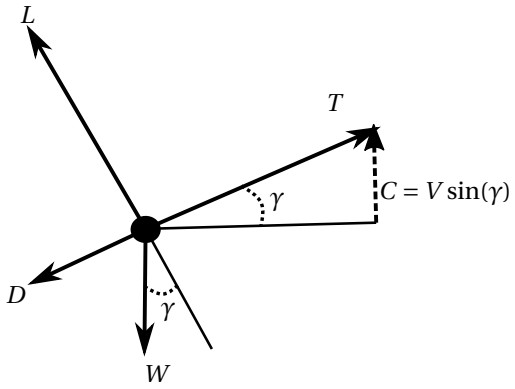

Figure 2.3: Free body diagram of a point mass upon which the main forces of flight act: lift, drag, weight and thrust.

The forces acting upon the aircraft, simplified to a point mass are sketched in Figure 2.3 with γ the climb angle. When the forces are decomposed the following derivation can be made:

$$T - D - W\sin(\gamma) = 0 \quad \overset{\text{linearize}}{\Rightarrow} \quad \frac{T-D}{W} = \gamma \tag{2.3}$$

$$\frac{T}{W} = \frac{D}{W} + \gamma \quad \Rightarrow \quad \frac{T}{W} = \frac{C_D}{C_L} + \gamma \tag{2.4}$$

For propeller powered aircraft the convention is not to size the engines to thrust as this varies with airspeed. Rather the take-off power required from the engine is used to select an engine size. From the equation $\eta_p P = TV$ the required engine power can be found with the following equation:

$$\frac{W}{P} = \eta\left(\sqrt{\frac{2W}{S\rho C_L}}\frac{C_D}{C_L} + C\right)^{-1} \tag{2.5}$$

Climb gradient constraints for jet and propeller aircraft are the same and rely on the same aircraft parameters C_L, C_D but due to convention of expressing the thrust required in engine power an extra parameter is included: the propulsive efficiency of the propeller at the specific flight segment. For all flight segments and constraints one constraint is leading and determines the minimum engine size. The engine power is determined from Equation (2.5), subsequently the engine mass is derived from the engine power. Together with the mass of the propeller and the auxiliaries the mass of the propulsive unit is determined. The wing area is determined from the landing field length requirement.

In this thesis when 'climb' or $\eta_{p,\,\text{climb}}$ is used to define a flight section the critical climb gradient condition is meant. The climb gradient condition is the critical sizing condition in most cases. However, it is possible that the cruise speed or the take-off field length is the constraining condition for the engine size. The sizing of the power plant when the take-off field length is the critical condition is discussed in Section 2.2. These conditions are considered in this thesis. Other sizing conditions that were itemized at the beginning of the subsection are not considered.

Note: The speed is derived from the maximum lift coefficient. This is not valid when a specified gradient must be attained at a dictated flight speed[2].

2.1.3. Forming the design objective

From Equation (2.5) and Equation (2.2) it is concluded that the aircraft mass resulting from the propulsion system is a function of three propulsion parameters. The three parameters of the propulsion department acting on the aircraft are: the PSFC and two propeller propulsive efficiencies during cruise (sizing fuel mass) and, during the critical condition condition sizing the mass of the propulsive unit.

In this thesis the PSFC is kept constant for a change in engine size. According to Walsh and Fletcher [9, p. 147]: "When all geometry of a gas turbine is scaled by a factor of two, mass flow and thrust/power increase by a factor of 4, rotational speed will decrease by a factor of two and SFC remains unchanged". In reality, it is noticed that PSFC decreases for an increase in engine size. This is because, among other reasons, an increased engine size allows relative tip clearances of the turbine and compressor to be decreased. The trend of decreasing PSFC with engine size can be found in Jane's aero engines [10].

It is established that the aircraft mass during conceptual design with regards to propulsion is dependent on the propulsive efficiency of the propeller for two critical conditions. First, the efficiency during cruise dictating the fuel mass required for the mission and second, the propulsive efficiency during the critical cruise/climb/take-off condition dictating the power required of the engine and thereby the propulsive mass. A propeller design that yields a high efficiency in one condition may be detrimental for performance in another condition. The objective of the thesis is to find the optimum propeller design which results in a minimum in MTOM.

The design objective for this optimization can therefore be formed by varying the propulsive efficiency for the two conditions and repeatedly converging to a consistent aircraft design. By doing so a surface of consistent aircraft designs with varied fuel and propulsive unit masses results. The objective is shown in Figure 2.4.

2.2. Optimization routine

The optimization objective consist of a number of class II weight estimation convergences for a variety of fuel masses $f(\eta_{p,\,\text{cruise}})$ and propulsive unit masses $f(\eta_{p,\,\text{climb}})$ or $f(\eta_{p,\,\text{take-off}})$ or $f(\eta_{p,\,\text{cruise}})$. Each convergence is a feasible turboprop aircraft design apart from propulsive efficiencies that may not be achievable or are too conservative. Each point on the objective indicates an aircraft with its requirements for thrust and specific geometry. The trust requirements are plotted in Figure 2.5a and 2.5b.

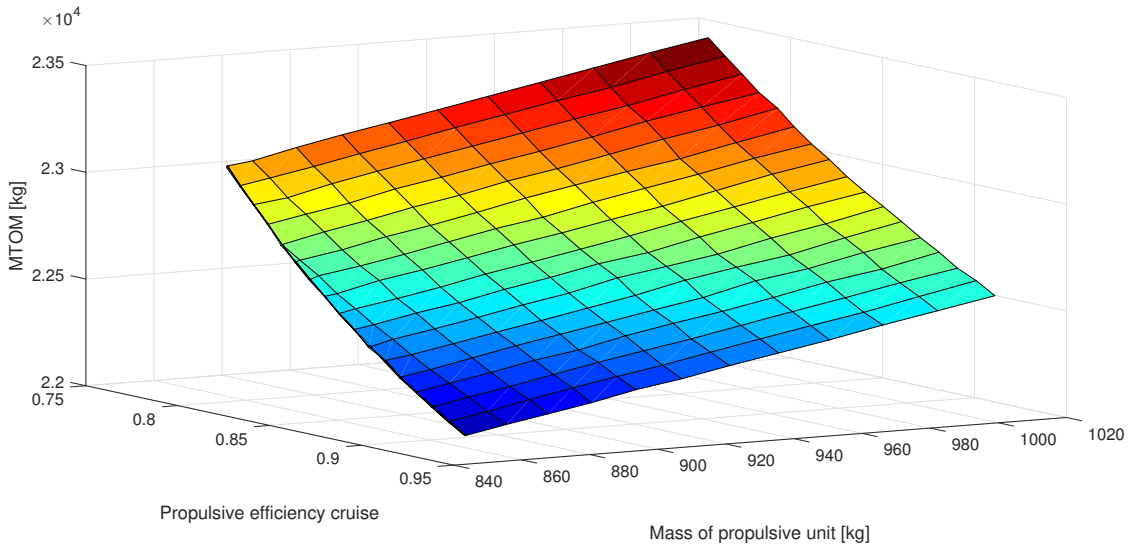

Figure 2.4: Design objective for the ATR72-600, build from class II design converge runs in the Initiator. The $\eta_{p,\,\text{cruise}}$ is varied from 0.75 to 0.95, the $\eta_{p,\,\text{climb}}$ is varied from 0.65 to 0.85.

The optimization strategies developed in this section will determine the critical sizing condition for the propulsive unit and find the accompanying propulsive efficiencies that will result in a minimal MTOM. For each condition a separate optimization routine is justified.

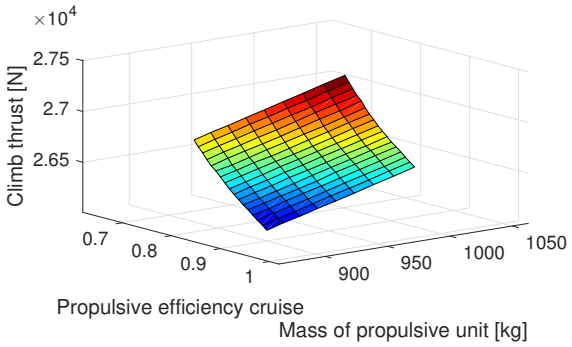

(a) Climb gradient thrust constraint OEI, sea level.

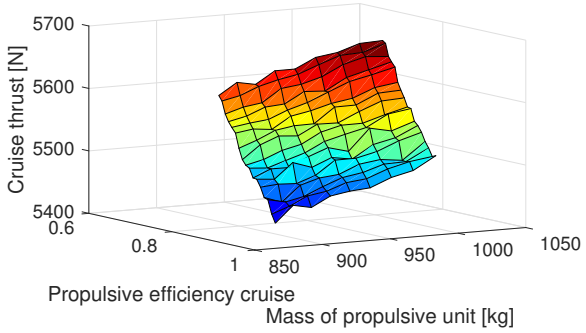

(b) Cruise thrust constraint per engine, cruise altitude.

Figure 2.5: Thrust constraints for the ATR72-600, build from class II design converge runs in the Initiator. The $\eta_{p,\,\text{cruise}}$ is varied from 0.75 to 0.95, the $\eta_{p,\,\text{climb}}$ is varied from 0.65 to 0.85.

Case 1 - Climb gradient constrained

The aircraft is in a critical climb condition. The condition and aircraft configuration are determined from a power loading diagram. In this diagram the required climb gradients for different conditions and aircraft configurations are plotted. The condition that sizes the power plant is used. In this condition the aircraft typically experiences an engine failure. Federal aviation regulations (FAR) dictate a minimum climb gradient that must be obtained by the aircraft. This results in a minimum thrust requirement at a single point in time in order to obtain the climb gradient. A propeller is designed such that the thrust constraint set by the FAR is obtained. The power required by the propeller for that condition is the sizing condition for the power plant. The pitch angle β_p of the propeller in the climb condition is determined as an optimization variable. The pitch angle in cruise is set by the user.

Case 2 - Take-off field length constrained

The aircraft experiences an engine failure during the take-off run at the decision speed. The aircraft must take-off and clear a 35 ft obstacle within its certified take-off field length. In order to accomplish this the

thrust delivered over the take-off run must be such that the aircraft has accelerated to a safe speed and has reached minimum obstacle height at the end of the take-off field length. The magnitude of thrust will vary over the take-off run and is a function of power and propeller design. This means that not one condition for the power plant is sizing. Rather the combination of power available and propeller efficiency by which power is converted to thrust determines the thrust delivered over the run. Contrary to Case 1, maximum power is not used at one condition for one pitch angle.

For Case 2, the power of the propulsion unit is an optimization variable. The power is an independent variable of the propeller design. This means that the torque required by the propeller for optimal thrust in that condition may not be available from the power plant or conversely the torque delivered to the propeller is too high for optimal thrust. For instance: the power is set by the pilot at 100% for the take-off. The propeller pitch mechanism is scheduled such that the propeller blades are pitched to absorb all available power. This may mean that the blade will over pitch, stalling part of the blade (early in the take-off) or it may mean that not enough torque is available to pitch to an angle which is optimal. Because the power is an independent variable. The propeller pitch is scheduled so that all the torque delivered by the power plant is absorbed by the propeller, independent of what may be the optimal pitch angle. The power of the propulsive unit is an optimization variable instead of the propeller pitch angle in climb. Appendix A elaborates on why the pitch angle mechanism is incorporated as an optimization variable for Case 1 and how the pitch scheduling mechanism is incorporated in the design tool for Case 2. The reader is encouraged to read this appendix if uncertainty regarding the propeller blade pitch angle remains.

The optimization of Case 1 is less computationally expensive due to the optimization having to be performed for two conditions: climb and cruise. Case 2 requires an optimization over the take-off run. The integral of the take-off run simplified in Equations (2.6)–(2.8) is not readily solved. Rather the integral can be approximated by segmenting the take-off run. For each segment of δt the aircraft advances a distance dis. The state of the aircraft can be calculated by simplified Equations (2.9)–(2.11). The thrust, drag and other forces on the aircraft are established for each δt and so a good approximation of the take-off run is made. The thrust is updated for an interval, the optimization is dependent on each trust interval and hence will be more computationally expensive. The optimization routine for Case 1 is dependent on two flight conditions. For Case 2 there are many flight conditions in addition to the two of Case 1. The amount of flight conditions can be set by altering the computation interval of the thrust during take-off.

$$\text{TOFL} = \int V\,dt \tag{2.6}$$

$$V = \int a\,dt \tag{2.7}$$

$$a = \frac{T - D}{\text{MTOM}} \tag{2.8}$$

$$\text{dis}(i+1) = \text{dis}(i) + V(i)\delta t \tag{2.9}$$

$$V(i+1) = V(i) + a\delta t \tag{2.10}$$

$$a = \frac{T - D}{\text{MTOM}} \tag{2.11}$$

The objective function $J(\overline{x})$ for Case 1 and Case 2 will be minimized for the variable $\text{MTOM}(\overline{x})$. The minimization case is subject to non-linear equality constraint $h(\overline{x})$ and inequality constraints $\overline{g}(\overline{x})$:

$$\begin{aligned} &\text{minimize } J(\overline{x}) = \text{MTOM}(\overline{x}) \\ &\text{subject to:} \\ &\qquad h(\overline{x}) = 0 \\ &\qquad \overline{g}(\overline{x}) \leq 0 \end{aligned} \tag{2.12}$$

The optimization objective function does not vary between the cases. The process flow of the optimization cases is given in Figure 2.7. The constraints and design vector do differ. Not only between optimization cases but also between optimization strategies.

2.2.1. Optimization strategies

The optimization for both conditions is preferably solved by a gradient based algorithm. This limits computation time, however, a global optimum may not be found. Therefore, a global optimization technique is also

considered. For the global optimization strategy a genetic algorithm is selected. Although it may not be possible to prove a global optimum is reached, a global optimization technique will provide information about the optimization landscape.

2.2.2. Optimization variables and constraints for the different strategies

Summarizing the previous sections: two optimization cases are identified; Case 1 which is constraint in climb thrust by its critical climb condition, Case 2 which is constraint in climb thrust by its critical climb condition and the take-off field length. Two optimization strategies are selected: a fast local optimization with a gradient based algorithm and, a computationally expensive global optimization with a genetic algorithm.

Mathematical description of optimization constraints and variables

The geometric parameterization of a propeller blade consist of radially dividing the blade into sections. Starting from the radial location of the hub which is set by the user, i sections are defined towards the tip. For each section the chord length and the β-angle is a design variable. The theory of the aerodynamic blade sections is discussed in Section 3.1.1. The diameter and the rotational rate of the propeller which have a relation between the propeller aerodynamic efficiency, the maximum tip Mach number and the weight of the propulsive unit are a design variable in every optimization case. The design variables used in every optimization are:

$$\overline{x} = \left[l_{\text{chord}}(1:i) \;\; \beta(1:i) \;\; D_p \;\; \text{rpm} \right] \tag{2.13}$$

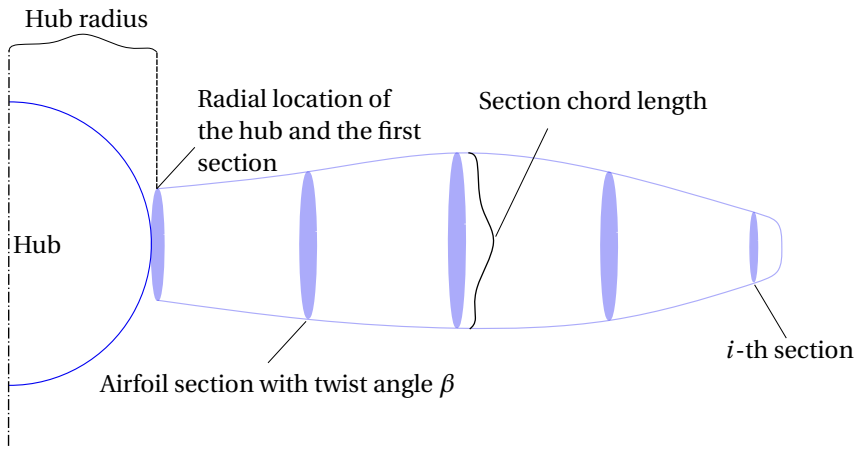

Figure 2.6: Blade parameterization showing some of the design variables.

The equality constraint maintained in every optimization case is the cruise thrust. The cruise thrust delivered by the propeller must be equal to the cruise thrust requirement of the aircraft at its design point. The constraint surface is depicted in Figure 2.5b. The constraint is set as:

$$h(\overline{x}) = \frac{\text{delivered } C_{T_{\text{cruise}}}(\overline{x})}{\text{required } C_{T_{\text{cruise}}}(\overline{x})} - 1 = 0 \tag{2.14}$$

The inequality constraints maintained for every optimization are the maximum tip Mach number in this thesis set at $M = 0.80$, the climb thrust requirement and the structural limitation. These constraints are set as:

$$\begin{aligned} g_1(\overline{x}) &= \frac{M_{\text{tip}}(\overline{x})}{M_{\text{tip, max}}(\overline{x})} - 1 \leq 0 \\ g_2(\overline{x}) &= 1 - \frac{\text{delivered } C_{T_{\text{climb}}}(\overline{x})}{\text{required } C_{T_{\text{climb}}}(\overline{x})} \leq 0 \\ g_3(\overline{x}) &= \frac{\sigma_{\text{root}}(\overline{x})}{\sigma_{\text{root, max}}(\overline{x})} - 1 \leq 0 \end{aligned} \tag{2.15}$$

Table 2.1: Design variables vector for the different optimizations performed in this thesis.

	Global optimization strategy	**Local optimization strategy**
Case 1: **Climb gradient**		
Simplified aero-model	$\overline{x} = \left[l_{\text{chord}}(1:i) \;\; \beta(1:i) \;\; D_p \;\; \text{rpm} \;\; B \;\; \beta_{\text{p}}\right]$	$\overline{x} = \left[l_{\text{chord}}(1:i) \;\; \beta(1:i) \;\; D_p \;\; \text{rpm} \;\; \beta_{\text{p}}\right]$
Detailed aero-model	-	$\overline{x} = \left[l_{\text{chord}}(1:i) \;\; \beta(1:i) \;\; D_p \;\; \text{rpm} \;\; \frac{t}{c}(1:i) \;\; C_{l_i}(1:i) \;\; \beta_{\text{p}}\right]$
Case 2: **TOFL & climb gradient**		
Simplified aero-model	-	$\overline{x} = \left[l_{\text{chord}}(1:i) \;\; \beta(1:i) \;\; D_p \;\; \text{rpm} \;\; P\right]$
Detailed aero-model	-	$\overline{x} = \left[l_{\text{chord}}(1:i) \;\; \beta(1:i) \;\; D_p \;\; \text{rpm} \;\; \frac{t}{c}(1:i) \;\; C_{l_i}(1:i) \;\; P\right]$

Additional constraints and variables used

If a global optimization is performed it is possible to include the amount of blades B in the design vector. The discrete value for the number of blades does not allow a gradient based search to be performed. A genetic algorithm is able to work with discrete values.

A genetic algorithm is computationally expensive and therefore a simplified aerodynamic model for the propeller airfoil sections is used. A simplified model for the aerodynamic properties excludes the aerodynamic properties as part of the propeller design vector. It is practical to evaluate airfoil geometry with a gradient descent optimization. The airfoil geometry parameterization consist of the airfoil camber C_{l_i} and thickness $\frac{t}{c}$ for each section. How the choice is made for these airfoil design variables is elaborated in Section 4.1.

The final design variable dependent on the optimization case is either the blade pitch angle in climb β_{p} or gas turbine power P. The reason behind this is given in Section 2.2. The total design vector with additional design variables dependent on the optimization being performed in between brackets:

$$\overline{x} = \left[l_{\text{chord}}(1:i) \;\; \beta(1:i) \;\; D_p \;\; \text{rpm} \;\; \left(B\right) \;\; \left(\tfrac{t}{c}(1:i) \;\; C_{l_i}(1:i)\right) \;\; \left(\beta_{\text{p}}\right) \;\; \left(P\right)\right] \tag{2.16}$$

For Case 2 the take-off field length is included in the inequality constraints of Equation (2.15). The inequality constraint equations then become:

$$\begin{aligned}
g_1(\overline{x}) &= \frac{M_{\text{tip}}(\overline{x})}{M_{\text{tip, max}}(\overline{x})} - 1 \leq 0 \\
g_2(\overline{x}) &= 1 - \frac{\text{delivered } C_{T_{\text{climb}}}(\overline{x})}{\text{required } C_{T_{\text{climb}}}(\overline{x})} \leq 0 \\
g_3(\overline{x}) &= \frac{\sigma_{\text{root}}(\overline{x})}{\sigma_{\text{root, max}}(\overline{x})} - 1 \leq 0 \\
g_4(\overline{x}) &= \frac{\text{obtained TOFL}(\overline{x})}{\text{required TOFL}(\overline{x})} - 1 \leq 0
\end{aligned} \tag{2.17}$$

The optimization scenarios are depicted in Table 2.1. For each scenario that is evaluated, the applicable variables are given.

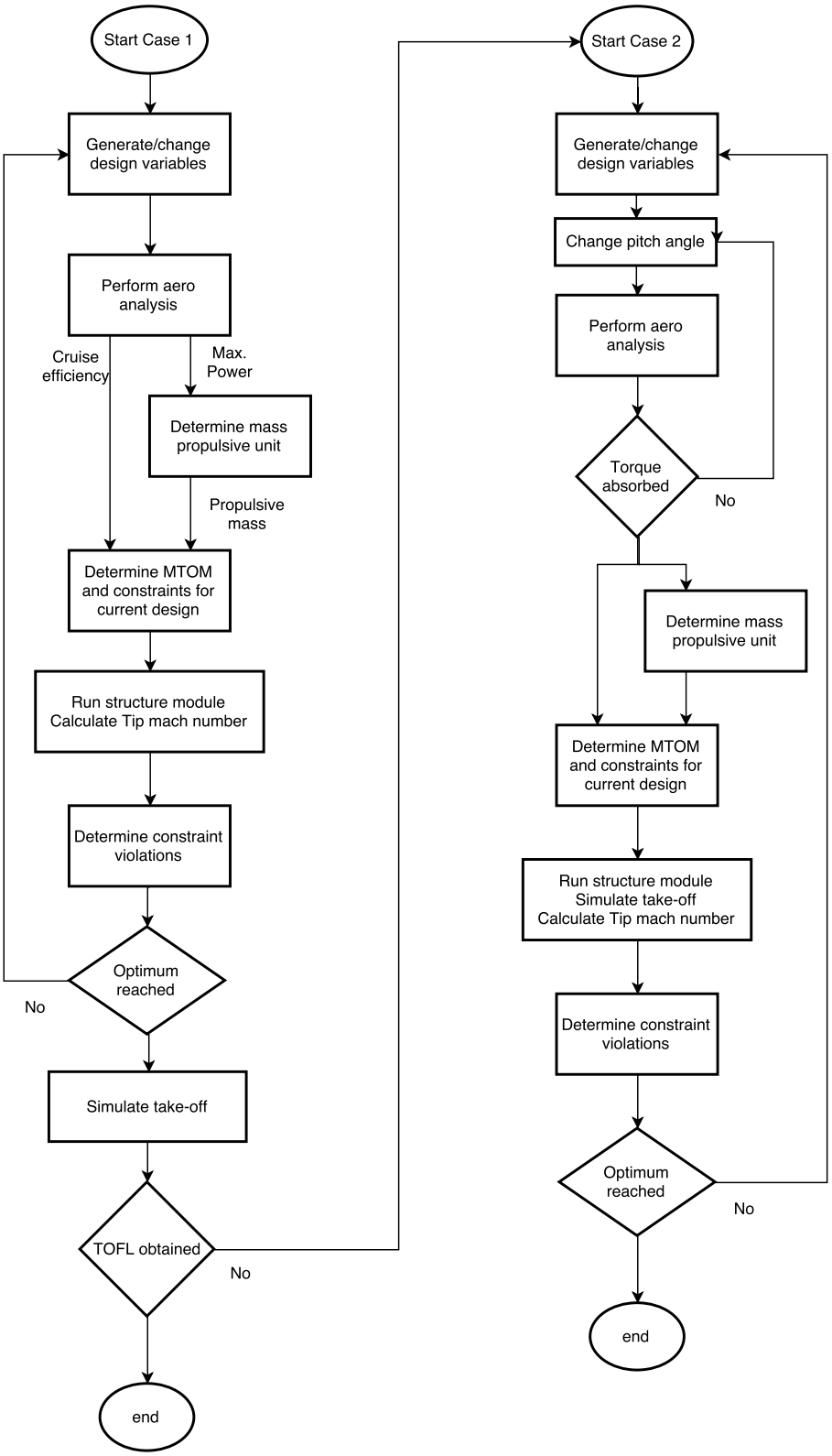

Figure 2.7: Optimization routine flowchart. Excluded is the interaction between the TOFL module and the aerodynamic solver.

I

Tools

3

Aerodynamic module

The propeller design method requires an aerodynamic tool to calculate the propeller performance. A number of solver methods are available. A study and selection of the best candidate will follow in this chapter. The propeller solver selection determines the design parameterization of the propeller.

3.1. Propeller theory selection

The aerodynamic solver selection results from a compromise between calculation time, propeller parameterization and accuracy of the result. In order to assess the solvers for these requirements a comparison is made. The solvers that are considered are given in Table 3.1. The candidates are ordered from low to high fidelity and evaluated on their ability to capture blade geometry/parameters, calculation accuracy during nominal cruise/climb condition as well as a high loading condition and computation time/expense. Time indications are estimations and should be considered to evaluate the relative difference between methods.

Table 3.1: Comparison between propeller aerodynamic solvers.

Method	Nominal cruise/climb accuracy	High loading accuracy	Parameter representation	Computational time
Actuator Disc Theory	+/-	-	-	instantaneous
Blade element momentum theory	+	+/-	+	In the order of seconds [11]
Free Wake Lifting Line	+	+	++	In the order of minutes [11]
Vortex Lattice Method	+	++	++	Increase over 'Free Wake Lifting Line'
RANS	++	++	++	In the order of hours [11]

The actuator disk method based on momentum theory is rejected as a propeller performance calculation method. The inadequate parameter representation does not allow a modeling of main propeller properties such as the blade geometry. The method lacks a viscous model to account for blade drag and neglects this loss. Instead an infinite number of blades is assumed.[12]

Based on Table 3.1 blade element momentum (BEM) theory is selected for the computation of propeller aerodynamic performance. The low computational time make it well suited for use in an optimization scheme where a large number of iterations are made [11]. Parameter description is good though not able to determine effects of propeller blade sweep and lean. A number of tip and hub loss models are available from vortex theory and in combination with a good viscous model for the section airfoil properties, will produce accurate results for the cruise and climb condition. The high loading case is dependant on the tip loss model which is generally not able to account for wake contraction and thus not very accurate for this case. BEM theory uses a 2D representation of the propeller blade sections. 3D aerodynamic effects of radial flow and stall delay are able to be corrected for but still produce an inaccuracy especially during low advance ratio calculations. [13]

Higher fidelity models are not considered due to their increase in computational time. Though these methods allow a more accurate determination of the tip losses and have the ability to determine the effect of

a wider range of parameters such as sweep. RANS methods are equipped to calculate the viscous affects of the propeller blade and do not need a separate method for determining airfoil section properties and thereby provide an even higher level of accuracy. [14]

3.1.1. Description of blade element momentum theory

The BEM theory is based on 2D aerodynamics of wing sections. A propeller blade is divided in the radial direction in a number of cross sections. Two neighboring sections describe an annulus in the propeller face. The flow velocity due to rotation of the blade and free stream velocity can be decomposed on each cross section. This is often described as blade element theory. The forces on the cross section, sketched in Figure 3.1, can be determined by an aerodynamic solver for wing sections. The calculated lift and drag are then able to be decomposed in to the thrust and torque of a propeller section. The average thrust and torque of two neighboring sections integrated over their radial distance determines the properties of their annulus. A summation over the blade radius for all the annulus' result in the propeller performance.

The flow speed can be decomposed from the flight speed and the speed due to rotation. However the propeller also induces a vorticity field that alters the flow speed of the section. Momentum theory is used to determine the induction factor for a given thrust and torque. The result of momentum theory is used to determine the trust and torque from the blade element. The resulting thrust and torque are reiterated into momentum theory. If a feasible propeller geometry is used this method rapidly converges to a solution.

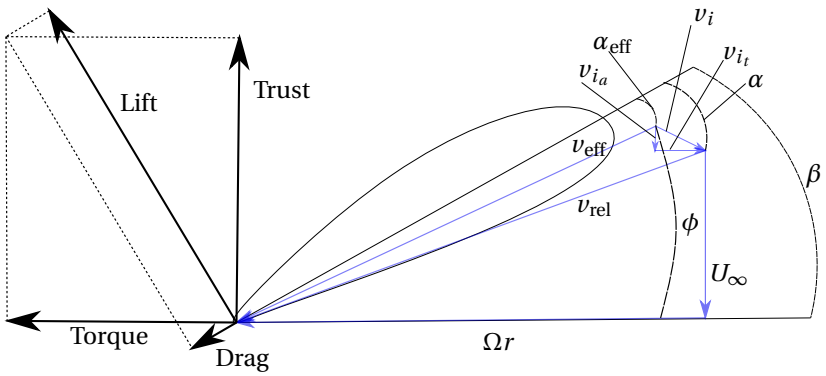

Figure 3.1: Sketch of a propeller blade 2D cross section.

3.1.2. BEM equations

The induced flow speed can be obtained by reiteration of the thrust and torque determined from the 2D section into momentum theory. Convergence of the solver can be tested by different variables with common choices: the angle of attack, angle ϕ or the induction factor. The method described below solves for axial and tangential induction factors v_{i_a} and v_{i_t}.

First the thrust and torque for the annulus δr multiplied with the number of blades is determined.

$$\frac{\delta T}{\delta r} = \frac{1}{2}\rho v_{\text{eff}}^2 cB(C_l \cos\phi - C_d \sin\phi) \tag{3.1}$$

$$\frac{\delta Q}{\delta r} = \frac{1}{2}\rho v_{\text{eff}}^2 crB(C_l \sin\phi + C_d \cos\phi) \tag{3.2}$$

with

$$v_{\text{eff}} = \frac{U_\infty(1+v_{i_a})}{\sin\phi} \tag{3.3}$$

Next conservation of linear momentum with the relation from actuator disk theory: $\delta T = \Delta p \delta A$ over area $2\pi r \delta r$ is applied:

$$\frac{\delta T}{\delta r} = 4\pi r \rho U_\infty^2 (1+v_{i_a}) v_{i_a} \tag{3.4}$$

and conservation of angular momentum:

$$\frac{\delta Q}{\delta r} = 4\pi r^3 \rho U_\infty (1 + v_{i_a}) v_{i_t} \tag{3.5}$$

When Equation (3.1) and Equation (3.2) are equalized with Equation (3.4) and Equation (3.5) it is possible to solve for the axial and tangential induction factors

$$v_{i_a} = \left[\frac{4\sin^2\phi}{\sigma_s(C_l\cos\phi - C_d\sin\phi)} - 1 \right]^{-1} \tag{3.6}$$

$$v_{i_t} = \left[\frac{4\sin\phi\cos\phi}{\sigma_s(C_l\sin\phi - C_d\cos\phi)} + 1 \right]^{-1} \tag{3.7}$$

with the local solidity

$$\sigma_s = \frac{Bc}{2\pi r} \tag{3.8}$$

3.1.3. Tip loss model

The BEM equations in the previous subsection lack a tip loss model. The loading on a propeller blade tends to zero towards the tip, just like a wing. This is due to the pressure equalization that must occur at the tip[15]. Betz [16] described the theory for an optimal circulation distribution for a propeller with a minimal induced loss. The wake of the propeller blades with a minimum induced loss moves axially backwards as rigid screw surfaces pumping fluid aft as an 'Archimedes screw'. Prandtl assumed that the vortices formed simple helical structures in the propellers wake. He then further simplified the wake model into disks that moved backwards with the speed $U(1-a)$, the central wake velocity. The average velocity of the whole wake is given as $U(1-af(r))$. The loss factor as determined by Prandtl is given as $f(r)$. This notation follows from Figure 3.2 which shows the wake of a wind turbine. The principle of the tip loss factor is the same as for a propeller, however the sign of the induced velocity a is opposite. The loss factor is the ratio in speed between the induced velocity for a given radial position and the average value of the wake. In this thesis the Prandtl tip loss correction is

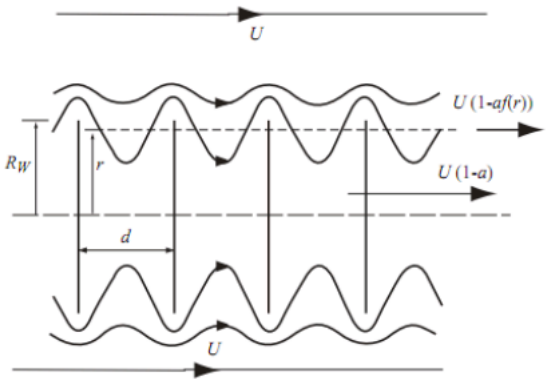

Figure 3.2: Prandtl's 2D representation of the wake vertices. [17]

used. For a derivation of the tip loss factor and a more in depth explanation the reader is referred to [18] or [19] the latter in particularly supplies an in depth and thorough review. In this thesis F is maintained for the Prandtl tip loss factor and v_i for the induced velocity.

Goldstein [20] produced a more accurate approach, describing and solving for the wake flow by use of Bessel functions. For more information see [14]. The theory of Goldstein was later extended by Theodorsen [21] to allow the light rotor assumption to be lifted and to include validity for highly loaded rotors. These methods rely on a correction factor which can be determined using Okulov's method which models the wake-screw as the superposition of multiple single helical vortex filaments[22]. Although relevant to this research the calculation of the Goldstein correction factor is outside the scope of this research.

3.2. BEM method solver selection

In Section 3.1 BEM theory is selected as the aerodynamic tool to be used in the optimization scheme. Many implementation methods of BEM theory exist. In this subsection a selection of four methods is studied for its applicability to this research.

3.2.1. Solver description

There are a number of options available for the implementation of the BEM method. For this research four methods are evaluated. Of high importance in the selection of the precise implementation of the method are the computational cost, which should be as low as possible.

Option 1 is a BEM code programmed by Veldhuis. This code follows the structure of Equations (3.1)–(3.8). This implementation of BEM theory is very common. It is the basic theory developed by Glauert in 1935 [23]. It uses the tip loss factor of Prandtl in its most general case. The method defines the helix angle between the 'screw surfaces' by the ratio of $v_a = U_\infty + v_{a_i}$ and $v_t = \Omega r - v_{t_i}$ this is the angle ϕ. The tip loss factor is then expressed as:

$$F = \frac{2}{\pi} \arccos \exp \left[-\pi \frac{R-r}{s} \right] \tag{3.9}$$

$$s = \frac{2\pi R}{B} \sin(\phi(r)) \tag{3.10}$$

The factor is used to correct the a reduction in lift occurring at the tip and thus corrects the calculation of induced felocity as follows:

$$v_{i_a} = \left[\frac{4\sin^2\phi}{\sigma_s(C_l\cos\phi - C_d\sin\phi)} - 1 \right]^{-1} \tag{3.11}$$

$$v_{i_t} = \left[\frac{4F\sin\phi\cos\phi}{\sigma_s(C_l\sin\phi - C_d\cos\phi)} + 1 \right]^{-1} \tag{3.12}$$

Option 2 is programmed from a method given in the paper of Adkins and Liebeck [24]. This code uses the BEM theory with some adjustments. It is often referred to as a method for propeller design with optimal circulation distribution. Adkins and Liebeck suggest making the following alteration to the calculation of the tip loss factor:

$$F = \frac{2}{\pi} \arccos(e^f) \tag{3.13}$$

$$f = \frac{\frac{B}{2}(1-\frac{r}{R})}{\sin\phi_{\text{tip}}} \tag{3.14}$$

$$\tan\phi = \frac{\tan\phi_{\text{tip}}}{\frac{r}{R}} \tag{3.15}$$

This solution is exact for the analysis of an optimally designed propeller at the design point. Furthermore, the placement of the correction factor is adjusted in accordance with the findings of Larrabee [25].The induction factors are calculated as:

$$v_{i_a} = \frac{\sigma_s K}{F - \sigma_s K} \tag{3.16}$$

$$v_{i_t} = \frac{\sigma_s K'}{F + \sigma_s K'} \tag{3.17}$$

with

$$K = \frac{C_l\cos\phi - C_d\sin\phi}{4\sin^2\phi} \tag{3.18}$$

$$K' = \frac{C_l\sin\phi - C_d\cos\phi}{4\cos\phi\sin\phi} \tag{3.19}$$

Implementation of an existing solver is considered for the remaining options. XROTOR is selected for this due to the wide acknowledgement of XROTOR as a good propeller analysis tool. Van Arnhem describes the research previously performed with this tool [26, p. 18], as well as a validation study of XROTOR. Furthermore XROTOR is fully compiled hence very fast. XROTOR includes multiple analysis methods.

Option 3 is the graded momentum formulation of XROTOR. Described by the user manual as: "Applies the classical theory of propellers revived recently by E.E. Larrabee and relies on the Betz-Prandtl tip loss fudge factor" [27].

Option 4 is the potential formulation, which according to the XROTOR user manual: "solves for the helically-symmetric potential flow about a rigid helicoidal wake and hence is valid for all blade numbers and advance ratios. It is an extension of Goldstein's 2 and 4 blade solution to all blade numbers and arbitrary radial load distributions" [27].

3.2.2. Solver selection

The four solvers are compared to an experiment with the N250 propeller[28]. The results show reasonable agreement for C_T and C_P between all methods, see Figure 3.3. The Adkins Liebeck method (option 2 in blue) has difficulty converging at low advance ratio. Low advance ratio calculations will be required for the analysis of the take-off run. This makes the A&L option less attractive.

As stated previously the computation time of the methods is important as the BEM code will be run for each function evaluation of the optimizer. A time comparison between the BEM methods is shown in Table 3.2. The evaluation of computation time is made difficult by an interpolation performed within the BEM code. This interpolation is necessary to determine the aerodynamic properties of the 2D blade sections. This is a time consuming process and its computation expense should be evaluated separately. Therefore, for the BEM codes programmed in Matlab, the aerodynamic polars determined by interpolation are replaced by a single C_l and single C_d equation for one airfoil, which provides an immediate solution. XROTOR is thought to always perform an interpolation over the blade for the sections supplied to XROTOR. Even if the number of section supplied is the same as the number of section requested for calculation. The XROTOR code is written in Fortran. Adjusting the source code is not considered for this research. This means it is not possible to circumvent the interpolation in favour of a simplified equivalent. XROTOR is a separate program which is executed outside of Matlab environment. It is expected that the interfacing between the two is detrimental to solver time. This is verified by executing a quit command to XROTOR from the Matlab environment, without performing any calculations. The time to complete this action rivals that of a full convergence of a BEM code developed in Matlab. In addition, debugging is hindered by implementing XROTOR, as it is not transparent. Meaning, it is difficult to track the calculation as it is happening to find errors.

Based on the computational expense, convergence stability and complete adjustability within Matlab the choice is made for the Veldhuis BEM code, option 1, for propeller aerodynamic analysis.

Table 3.2: Time comparison of BEM methods.

Time comparison of BEM methods	
Veldhuis BEM convergence	0.056 s
A&L BEM convergence	0.038 s
XROTOR open & close	0.037 s

The following assumptions are made in the implementation of BEM theory in this thesis:

- No aerodynamic interaction between the annular elements
- The velocity and the static pressure is uniform in each stream tube cross section
- The static pressure far upstream and downstream is equal to the ambient free stream
- Half the induced acceleration of the flow occurs in front of the propeller half of the acceleration occurs aft of the propeller
- Irrotational, incompressible, steady state fluid flow
- Hub losses are negligibly small.
- Tip losses are corrected for by the tip loss model of Prandtl
- Blades act independent from one another

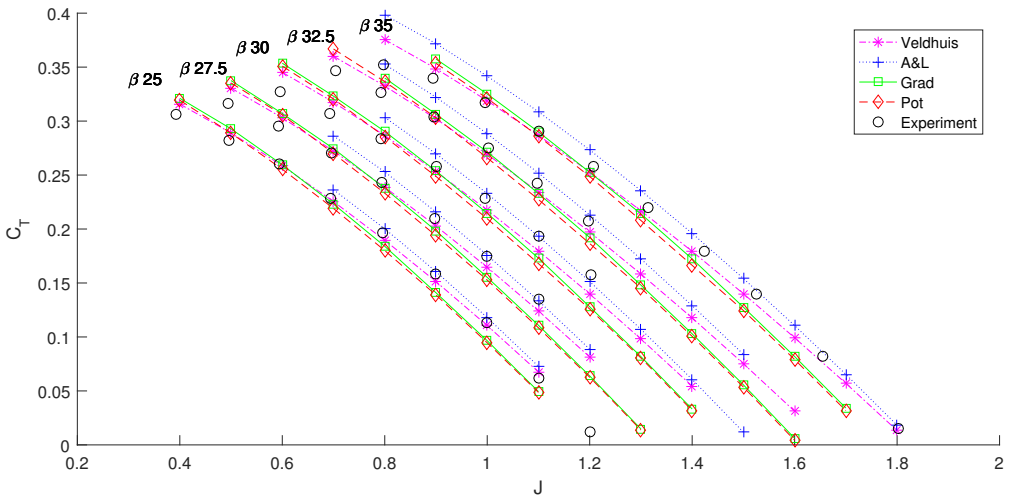

(a) Thrust coefficient comparison.

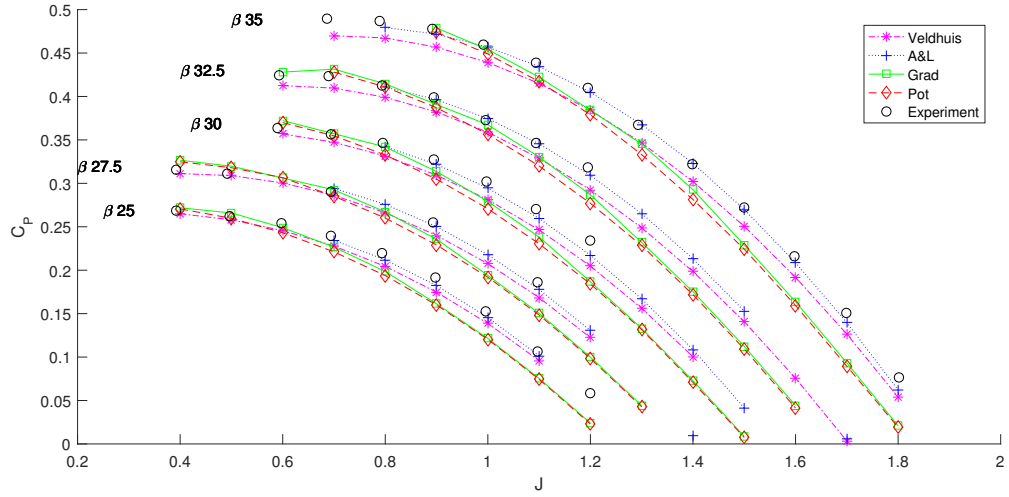

(b) Power coefficient comparison.

Figure 3.3: N250 propeller, rpm=10000, ISA-SL.

3.3. Implementation of BEM theory into the aero analysis module and final notes

The design variables generated by the optimizer are used to calculate the aerodynamic performance of the propeller. In this chapter BEM theory is selected for this calculation. The design variables used in BEM theory are given in Table 3.3. These inputs are used to calculate the propeller thrust, torque and propulsive efficiency. The thrust and torque of each section is supplied to the structure module, acting as an aerodynamic load on the propeller blade.

The optimization routine determines an optimal rpm for the propeller. The rotational rate of the propeller is not constant throughout the flight. Although the propeller designed in this thesis is a constant speed propeller, which means the propeller rotates at a set rpm independent of engine power setting, the set point for the propeller rpm varies with the flight condition. In the critical climb condition and during take-off the propeller spins at 100% design rpm. In cruise, the rpm set point is lowered by the pilot for better aerodynamic performance of the propeller. In this thesis the cruise rpm setting is 82% design rpm.

The propeller performance analysis is performed without considering installation effects. The efficiency of a propeller in tractor configuration is influenced by the interaction of the propeller slipstream with the wing of the aircraft. In addition, a propeller in climb operates at an angle of attack relative to the free stream.

Table 3.3: Variables used by BEM theory to calculate propeller performance.

Input of BEM theory	Source
Section chord lengths Section β-angles Propeller diameter Propeller rpm	Design variables
Section radial locations	Setting
Number of blades	Design variables/Setting
Airfoil polars	Airfoil Section Data
Atmosphere Rpm setting Free stream speed	Flight condition

This means that the angle of attack on the propeller sections changes during each revolution of the blade. These and other effects on installed performance of the propeller are neglected. The diameter of the hub or 'spinner' is maintained at 23% of the blade radius for the entirety of this research.

4

Airfoil Section Data

In this chapter airfoil data required by the BEM module is acquired. The airfoil properties are required numerous times during the iterative calculation preformed by the BEM module. This means that the properties must be available to the tool as quickly as possible. This places limits on the airfoil design freedom, which are discussed in the first section. The usage of 2D airfoil sections of propeller modeling inherently reduces the accuracy of the modeling tool. The flow over a propeller blade does not follow a straight path over the propeller blade. Rather the flow is curved by Coriolis and centrifugal forces. Representing the airfoils sections in 2D therefore presents an inaccuracy which is addressed. The take-off performance of the propeller is a design criteria. The performance of the propeller near zero advance ratio is therefore needed. From literature and propeller wind tunnel tests it is known that the root airfoils experience stall at low advance ratio's. Furthermore, stall can occur when there is an excess in power available and the propeller over pitches. Therefore the aerodynamic properties of an airfoil is required to be known past stall. Finally a method of determining airfoil section properties is determined and a procedure for implementing the airfoil section data into the BEM module is developed.

4.1. Airfoil geometry parameterization

The airfoil shape is an optimization variable. However the determination of a section airfoil shape during the optimization process must be limited in complexity. For a detailed propeller design airfoils are fine tuned to ensure adequate performance. At the conceptual level the designer is interested in the performance that can be expected of the propeller and the design of an airfoil is assumed to be not definitive. A few main airfoil properties will be used to develop a preliminary airfoil. The preliminary selection of the airfoils must show the major implications on the propeller performance.

Airfoil design by means of an optimization is traditionally done by adjusting curves that fit airfoil shapes. These are mathematical curves which can be modified by a limited number of control points. Example of these parameterization curves are: B-spline or CST coordinates. The advantage is, that given enough control points, virtually any shape airfoil can be produced. This method requires an aerodynamic solver to evaluate each change. Furthermore, the required number of control points is rather large and this has a detrimental effect on the optimization time. The airfoil for the preliminary design will be parametrized in as few variables as possible.

4.1.1. Propeller airfoil design sensitivities

In order to determine which airfoil parameters will be selected for optimization a brief summary of the airfoil operating range is given.

Propeller Root airfoil

For the type of propellers considered in this research, typical operating helical Mach numbers are in the range of M =0.5-0.6. This means low Reynolds numbers around 5×10^5 are possible. For typical airfoils this means that the boundary layer is laminar and can transition to turbulent over a separation bubble. For this research it is assumed that boundary layers are fully turbulent. The typical 'thin airfoil stall' associated with low Reynolds number flows is not considered.

The root has the biggest change in relative velocity. Due to the angular velocity being lowest at the root the forward speed of the aircraft plays a comparatively larger role. Therefore this part of the blade has a larger variance in the geometric angle of attack. When previous propeller designs are studied the root airfoils are typically thick. This allows for a large α range with attached flow. Based on ideal loading distributions the root typically has to produce low lift. A small root chord will be able to produce the required loading for a minimum in drag. However the root has to translate all the aerodynamic forces of the blade onto the airframe. This will mean that structural constraints will influence the airfoil choice as well.

Propeller tip airfoil

The tip of the propeller operates in the transonic range. Under shock stall the $c_{l_{\max}}$ is reduced and under the same effect drag divergence is encountered. Adding camber to the airfoil is beneficial to the $c_{l_{\max}}$ that is able to be obtained by the airfoil. This allows for a smaller chord which can be beneficial by reducing blade weight. In addition increasing the blade aspect ratio favourably influences the induced drag of the blade. The downside is that the effective α range in which this $c_{l_{\max}}$ is obtained is reduced. The pitching moment of the airfoil is not expected to have a large effect on the structural requirements of the blade as discussed in Chapter 6.

4.1.2. Design criteria airfoil family

Based on the operating criteria the following airfoil variables are important for the performance of the propeller:

- Thickness to chord ratio,
- Design lift coefficient/airfoil camber
- Transonic performance

The thickness to chord ratio has major effects on the conflicting requirements at the root. The thickness to chord ratio influences the drag divergence Mach number. Furthermore it dictates the lift curve slope, increasing α_{stall} as well as $c_{l_{\max}}$. Up to a given point the decreased leading edge curvature postpones leading edge stall. For further increased thickness the larger pressure gradient actually promotes trialing edge separation. Therefore the thickness to chord ratio will be made an airfoil design variable.

The airfoil camber increases the $c_{l_{\max}}$. It is also possible to realize a drag reduction as a cambered airfoil will produce less drag at its design lift coefficient compared to a symmetric airfoil at the same lift coefficient.

The transonic behavior will not be included in the design space. In order to include this, the amount of optimization variables will increase drastically. The pressure distribution will have to be tailored to ensure a weak shock. This means varying the nose radius, ensuring a flat pressure distribution over top the airfoil and adjusting the bottom of the airfoil to acquire the desired lift. Rather the Korn equation:

$$M_{dd} = \kappa - \frac{c_{l_{M=0}}}{10} - \frac{t}{c} \tag{4.1}$$

will be used with an assumed technology factor κ to determine the drag divergence Mach number M_{dd}. It is assumed that the preliminary airfoil can be adjusted to have proper transonic characteristics to the degree of the technology factor without impacting the established lift and drag curves by a significant amount. Compressibility correction can be done by implementing the Prandtl-Glauert correction:

$$\mu_{PG} = \frac{1}{\sqrt{1-M^2}} \tag{4.2}$$

Kaplan expanded on this to include the airfoil thickness:

$$\mu_K = \mu_{PG} + \frac{\frac{t}{c}}{1+\frac{t}{c}}\left[\mu_{PG}(\mu_{PG}-1) + \frac{1}{4}(\gamma+1)(\mu_{PG}^2-1)^2\right] \tag{4.3}$$

The equation of Kaplan will be used to correct the lift coefficient by the following equation:

$$c_l = c_{l_{M=0}}\mu_K \frac{1-M^2}{1-M_{dd}^2} \tag{4.4}$$

The correction of the coefficient of drag for shock induced separation is:

$$c_d = c_{d_{M=0}} + \left[\frac{M - M_{dd}}{1 - M_{dd}}\right]^3 \quad \text{for} \quad M_{dd} < M < 1 \tag{4.5}$$

A validation study of the Korn equation is available in [29]. The technology factor κ has been established to be 0.95 for modern supercritical airfoils.[30] The NACA 16-series, one of the first airfoils designed for improved transonic behavior has been found to have a technology factor of $\kappa = 0.87$ [31]. For this research a technology factor of $\kappa = 0.87$ is maintained. **Note:** these are 2D corrections.

4.1.3. Section conclusion

In Section 4.1.2 the geometric parameters of airfoil thickness to chord ratio and the maximum camber were selected as airfoil optimization variables. To asses the changes that varying these geometric parameters entail for the aerodynamic variables, an airfoil family is selected where the thickness to chord and maximum camber can be varied. For this the NACA 4-series and the 16-series are considered. The 16-series was developed when Mach effects were first encountered for high speed propellers. The 16-series has a pressure distribution that has a uniform distribution of induced velocity [32]. It has a flat pressure distribution and can be thought of as one of the first airfoils designed to minimize the 'compressibility burble' or the shock that terminates supercritical flow over the airfoil. To represent all airfoils distributed along the blade by a supercritical airfoil family is not required. As discussed in Section 4.1.2 it is assumed that the pressure distribution of the selected airfoil can be tailored later -to an assumed technology level- to cope with transonic effects. The NACA 4-series is selected as an airfoil family as the researcher is familiar with this family, the airfoil coordinates can be easily determined from a series of equations as well as wealth of wind tunnel tests including 2D tests past $c_{l_{\max}}$ available.

4.2. Discussion on the behavior of rotor airfoil sections

In the previous section the relevant airfoil design parameters were described. In this section the behavior of lift and drag curves of rotor airfoils is treated. The stall delay rotor airfoil sections experience is studied together with the post stall behavior of the lift and drag. After which, methods for representing airfoil aerodynamic data mathematically is described. Finally, the implications of stall delay and the available representation methods will be used to compare two aerodynamic airfoil analysis solvers: XFOIL and RFOIL.

4.2.1. Stall delay of rotor airfoils and post stall development of lift and drag

BEM theory uses airfoil sections to determine propeller performance. These sections are modeled as 2D sections but they represent a slice of the propeller blade. The blade produces 3D effects which impact performance. It has been shown by numerous researchers that propeller airfoil sections have an increase in maximum lift due to delayed turbulent separation. This requires a correction over the 2D prediction of lift and drag.

The lift and drag of an airfoil past its stall angle of attack have to be available to the BEM method. In certain scenarios the propeller will operate with part of its blade stalled. Research into wind turbine airfoils is used to gain an understanding of this operating regime. The aerodynamic performance of wind turbine blade sections past stall is still uncertain but advancements have been made to predict the effects of rotation on the airfoil aerodynamic properties. Research regarding the applicability to propellers is absent. However, researchers in the past have used these wind turbine corrections in propeller related research. The behavior of the rotor airfoils can be assumed to be similar. Stall research of wind turbine sections will be used in this thesis to correct 2D sections for stall delay and establish the post stall behavior of rotor airfoils subject to radial flow in the boundary layer.

Incremental increase in $c_{l_{\max}}$

According to Lindenburg[33, p. 5]: "Snel et al. derived a 3D correction method that gives an increase of the aerodynamic lift coefficient for the effects of rotation." This method is easily implemented in lower order models. Snel et al. developed the following equation based on a quadratic relationship between the cord length and the span wise position:

$$c_l = c_{l_{2D}} + A\left(\frac{c}{r}\right)^B (c_{l_{2D,\,\text{linear}}} - c_{l_{2D}}) \tag{4.6}$$

Chaviaropoulos and Hansen expanded on this work by analyzing the effect of the local twist angle. This analysis was performed by means of a Navier-Stokes CFD analysis [34]. Timmer [34] compares the above two stall models to two more resent models by Lindenburg and Bak et al. Timmer concludes that Snel et al. produces the best fit for determining $c_{l_{max}}$ compared to wind turbine experiments. Figure 4.1 shows the lift curve of an airfoil for a number of radial positions on a propeller blade as determined by Himmelskamp.

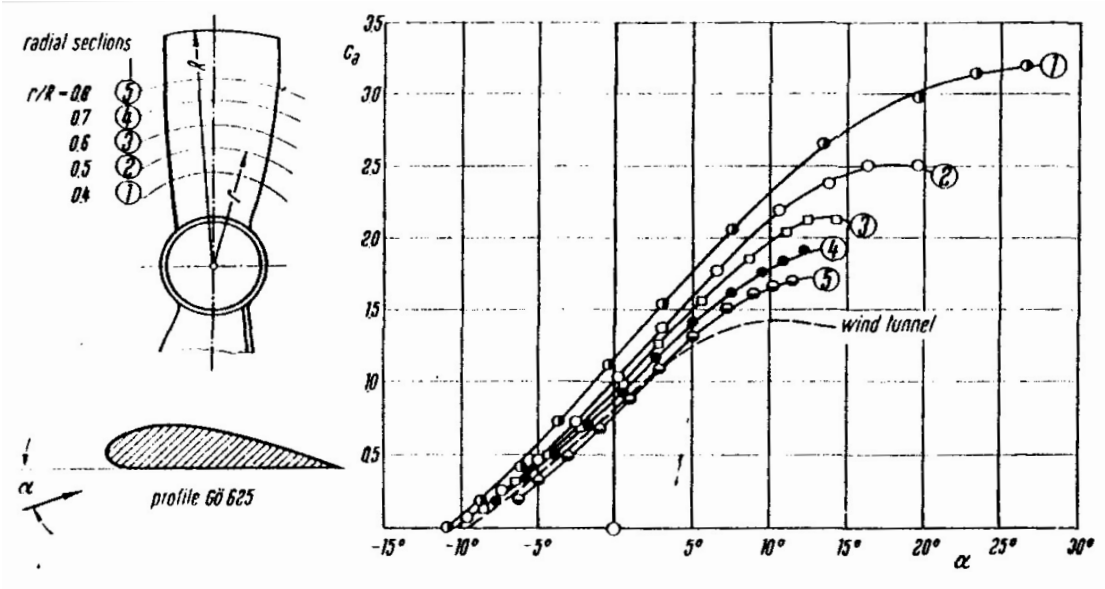

Figure 4.1: Lift coefficient c_a as a function of alpha and radial position on the propeller blade. [35]

Development of c_l as a function of α past $c_{l_{max}}$

Next to increased $c_{l_{max}}$ of rotor airfoils, depending on the radial location of the section, the development of lift and drag past $c_{l_{max}}$ can be very different compared to 2D airfoils. In experiments performed by the NREL and TU Delft [36] pressure tabs were fitted to rotor blades and the aerodynamic properties investigated. Although no conclusion is drawn in this research owing to the small data set available and high inherent uncertainty in the measurement. In general the researcher cites under prediction of Snel's model past $c_{l_{max}}$. The research does conclude that c_l is under predicted by 15 % when 2D experimental data is corrected. The researcher suggest the use of the RFOIL code as it features the best agreement over the radius of the rotor blade. Particularly citing the inclusion of the drop in lift coefficient past $c_{l_{max}}$ allowed by Snell's method as not existent for actual rotor airfoils. The data collected by this research is reviewed and the data is time averaged and produces a clearer trend which shows that $c_{l_{max}}$ for the 2D airfoil section can be increased by as little as 5% up to 20%[37].

However Breton et al. [38] compares a host of rotor stall methods. The result of this analysis can be found in Figure 4.2. The researcher concludes that there is poor agreement between all models and experimental data in the range past $c_{l_{max}}$. The agreement between the models for predicting the incremental increase in $c_{l_{max}}$ over the 2D data is fair. The disagreement past $c_{l_{max}}$ is undesirable. For the aerodynamic data required, an accurate estimation of the polars is needed. With the large spread between the different models selecting one would be arbitrary and not representative. An assumption will be made for the behavior past stall in following sections.

4.2.2. Representing airfoil data numerically

In this section options for representing the lift and drag of the airfoil sections mathematically are assessed. Determining the aerodynamic properties of a given rotor airfoil on demand by means of a solver such as XFOIL or RFOIL is unattractive due to the computational cost. A database of aerodynamic properties is therefore desired. The following options are identified to describe airfoil aerodynamics in a database:

1. c_l , c_d curves build from equations, calibrated by empirical data
2. Curves fitted to an aerodynamic database established by either experiments or an aerodynamic solver.

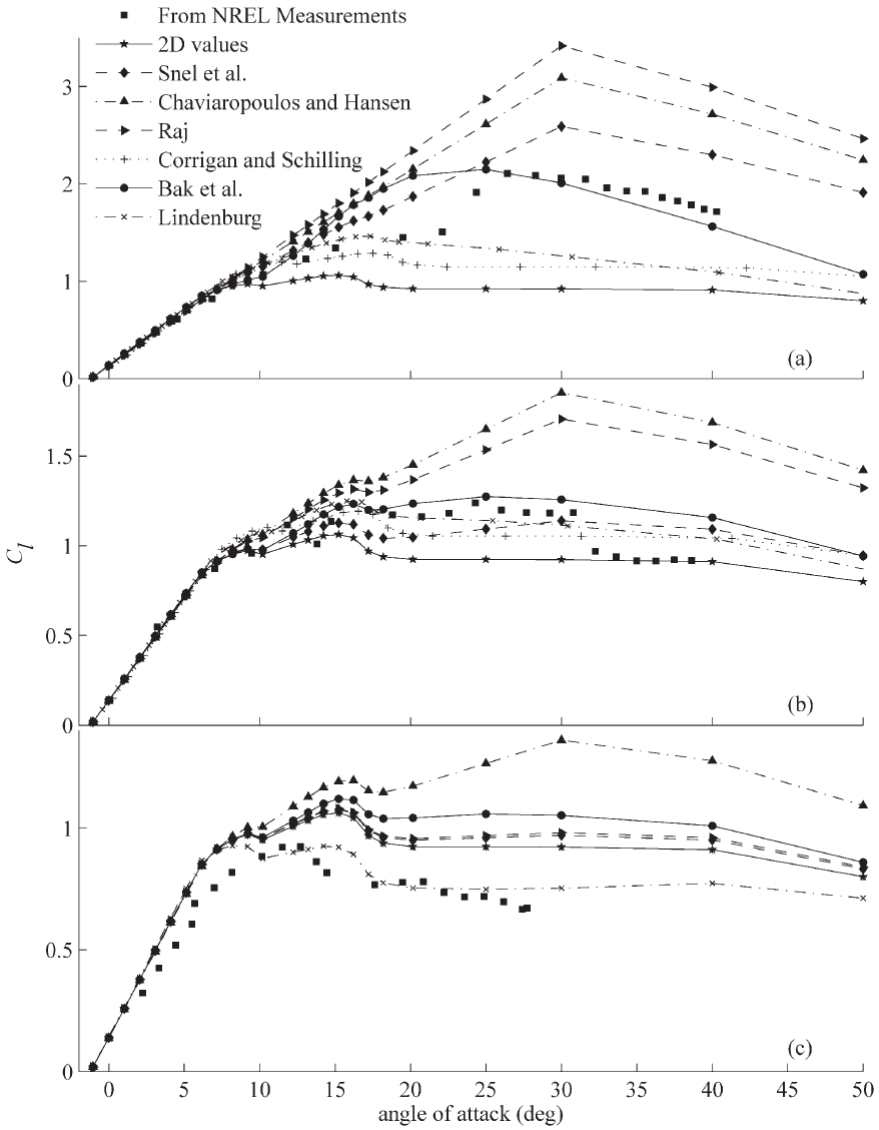

Figure 4.2: Lift coefficient as a function of angle of attack for different stall delay models. Radial position: (a) 30% span, (b) 63% span and (c) 95% span [38]. The airfoil used for this comparison is unknown.

In recent years, both options have been used by different researchers for propeller analysis. The existing methods are evaluated and in following sections a custom method, incorporating some of the ideas of these researchers, is developed.

Using equations to represent airfoil data

Typically the lift and drag curves can be captured by the simplified equations:

$$c_l = c_{l_\alpha}(\alpha - \alpha_{zl}) \tag{4.7}$$

$$c_d = c_{d_0} - C_1 c_l + C_2 c_l^2 \tag{4.8}$$

This set of equations can capture the general properties of an airfoil. Care has to be taken to ensure that the chosen combination of calibration constants is valid so that the equations will represent a possible airfoil. In order to guarantee this the calibration must be done with empirical or calculated airfoil data. These equations are frequently used to estimate lower order airfoil performance.

The researcher Traub [39] used these equations to derive a set of formulations that would be suitable for the determination of propeller airfoil properties for use in a BEM solver. Missing from the representation by

Equations (4.7)–(4.8) is the behavior at and past stall. Traub fitted a stall model for propeller blades to these equations:

$$c_l = c_{l_\alpha}\alpha\left[\frac{1+X^m}{2}\right]^2 \tag{4.9}$$

$$X = \frac{1}{1+e^{\sigma_t[\alpha-\alpha_{\text{stall}}]}} \tag{4.10}$$

$$c_d = X\left[c_{d\min} + k_p(c_l - c_{l\text{md}})^2\right] + (1-X)\left[c_l\tan(\alpha) + 0.5c_{d\min}\cos(\alpha_{\text{geom}})\right] \tag{4.11}$$

$$k_p = \frac{c_{d\min}}{c_{l(l/d)_{\max}} - c_{l\text{md}}^2} \tag{4.12}$$

The variable X indicates separation, at $X = 1$ the flow is fully attached and at $X = 0$ the flow has fully separated. The scaling parameters m and σ_t can be used to set the rate of lift loss past stall. Traub suggest setting $\sigma_t = 0.1$ and $m = 0.4$ after calibrating with windmill test data from Rosten [40]. The drag from the airfoil is divided in the attached part X and the separated part $(1-X)$. The attached region describes conventional drag contributions. For the separated region it is assumed that once flow has separated the drag is equal to the stream wise component of the normal force.

The model lacks a correction for the radial position of the airfoil section. In Section 4.2.1 it was found that this has a large effect on the postponement of turbulent separation and subsequent behavior past separation. The $c_{l_{\max}}$ increment gain due to radial flow is accounted for by the calibrations parameters. This is unnecessary. In Section 4.2.1 it is concluded that windmill corrections are in agreement for this region. This model is a mathematical method for describing the 3D effects post 2D $c_{l_{\max}}$. The development of lift and drag is calibrated by rotor experiments and not based on boundary layer theory. The validation of a propeller analyzed with a BEM code incorporating Traub's aerodynamic data[39] produces results that are fair.

Using fitted curves to represent airfoil data

As discussed in the beginning of the section, a viable method for determining the aerodynamic data would be to fit curves to calibration points. The well known BEM solver XROTOR uses this method. it requires the following data points:

- α_{zl}
- $\frac{\delta c_l}{\delta \alpha}$
- $c_{l_{\max}}$
- c_l increment to stall,
- $c_{d_{\min}}$
- c_l at $c_{d_{\min}}$
- $\frac{\delta c_d}{\delta c_l}^2$

From of these calibration points XROTOR builds c_l and c_d curves. Dorfling et al. [31] describes a model which uses airfoil data for the calibration of a curve fitting model for propeller airfoil sections. The calibration is based on wind tunnel data of 2D sections measured over 90 degrees angle of attack to set up the initial curve constraints: a linear curve up to the linear departure angle of the airfoil, zero slope at the maximum lift coefficient and post stall minimum. For the drag the following equation is used:

$$c_d = 0.1\left[c_{l\text{md}} - (c_{l_\alpha}\alpha + c_{l0})\right]^4 + c_{d\min} \tag{4.13}$$

Calibration is performed by assessing the effects of the integrated lift coefficient and thickness to cord ratio on the location of the calibration points. The validation of the aerodynamic model performed by Dorfling is not clear near the stall area and conclusions are not convincing. Furthermore as discussed in Section 4.2.1, rotor airfoils past stall are thought not to exhibit the same behaviour of 2D airfoils. This is not addressed in the model. The drag is estimated by the fourth order parabola given in Equation (4.13) for low angles of attack. For high angles of attack a parabola which reaches its maximum drag coefficient of 2 at 90 degrees angle of attack is used. The two curves are made to transition at the point where the slope of the two curves is equal.

4.2.3. Comparison of airfoil solvers

The methods for representing airfoil lift and drag curves have been evaluated. In this subsection two solvers for gathering the configuration parameters of the two discussed methods are compared. This comparison is made in order to decide how airfoil data should be determined in the BEM code. Two solvers are evaluated in this subsection: XFOIL and RFOIL. XFOIL is a proven solver which is very familiar to the author. There exist a semi-public alteration of this tool RFOIL, build for the analysis of rotor airfoils. Both methods are poor at predicting $c_{l_{\max}}$ for thick airfoils. The reason for this will be elaborated on, conjointly an alternative method for determining $c_{l_{\max}}$ is made.

XFOIL

XFOIL is a fast panel method with included viscous calculations. The inviscid formulation is a second order panel method. The flow field is created by superimposing a vortex and source on each panel. The viscous effects in the boundary layer are captured by a integral boundary layer formulation. By use of a surface transpiration model calculation of partially separated flow is permitted as this model features a close integration with the inviscid model. XFOIL fails to accurately model large regions of separated flow. For the determination of the 2D $c_{l\max}$ XFOIL can not be used. Especially the analysis of thick airfoils results in large errors. [41]

RFOIL

RFOIL is a tool for wind turbine rotor airfoils developed by TUDelft, ECN (dutch energy research centre) and NLR (Netherlands aerospace centre). It is a modification of XFOIL. The improvements of RFOIL for rotor airfoils over XFOIL can be summarized as:

1. Improved convergence stability at high angle of attack
2. Adjustment of the closure relations made in the turbulent boundary layer calculations
3. Corrections made to the maximum lift produced

Modification were made to increase the stability of the code allowing some improvement in converging on a prediction past stall. However, similar to XFOIL thick airfoil $c_{l_{\max}}$ is over predicted [42]. The increased stability is due to improved boundary layer closure relations. The laminar boundary layer calculations are not adjusted because it is thought that radial flow has little effect [43]. The transition calculation is also unaltered. The same transition calculation as XFOIL based on the e^n method is used. It was argued to be too complicated to incorporate the influence of radial flow on transition into RFOIL. The turbulent boundary layer equations are adjusted to better predict drag, turbulent separation and subsequently the reliability of the 3D corrected $c_{l_{\max}}$. Corrections made to the lift prediction are from the model of Snel. The following conclusion regarding RFOIL is drawn by Rooij [42, p. 24]: 'In general the prediction of the airfoil characteristics with RFOIL will show a reduced drag coefficient of app. 10% and its prediction of the lift curve near stall will be reasonably well. The post stall curve is in general too optimistic because rapid movement of turbulent separation can not be predicted correctly.' RFOIL is useful to model rotor airfoils. However similar to XFOIL, it fails to accurately predict $c_{l_{\max}}$ as well as the behavior past stall.

Prediction of $c_{l_{\max}}$

As discussed in Section 4.2.3 panel methods are unreliable for the determining $c_{l_{\max}}$. Not only is the determined value over predicted, often no value can be found as the solver will not converge. A method produced by ESDU [44] produces fast, accurate results for 2D airfoils sections valid up to $M = 0.4$. To account for mach effects the method discussed in Section 4.1.2 is used. From Table 4.1, it is concluded that particularly for airfoil thickness $\frac{t}{c} \geq 0.20$ the ESDU method produces better results. The ESDU method will be used for the prediction of $c_{l_{\max}}$.

4.3. Development of the aerodynamic airfoil database for use in the BEM code

The airfoil design freedom is determined as the thickness to chord ratio and the camber of the airfoil. In order to vary these geometric parameters the NACA-4series is selected as the airfoil family to be modified. The lift and drag curves will be corrected for Mach effects using a technology factor of $\kappa = 0.87$. The aerodynamic model to be used in this research will be described based on the findings in the previous sections. Summarizing these points:

Table 4.1: Comparison of $c_{l_{max}}$ evaluated at $Re = 3 \times 10^6$.

NACA number	Wind-tunnel [Ref]	XFOIL	Δ	ESDU	Δ
0006	0.83 [45]	0.97	17 %	1.01	22 %
0009	1.3 [45]	1.53	18 %	1.4	8 %
0012	1.5 [45]	1.59	6 %	1.64	9 %
0021	1.22 [46]	1.53	25 %	1.35	11 %
0025	1.33 [46]	1.53	15 %	1.21	9 %
1408	1.35 [45]	1.51	12 %	1.46	8 %
1410	1.5 [45]	1.65	10 %	1.67	11%
1412	1.6 [45]	1.65	3 %	1.73	8 %
2408	1.4 [45]	1.61	15 %	1.59	14 %
2410	1.65 [45]	1.71	4 %	1.72	4 %
2412	1.6 [45]	1.69	6 %	1.79	12 %
2415	1.4 [45]	1.68	20 %	1.67	19 %
2418	1.35 [45]	1.68	24 %	1.53	13 %
2421	1.25 [45]	1.67	34 %	1.41	13 %
2424	1.18 [45]	1.64	39 %	1.3	10 %
4412	1.5 [45]	1.78	19 %	1.87	25 %
4415	1.42 [45]	1.76	24 %	1.8	27 %
4418	1.42 [45]	1.77	25 %	1.67	18 %
4421	1.32 [45]	1.79	36 %	1.52	15 %
4424	1.28 [45]	1.8	41 %	-	-

- The incremental increase in $c_{l_{max}}$ can be corrected by a number of models.
- The prediction of 2D $c_{l_{max}}$ for thick airfoils is best done by method proposed by ESDU. For thin airfoils XFOIL/RFOIL produces acceptable results.
- The post $c_{l_{max}}$ development of lift and drag are not able to be accurately predicted; an assumption must be made.
- The lift and drag curve's can be estimated by either XFOIL or RFOIL.

Based on these points a curve fitting model is identified as the best method for producing lift and drag curves. Choosing this model allows for the calibration points to be by established by separate methods.

Assumption for lift and drag development past α_{stall} and correction for increased $c_{l_{max}}$

The 2D $c_{l_{max}}$ is corrected with Snel et al. correction for radial flow. For the development of lift past α_{stall} the following assumption is made:

If a particular airfoil operates at an angle of attack larger then α_{stall} the lift produced will be equal to the lift produced at the corrected $c_{l_{max}}$ for that airfoil.

The drag past α_{stall} is assumed to follow the same gradient as at α_{stall} up to the inflection point. It is known that the drag increases up to 90 degrees angle of attack and levels off into a parabola. The maximum value of the drag coefficient at 90 degrees angle of attack is set at 1.3 [47]. A parabola centred at 90 degrees and $c_d = 1.3$ is matched to the original drag curves at the point where the slope of the two curves match (the inflection point).

The flaws in this model include a neglection in the drop in lift past $c_{l_{max}}$ for thin airfoils. Thin 2D airfoil sections produce this stalling behavior when evaluated at the same Reynolds number as the propeller tips. Because a propeller features thin airfoil sections near the tip, where radial effects are minimal, it is fair to assume that this drop in lift coefficient is present. Furthermore, any rise in c_l past 2D $c_{l_{max}}$ at the root is not accounted for. This shortcoming will be addressed in any conclusions drawn from the finalized propeller design. The drag is not adjusted for radial flow and follows 2D theory. This means drag rise at the root sections is predicted to early as the flow remains attached up to a higher angle of attack then predicted.

Calibration points

For the lift curve the same calibration data as used by XROTOR is used with the addition of the post $c_{l_{\max}}$ model. The choice is made to use XFOIL for the determination of the calibration data. Because the maximum lift coefficient is determined by the ESDU method, the advantage of using RFOIL would remain the adjusted boundary layer equations. However because assessing and understanding these equations is beyond the scope of this thesis, using these would be unwise as their exact effect is unknown. Because the boundary layer behaviour is not clear the assumption for this thesis is to use fully turbulent flow over the airfoil sections which would be the worst case scenario in terms of drag. The choice for XFOIL is made based on this being a open source readily available solver and clear documentation available. Using RFOIL to build an aero-database would also mean that on top of the airfoil thickness, camber and Reynolds number the radial location would have be a variable. This is because RFOIL includes the 3D correction in its analysis. The 2D value for $c_{l_{\max}}$ found by ESDU method is corrected by Snel's model. Based on the conclusion that most correction models available are accurate for the incremental increase in $c_{l_{\max}}$.

Building the aero-database

The database of aerodynamic polars for the airfoil section is established for a range of Reynolds numbers, thickness to chord ratio's and camber given in Table 4.2. XFOIL is used to determine the polars of the airfoil for these parameters. This brings some complications as XFOIL can have trouble converging particularly at high angle of attack. To mitigate this some measures are taken. First an analysis is not performed for a sequence of angle of attack but rather separately for each angle of attack. This allows the airfoil to be analyzed in non-viscous mode before performing a viscous analysis which aids convergence stability. If the analysis fails to converge an extra attempt is made with a slightly altered Reynolds number. If convergence is still not achieved the point is rejected and a the next angle of attack is tried. Generally not more then two-three convergence failures occur in a row which does not impact the fit accuracy greatly. The assumption of a fully turbulent boundary layer is realized by setting the n-factor to $n = 1$. Alternatively, forcing transition to occur on the leading edge was found to destabilize the convergence. A compound C_d curve is made with the low angle of attack portion fitted to polars determined with XFOIL. The high angle of attack drag model follows the example of [48] with an altercation to the $C_{d_{\max}}$ as found in [47]. A parabola centered at 90 degrees angle of attack is fitted as follows:

The curve fitted to the drag polars found by XFOIL is defined as

$$C_d = f_{\text{XFOIL}}(\alpha) \tag{4.14}$$

The parabola for the high angle of attack drag is described by the following equation:

$$C_d = C_1\left(\alpha - \frac{\pi}{2}\right)^2 + C_{d_{\max}} = C_1 f_{\text{parabola}}(\alpha) + C_{d_{\max}} \tag{4.15}$$

With $C_{d_{\max}} = 1.3$ Two unknowns need to be found: the parabola constant C_1 and the angle of attack where the two models transition α_{trans}. These can be found by solving the following set of equations

$$f_{\text{XFOIL}}(\alpha) = C_1 f_{\text{parabola}}(\alpha) + C_{d_{\max}} \tag{4.16}$$

$$f'_{\text{XFOIL}}(\alpha) = \left(C_1 f_{\text{parabola}}(\alpha) + C_{d_{\max}}\right)' \tag{4.17}$$

This procedure is depicted schematically in Flowchart 4.3.

Table 4.2: Parameter range of airfoil database used in BEM theory.

Parameter range	
Camber	0-5%
Thickness to chord ratio	6-26 %
Reynolds Numbers ($\times 10^6$)	[0.5 0.7 1.0 1.5 2.0 3.0 5.0]

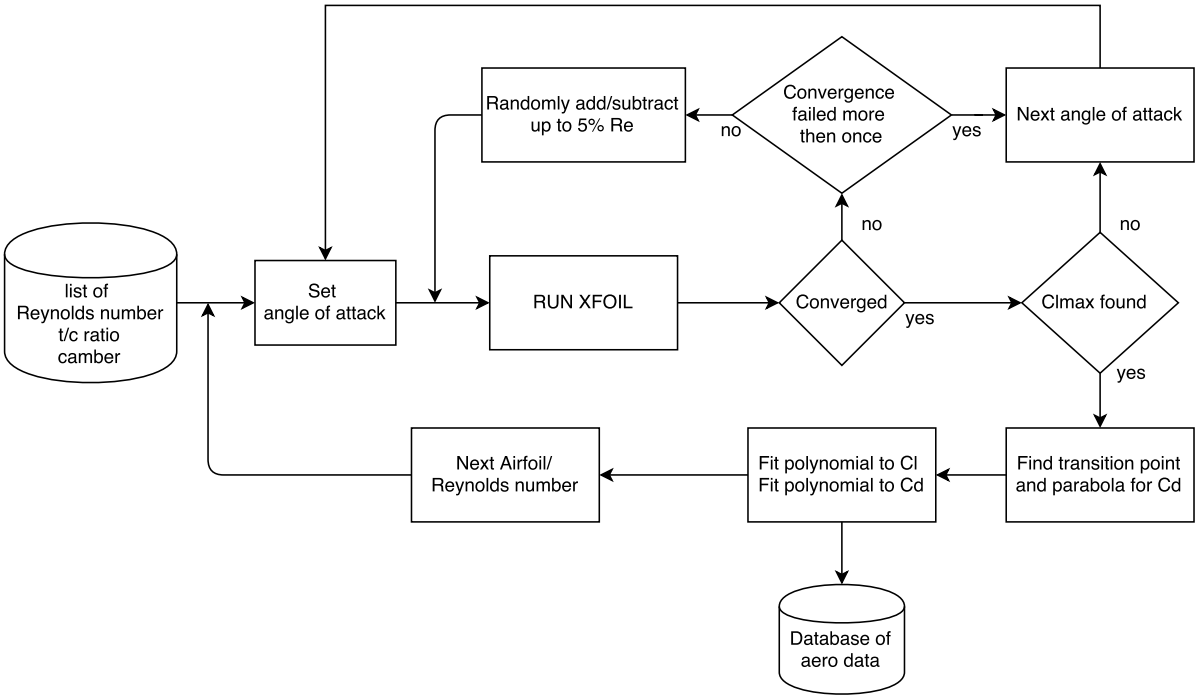

Figure 4.3: Flowchart of the establishment of the aerodynamic database.

4.4. Implementation of the aerodynamic database into the BEM code

The sampling method described in previous sections provides a collection of C_l and C_d alpha curves as a function of camber, thickness and Reynolds number. The lift and drag of an airfoil evaluated at a given angle of attack must be made available to the BEM solver from these curves. Again this operation should be as fast as possible. A regression model from all curves was made for this purpose. The resulting hyper surface produced a R^2 value of 0.891. A better approach was found after some experimentation with interpolation methods. The resulting interpolation method determines the required C_l and C_d as follows: First the 3 closest values of camber thickness and Reynolds number that were sampled and fall above the current value for camber, thickness and Reynolds number is found. This is repeated the same way and the closest sample values that fall below the current point is determined. For each combination of these curves the aerodynamic polars are calculated resulting in 8 values. A 3D cubic interpolation then calculates the aerodynamic polars for the current point.

5

Take-off simulation module

In this chapter, the take-off simulation module is developed. It is critical that the propeller can produce the required thrust to obtain a desired take-off field length. The aircraft must safely be able to accelerate to V_2 within this length when the critical engine fails at the decision speed during the take-off. The decision speed occurs at the moment the field length required for rejecting or committing to the take-off is equal. This is called the balanced field length. In this chapter the aim is to establish a method for calculating if a propeller and power plant design will satisfy the aircraft's take-off field length requirement.

To calculate the thrust requirement for a given take-off field length several empirical formulations exist. These are calibrated by a group of parameters first established by Loftin[49]. Four methods for propeller aircraft based on the original derivation of Loftin are evaluated in Appendix C. The conclusion of this evaluation is that these methods are not suitable for propeller design. The methods rely on an empirical calibration. Because of this, the methods are deemed of too low fidelity for propeller design in this thesis.

Besides an empirical estimation it is also possible to simulate a take-off run by applying Newtons second law: 'The acceleration of an object is directly proportional to the magnitude of the net force, in the same direction as the net force, and inversely proportional to the mass of the object.' This means that with the aerodynamic polars of the aircraft known, the thrust calculated and some assumptions for unknowns (such as the rolling friction or the pitch rate initiated by the pilot), the take-off field length can be calculated. This method is used to determine the take-off performance of the propeller and the take-off field length of the aircraft. The method for calculating the take-off field length follows the example of [50, p. 299-327] or [51, p. 301-311].

5.1. Aircraft data

The take-off module is developed with the help of two reference turboprop aircraft. The Fokker 50 and ATR72-600 are selected for this purpose. The aircraft data is given in Table 5.1. The data is used to calculate the take-off field length of each aircraft. The result will be used to verify the take-off module and calibrate it for use in the optimization tool.

Table 5.1: Main aircraft reference data for take-off analysis.

	ATR72-600	Fokker 50
MTOM [kg]	22800 [1]	20820 [52]
$C_{L_{max}}$ in take-off condition	2.44 [53]	2.2 [52]
Wing span [m]	27.05 [1]	29 [54]
Aspect ratio	12 [1]	12 [54]
Wing surface [m^2]	61 [1]	70 [54]
Take-off field length (MTOM, ISA-SL) [m]	1333 [1]	1190 [55]
Take-off power (normal/max.) [kW]	1846/2051 [1]	1678/1864 [56]
Propeller diameter [m]	3.93 [1]	3.65 [57]

5.2. Take-off speeds

The take-off run is sketched in Figure 5.1. The V-speeds are defined by the Federal Aviation Regulations. One engine fails at speed V_{EF} which is close to V_1 to account for pilot reaction. The failure of an engine at speed V_{EF} results in an equal length for a rejected take-off and a continued take-off at V_1. For certification V_{EF} and V_1 are selected by the applicant. The balanced field length can be computed if a calculation of the emergency breaking procedure is made. In favour of estimating the breaking capacity of the aircraft the following assumptions for the V-speeds are made:

$$V_{EF} = 1.05 V_S \qquad V_1 = V_{EF} \qquad V_R = 1.1\ V_S$$

The remaining speeds can be determined from [8] as:

$$V_S = 0.94\left(\frac{2W_{TO}}{\rho S C_{L\max}}\right)^{\frac{1}{2}} \tag{5.1}$$

$$V_2 = \left(\frac{2W_{TO}}{\rho S C_{L_2}}\right)^{\frac{1}{2}} \tag{5.2}$$

According to Torenbeek [8, p. 265]: "The free air safety speed V_2 is the speed to which the airplane accelerates while climbing away after lift-off with one engine inoperative." The Speed V_2 is calculated from the safety requirement $V_2 \geq 1.2 V_S$, which means $C_{L_2} = 0.786 C_{L\max}$.

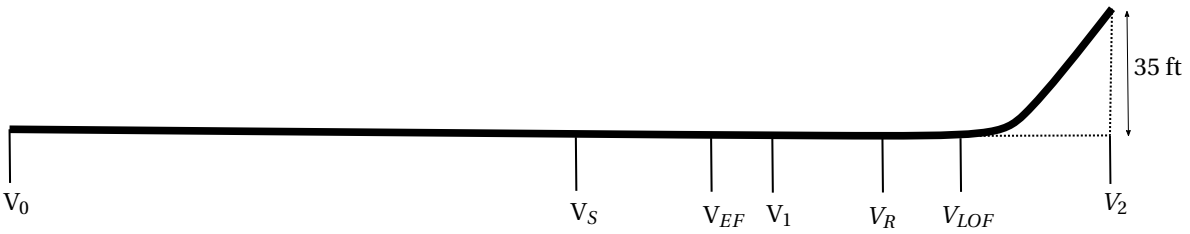

Figure 5.1: Sketch of the take-off run, V-speeds as specified by federal aviation regulation - part 25.107.

5.3. Drag break down

The drag contributions during the take-off are determined in this section. Zero lift drag for the clean ART72-600 is calculated, for the reference case, by the Initiator. For the clean Fokker 50 the aerodynamic data in Obert [52] is used. The zero lift drag for each aircraft is given in Table 5.2. The increase in drag due to the extended landing gear is established by the Engineering Sciences Data Unit[58] as:

$$C_{D_{0,\text{ landing gear}}} = \frac{K \text{MTOM}^{0.785}}{S} \tag{5.3}$$

In SI units with MTOM in kg,

$$K = 0.75 \times 10^{-3} \quad \text{for zero flap deflection}$$
$$K = 0.31 \times 10^{-3} \quad \text{for maximum flap deflection}$$

The increase in zero lift drag due to the extended flaps is difficult to calculate without flap geometry. The contribution of the flap to zero lift drag is *estimated* as 100 counts. The induced drag of the aircraft is calculated as:

$$C_{D_i} = \frac{C_L^2}{\pi e \text{Æ}} \tag{5.4}$$

The Oswald span efficiency e for large turboprop aircraft can be estimated to between .8-.85 [2]. The influence of the flaps on the span efficiency is obtained from Obert. The average increase in the Oswald factor

e due to flap deflection f with engines on wing is given as: $0.0026\frac{\delta e}{\delta f}$. The flap deflection in take-off is 15 degrees and 26.5 degrees for the ATR72-600 and Fokker 50 respectively. The failure of one engine results in an increase in drag. When a turboprop aircraft operates in the OEI condition the failed propeller is feathered and a rudder deflection is required to maintain moment balance. The drag contribution from a feathered, stopped propeller can be estimated from [2] as:

$$C_{D_{\text{prop, feathered}}} = 0.00125BD_p^2 \tag{5.5}$$

The above is a function of the number of blades B and propeller diameter D_p in ft. The asymmetric drag due to the side-slip angle required to maintain moment balance is a complicated calculation of vertical tail induced drag, fuselage drag and the propeller slipstream, torque and asymmetric blade effects. The drag contribution can be estimated by a technical paper of ESDU [59]. This paper provides an empirical relation for the increment in drag increase due to side slip $\Delta C_{D_{\text{asym}}}$ which can be added as a parasitic drag contribution. The drag increase is a function of the parameter:

$$\frac{1}{2\pi}\left(\frac{N_{\text{asym}}}{q}\right)^2\left(\frac{1}{l_f h_f}\right)^2\frac{1}{S} \tag{5.6}$$

with,

$$N_{\text{asym}} = l_p(T + C_{D_{\text{prop, feathered}}}) \tag{5.7}$$

The drag decrease due to ground effect is determined in a previous master thesis project on the Initiator[60]. There are many corrections available to incorporate the ground effects on the lift and drag of the aircraft, see for example [2]. However, this is not the focus of this thesis and is not further investigated. For sake of simplicity the thesis work of Schoustra is used.

Table 5.2: Parasitic drag break down in counts for the reference aircraft.

	ATR72-600	Fokker 50
Horizontal Tail	12	19
Vertical Tail	7	20
Clean Wing	77	81
Wing flaps	100	100
Fuselage	75	54
Nacelles	46	18
Landing Gear	134	109
Total AEO	451	401
Feathered propeller	204	154
$\Delta C_{D_{\text{asym}}}$	273	213
Total OEI	928	768

5.4. Thrust Calculation methods

The thrust generated by the propeller is a function of forward speed. The dependence of thrust on the velocity during the take-off complicates the calculation of the TOFL. The thrust is recalculated for different flight speeds for a settable interval during the take-off run. To account for blade stall and lost power at the initial phase of the take-off a method for predicting the thrust at low advance ratio is required.

Maximum power is used for the take-off run. In combination with the pitch mechanism of a propeller maintaining a constant propeller rpm, the propeller will over pitch at the beginning of the run in order to absorb all available power. The result is stalled blades sections near the root to absorb the torque available. This prohibits an effective transfer of all available power into thrust. Hence a turboprop aircraft will produce maximum thrust at some airspeed where the effective angle of attack is such that the flow over the blade airfoil is fully attached just after the beginning of the take-off.

In the optimization routine the BEM method is used to calculate the take-off performance of the propeller. For the establishment of the take-off tool the actuator disc method is included for reference, this is because the ideal static thrust can be derived from momentum theory. Both methods are unable to provide

an accurate prediction of thrust for the initial phase of the take-off. For low propeller advance ratio and high available power at the beginning of the take-off, some of the assumptions of both methods become invalid. An empirical method for estimation of the static thrust of a propeller has been established by NACA. The NACA static thrust prediction is based on propellers with a Clark-Y profile which has a maximum camber of 3.4%. The method is based on a propeller of comparable power absorption with up to 4 blades. The propellers of the reference aircraft feature 6 blades. In take-off the high loading on the propeller means that the increased number of blades will significantly improve the performance of the propeller at take-off. The NACA method only determines the static thrust (zero advance ratio). A description for the remaining low advance range where the AD and BEM theory fail to make an accurate prediction is not present.

5.4.1. Actuator disc method

Momentum theory is used to derive the ideal performance of a propeller. The theory neglects viscous losses, 3D effects and, in this case, wake rotation. The most pressing shortcoming for low advance ratio calculations is the source of the induced velocity. The theory describes a stream tube over which conservation of mass and momentum are applied. With Bernoulli's principle the propeller performance is described. However the induced velocity in front of the propeller actually originates from the wake of the propeller. This means that at low advance ratio the large induced velocities generated by the propeller cannot be accurately described by this theory.

It is possible to derive the ideal static thrust of a propeller from momentum theory. In this case all power delivered to the propeller is transferred to induced velocity generated by the propeller. From the zero free stream velocity the flow through the actuator disc accelerates to absorb the power with half the increment in velocity occurring in front of the propeller, and half of it behind the propeller:

$$T_{\text{static}} = P^{\frac{2}{3}} (2\rho A_{\text{prop}})^{\frac{1}{3}} \tag{5.8}$$

5.4.2. BEM method

The blade element method of Chapter 3 is fitted with a stall model as described in Chapter 4. The high relative angles of attack the propeller blade sections encounter at low advance ratio are described by this model. However, the propeller has to absorb full take-off power which means a highly loaded propeller. The tip loss correction of Prandtl loses validity for high loading cases. In addition to this, BEM theory relies on momentum theory, which also starts to break down at low advance ratio and high induced velocities.

The take-off accuracy of the BEM module is assessed by comparing the module to a low advance ratio propeller experiment. There are few propeller experiments which have results extending to zero advance ratio available. For an experiment with the necessary data an experiment performed in 1938 is used. In this experiment a 3 bladed propeller with Clark-Y airfoils absorbing a peak power of 600 HP was tested in the following manner: 'The general procedure observed in these tests was to hold the engine speed at a constant value while the tunnel speed was increased by steps to top speed (about 115 miles per hour with propeller operating), after which the tunnel speed was held approximately constant and the engine throttled by steps to zero thrust.' [61] This type of advance ratio control was mimicked in the BEM module with the results shown in Figure 5.2. The prediction of the BEM module at low advance ratio *and* high loading is poor. For these operating conditions the implemented BEM solver over predicts thrust and under predicts power consumption. This means that propeller efficiency is over estimated. Therefore an assumption for the initial phase of the take-off for the BEM model is made.

For the initial phase of the take-off $J < 0.3$, the thrust and power of the propeller is described by the production and absorption at $J = 0.3$. At $J = 0.4$ the propeller is able to pitch and adsorb all power and the BEM code produces accurate results with the assumptions for the tip losses and momentum theory valid. This is shown in the validation study performed with the N250 propeller, Figure 3.3. The power coefficient for the ATR72-600 and Fokker 50 at take-off are $C_P = 0.20$ and $C_P = 0.27$ respectively. At these power coefficients the prediction shows good agreement with the experiment. At $J = 0.3$ the thrust might be marginally over predicted. The implication of this assumption will be discussed in the next section. It will become clear that the initial part of the take-off does not significantly contribute to the TOFL obtained. Rather, the thrust contribution after the failure of the critical engine is crucial for accelerating the aircraft the final few $\frac{\text{m}}{\text{s}}$ to V_2.

At $J = 0.4$ and for the remainder of the take-off the propeller has to absorb the power supplied to the propeller. Before V_{EF} normal take-off power is supplied to the propeller. After the engine failure power is increased to maximum take-off power. The power is absorbed by pitching the propeller blades until the torque required to spin them is equal to the torque supplied by the engine. The pitch schedule mechanism is

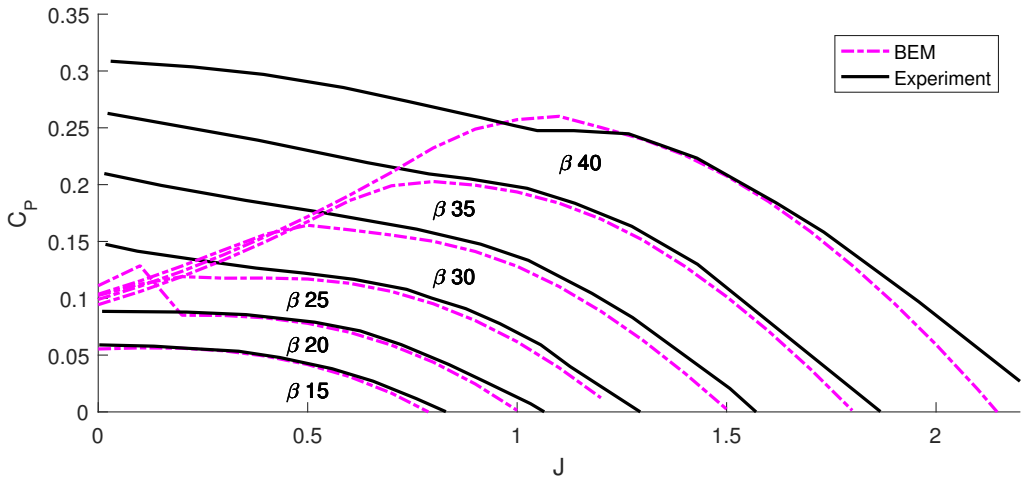

(a) Power coefficient.

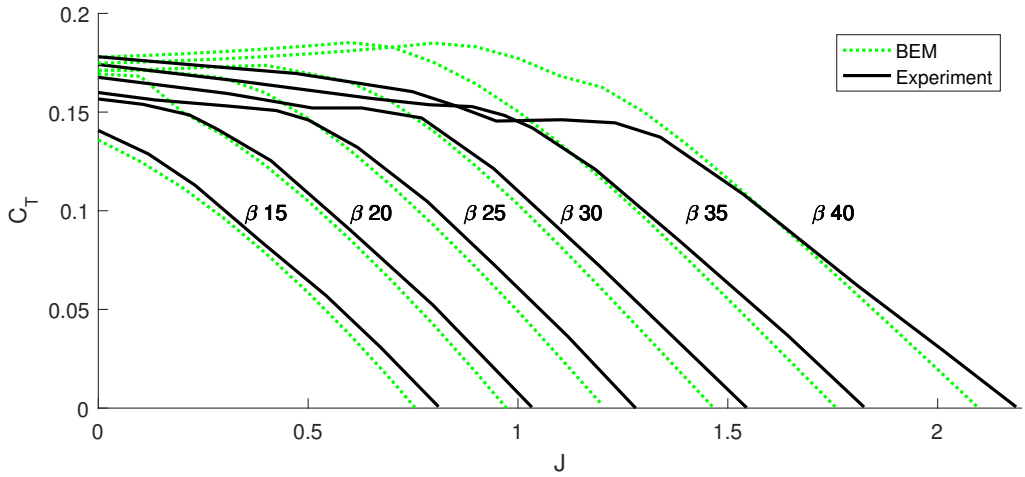

(b) Thrust coefficient.

Figure 5.2: NACA propeller with a 10 ft diameter, 3 blades, Clark-y airfoil, ISA-SL, see reference [61].

explained in detail in appendix A.

For the reference case used to calibrate the take-off module the propeller geometry used for the BEM code is that of the N250 propeller. The diameter of this propeller is scaled to $D_p = 3.93$m for the ATR72-600 and $D_p = 3.65$m for the Fokker 50.

5.4.3. Thrust lapse comparison

The development of the thrust and drag for the Fokker 50 aircraft during the take-off run is shown in Figure 5.3a. In this figure the BEM module with the assumption for the initial part of the take-off is used to calculate the thrust. The static thrust prediction of NACA is also included.

In Figure 5.3b the speed of the aircraft is plotted against distance. The acceleration in the initial part of the take-off is very large but it is the acceleration after the failure of the engine that is critical to the obtained TOFL. An assumption for the initial part of the take-off will not severely impact the results.

5.5. Implementation of the take-off module

The implementation of the take-off module requires calibration before it can be implemented. To do this the take-off run is simulated for two reference cases the ATR72-600 and the Fokker 50. The results of the take-off analysis are given in Table 5.3. It is concluded that the take-off analysis is reliable. The take-off field length of the reference aircraft is not achieved, however the delta's between the two reference aircraft are in

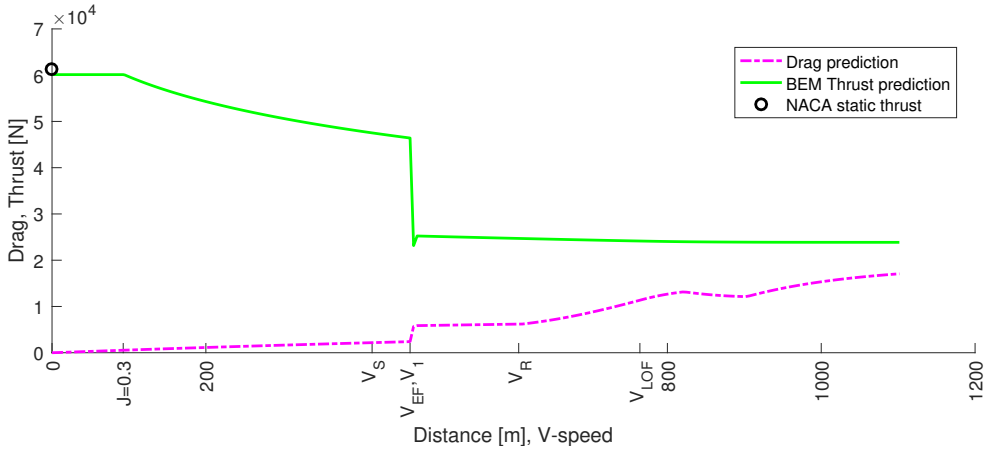

(a) Calculated take-off thrust and drag. Static thrust predicted by Equation (5.8) $T_{static} = 8.9 \times 10^4$N.

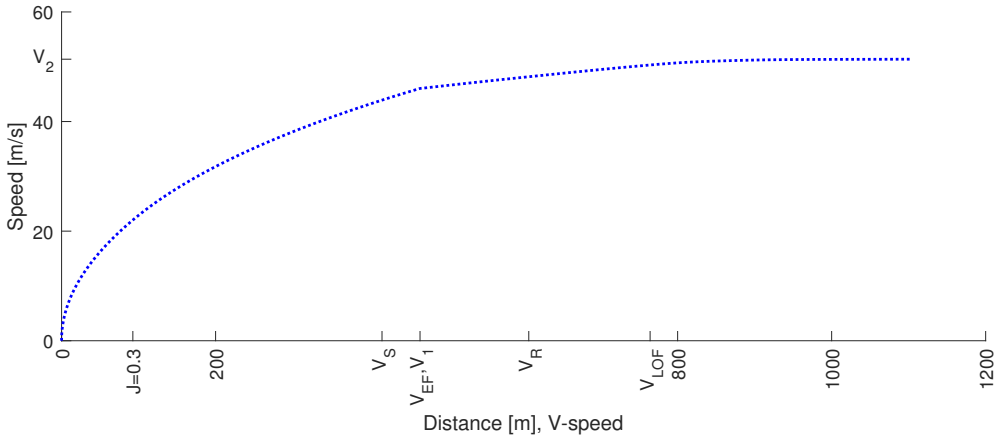

(b) Speed over the take-off run.

Figure 5.3: Calculated take-off simulation for a reference Fokker 50.

close agreement. The TOFL performance of a new propeller design can be assessed by comparing it to the performance of this reference case.

Table 5.3: Calculated take-off field length for reference aircraft.

	Calculated TOFL [m]	Δ Reference
ATR72-600	1236	-7.3%
Fokker 50	1098	-7.7%

6

Structure module

In this chapter the forces acting on the propeller blade are evaluated. A method for incorporating these forces in to a structural constraint on the propeller blade is developed. The distributed forces on the blade and the resulting stresses are calculated with a finite element approach.

6.1. Blade forces

The five main forces on the propeller blade are sketched in Figure 6.1. In this thesis the torque and thrust forces are considered for the structural constraint of the blade. The twisting forces that torque the blade, indicated in the bottom view, are not considered. The centrifugal force is also not incorporated in the structure tool.

Euler–Bernoulli beam theory is used to determine the stress and bending of the propeller blade from the considered forces. Euler–Bernoulli beam theory is valid for cantilever beams of high length to thickness ratio. Some sources state that the theory is valid for ratios of 10 or higher [62], which is generally not reached by a propeller blade. However, Euler-bernoulli has been previously used to model propeller blades [63]. Assumptions of the model taken from [62] are:

Assumption 1: The cross-section is infinitely rigid in its own plane.

Assumption 2: The cross-section of a beam remains plane after deformation.

Assumption 3: The cross-section remains normal to the deformed axis of the beam.

As described by Bauchau et al.[62, p. 175]: "These assumptions are known as the Euler-Bernoulli assumptions for beams. Experimental measurements show that these assumptions are valid for long, slender beams made of isotropic materials with solid cross-sections. When one or more of these condi-

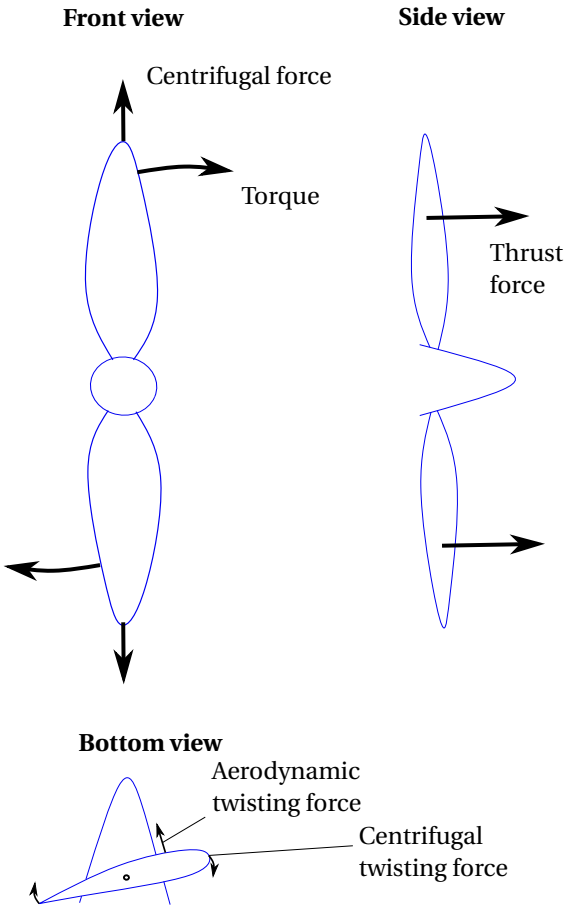

Figure 6.1: Sketch of the main forces on a propeller.

tions are not met, the predictions of Euler-Bernoulli beam theory can become inaccurate." The bending of the beam must also remain small in order for the beam bending theory to remain valid [64]. Assumption 3 only remains true if the bending moments caused by the aerodynamic forces are constant along the length of the beam. If the moments are varied along the beam shear loads are present. However, shear stress is comparatively low in beams with a cross section relatively small compared to their length such that the basic bending theory may be used with reasonable accuracy[65]. The average shear stress $\tau = F_{\text{shear}}/A$ becomes large for thin walled beams and may start contributing significantly when the wall thickness decreases. The accuracy Euler beam theory for this application in this thesis is assessed during a verification of the structure module in Chapter 8.

6.2. Structural element discretization

The aerodynamic forces on the blade are calculated within the BEM module for sections of the blade. The trust T and torque Q delivered or absorbed by the section is taken as the average $\frac{\delta T}{\delta r}, \frac{\delta Q}{\delta r}$ of the two airfoils marking the section on both sides and subsequently integrating over the section length l_s.

$$T_s = \frac{l_s}{2}\left(\frac{\delta T}{\delta r}(i) + \frac{\delta T}{\delta r}(i+1)\right) \tag{6.1}$$

$$Q_s = \frac{l_s}{2}\left(\frac{\delta Q}{\delta r}(i) + \frac{\delta Q}{\delta r}(i+1)\right) \tag{6.2}$$

For the tip section the final airfoil is used to determine the forces for the whole section.

The blade geometry varies over the span and therefore the second moment of area varies as well. To account for this variance in the structural analysis, the choice is made to represent the blade in a finite element method. The thrust and drag are assumed to be applied at the center of the established aerodynamic sections. This is where a node is placed. For the geometric cross section of the section between nodes the airfoil shape is taken. This is sketched in Figure 6.3.

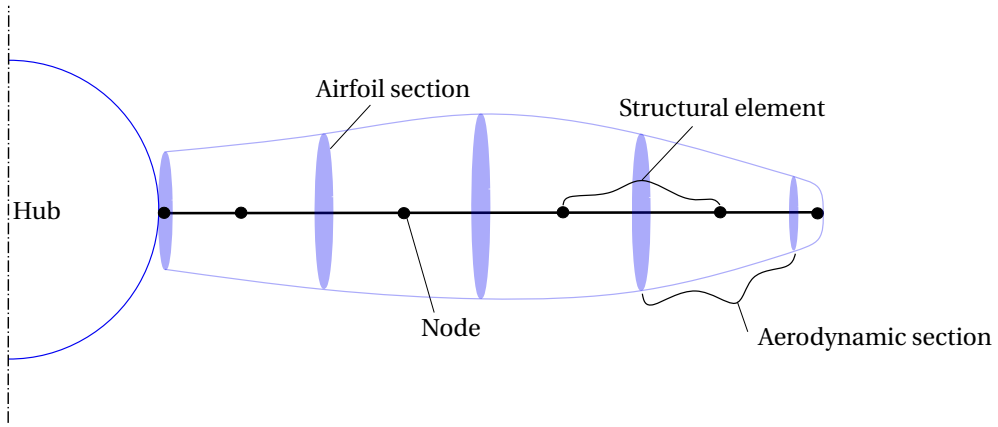

Figure 6.2: Finite element break down of a propeller blade.

6.3. Calculation of normal stress at the blade root

In this section the method for determining the normal stress at the blade root is established. The blade root is the radial location where the blade attaches to the propeller hub. The cross section of the propeller blade at this location has to be large enough to cope with the forces generated by the spinning propeller blade.

6.3.1. Calculation of section properties

The section geometric properties are calculated by an open source Matlab code [66]. This rapidly calculates the second moment of area of an arbitrary shape by dividing the airfoil shaped polygon in segments and summing the contributions of each segment. The segments are build up by two consecutive vertices of the polygon together with the origin of the axis system in which the vertices are defined, thereby forming a triangle. The surface integral for each segment's second moment of area $I_{xx} = \int_A y^2 dA$ is transformed into a line

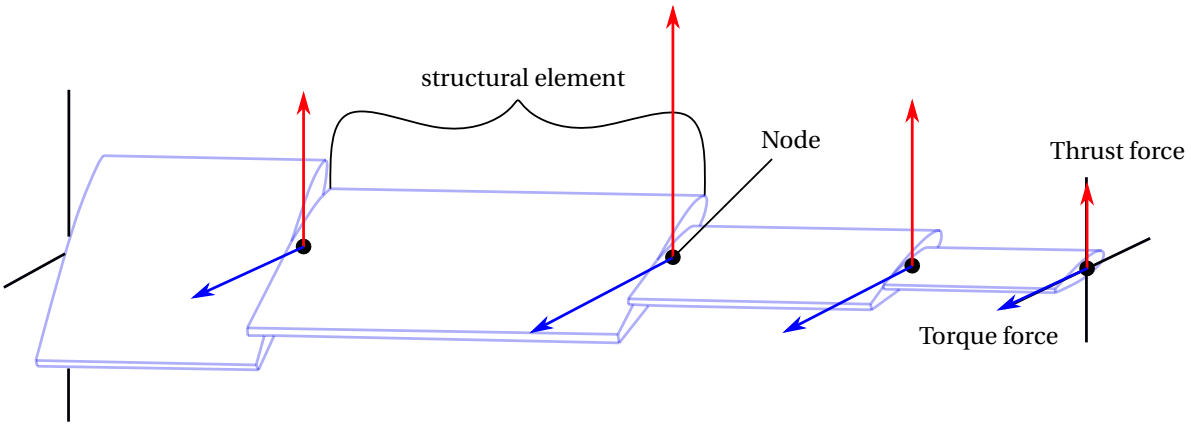

Figure 6.3: Thrust and torque on the propeller blade structural model.

integral using Green's theorem. After the moment of inertia of each segment is calculated around its centroid, the parallel axis theorem [65, p. 512] is used to calculate the moment of inertia around the parallel reference axis for the whole polygon. The procedure is as follows, proof and a detailed derivation of this method can be found in [67]:

First, twice the area of the segment is calculated

$$a_i = x_i y_{i+1} - x_{i+1} y_i \tag{6.3}$$

The area of each polygon with n line segments equals:

$$A = \frac{1}{2} \sum_{i=1}^{n} a_i \tag{6.4}$$

Following this, the centroid location and second moment of area with respect to the x and y axis are given by [67] as:

$$x_c = \frac{1}{6A} \sum_{i=1}^{n} a_i (x_i + x_{i+1}) \tag{6.5}$$

$$y_c = \frac{1}{6A} \sum_{i=1}^{n} a_i (y_i + y_{i+1}) \tag{6.6}$$

$$I_{xx} = \frac{1}{12} \sum_{i=1}^{n} a_i (y_i^2 + y_i y_{i+1} + y_{i+1}^2) \tag{6.7}$$

$$I_{yy} = \frac{1}{12} \sum_{i=1}^{n} a_i (x_i^2 + x_i x_{i+1} + x_{i+1}^2) \tag{6.8}$$

$$I_{xy} = \frac{1}{24} \sum_{i=1}^{n} a_i (x_i y_{i+1} + 2 x_i y_i + x_{i+1} y_i) \tag{6.9}$$

6.3.2. Calculation of the blade stress due to bending

The forces due to thrust and torque on each node are used to establish moment curves and shear curves. This allows the moment and shear force to be determined along the radial distance from the hub. The shear force is used to determine the average shear stress in order to verify that it is of a low enough magnitude to be neglected. The stresses on the blade are determined from the stress distribution due to unsymmetrical bending. If the airfoil shaped cross section is defined in the x-y plane, the normal stress on this plane is calculated by the following equation:

$$\sigma = \left(\frac{M_y I_{xx} - M_x I_{xy}}{I_{xx} I_{yy} - I_{xy}^2} \right) x + \left(\frac{M_x I_{yy} - M_y I_{xy}}{I_{xx} I_{yy} - I_{xy}^2} \right) y \tag{6.10}$$

6.4. Analysis of the structure module results and assumption for the structure constraint

The results of the above calculation method calculate stresses that are of a very large magnitude. These stresses are unrealistic as they would require a material selection and blade geometry that result in an extremely heavy propeller. The calculation methods are implemented correctly. A verification procedure shows this (see Chapter 8); the error of violating some of the assumptions of Eulers theory are within reason. Not including the dynamics particularly bending of the blade is thought to make the results inaccurate. In Appendix B it is shown that the bending moment relief experienced by the blade due to centrifugal force is very significant. In order to incorporate a structure constraint at the blade root an assumption based on a current propeller design is made.

6.4.1. Assumption for propeller structural constraint

In order to incorporate a structural constraint the N250 propeller[28] is used. The bending forces of this propeller are calculated for a reference case whereby the N250 propeller is scaled to the dimensions of the ATR72-600 propeller and the normal stresses are calculated by the method of Section 6.3.2. The root airfoil of the N250 with a thickness to chord ratio of 23.5% is taken as solid. On this solid cross section the maximum stress is computed for a reference case in climb. This stress will be the structural constraint for new propeller designs. The stress on new designs will be calculated at the solid root airfoil shaped cross section. The assumption made by this procedure is that the propeller blade is constrained in normal force resulting from thrust and torque forces only.

6.4.2. Consequence of limited structure tool

The structure tool ensures that a propeller design will have a blade root that resembles a realistic propeller. However, the structure module has quite a few short comings. The only forces that are accounted for are the steady state thrust and torque force. The steady state centrifugal force is not considered. This force is quite large but because it acts axially the magnitude of the stress generated at the blade root is modest. For the verification case calculated in Chapter 8, the normal stress due to centrifugal force is an order of magnitude lower than the stress due to bending.

A further stress on the propeller blade that is not accounted for are due to the harmonic loads. If the propeller operates in the climb condition the propeller inflow angle will be at an angle of attack. This means that the geometric angle of attack on the blades (sketch 3.1) will be different for the upcoming blade than the down going blade. This will introduce a moment across the propeller. But more importantly, the cyclic loading means that that propeller blades are subject to high-cycle fatigue. Furthermore, due to this cyclic loading on the propeller or other factors introducing a vibration on the propeller the blades can experience flutter. The vibratory modes also known as resonant frequencies, must be calculated in order to incorporate this in the design. To mitigate flutter occurring the propeller blade must be made stiff enough.

Blade retention, the inertia of the propeller and the gyroscopic forces that can be induced when the aircraft changes attitude are also not evaluated. The restorative moment due to centrifugal force is ignored. This effect increases with the diameter. The flexibility of the blades also influences the restorative force. A blade that deflects more under the forces of flight will experience a larger restorative moment due to this deflection.

Blade root normal stress as a failure point

In this thesis only the normal force is calculated. More appropriate would be calculation of the von Mises yield criterion. This would ensure that at the root not only the normal stress but entire contribution of shear and normal stresses in three dimensions are incorporated. Furthermore, not only the root of the blade but the von Mises stress in the whole blade should be checked. It is possible for a blade to have its failure point at a different location than the the blade root.

Using the N250 propeller for the structural constraint

The structural stress constraint on the blade root is calculated from the N250 propeller. This propeller is a wind tunnel scale model for the N250 aircraft. This propeller aircraft was designed to fulfill a similar roll as the ATR72. It is a reasonable assumption that the structural constraints of this propeller translate to new designs. The propeller fitted on the IPTN N-250-100 aircraft featured a diameter of 3.81 meter[68]. However, the technical paper of the NLR documenting the N250 propeller is not clear on the exact diameter of the propeller it represents nor the quality of structural design of the propeller. Furthermore, scaling the propeller to a larger diameter could mean a scaling error; the surface area of the blade root may not increase according to the stress.

7

Mass estimation module

In this chapter the mass estimation of the propulsive unit is established. The total mass of the propulsive unit is estimated by following Roskam Part V: Class II method for estimating power plant weight[3]. This method distinguishes four sub assemblies. These are given in Table 7.1. The mass for each sub-assembly is estimated. A deviation from Roskam is made for the mass estimation of the engine. For this research the engine mass estimation is split into two parts: the gas turbine and the gearbox. The gearbox mass is estimated separately to allow the effect of gear ratio on the mass of the propulsive unit to be established. The gear ratio changes with propeller rpm. The tip speed constraint ties the rational rate to the propeller diameter. A second deviation made is for the mass estimation of the nacelle of the propulsive unit. Roskam groups this in the structure breakdown of the aircraft mass. However, since the engine mass is the only variable of this mass, it is incorporated in the mass of the propulsive unit. For a propeller aircraft, the nacelle mass includes the air induction system mass [3]. The nacelle mass is computed as a corrective factor times the engine mass. The total mass of the propulsion unit is given as:

$$m_{pp} = m_{eng} + m_{prop} + m_{ps} + m_{nacelle} \tag{7.1}$$

Table 7.1: Propulsive unit sub assemblies.

Sub assembly	Components
Engine, m_{eng}	Gas turbine Gearbox
Nacelle, $m_{nacelle}$	Air induction system Nacelle
Propeller, m_{prop}	Propeller
Propulsion systems, m_{ps}	Engine controls Starting systems Propeller controls Provisions for engine

7.1. Engine mass estimation

The engine of a turboprop aircraft consists of a gas turbine and gearbox. Aircraft design hand books have methods available for estimating the engine mass. Examples of these methods can be found in Roskam[3] and Raymer[4]. These methods rely on statistical relations between take-off power and engine mass. The methods in these handbooks are somewhat dated. More recent statistical data for aircraft engine's is available. Janes aero engines[10] is an excellent source for turboprop engine properties. Previous editions of this source have been used in the handbooks previously mentioned. However, Janes aero engines has a limited amount

of data available about these engines. In this research the choice is made to establish a mass estimation method relying solely on derivations of the PW100 series engine for statistical data. This means that the engine resulting from the optimization is a rubber engine that is scaled from the PW100 series. A large variety of aircraft uses the PW100 series, including the ATR72 and Fokker 50.

The choice of basing an engine mass estimation on one engine type allows an increase in accuracy for engine and gearbox mass estimation. An EASA type-certificate data sheet is used to gather a wide range of engine properties. This data sheet has a large set of engine data for 23 derivations of the PW100 engine, ranging in maximum take-off power from 1625-2051 kW. This source specifies: dimensions, weight, power (max. take-off, norm. take-off, max. cont.), turbine inlet temperatures, rpm for LP spool, HP spool and output shaft for all conditions. This data allows an accurate estimation of the mass fraction of the gearbox. The downside is that higher engine power requires extrapolation of the data. Including engines of higher power in the regression would require a much large data set in order to still make statistical relation accurate. This is due to possible differences in engine layout. For example an engine with higher power, the PW150 of the PW150 series (P_{max} = 3781kW) used for the Bombardier Dash 8, uses a different layout of 3 axial compressor stages versus a 2 stage centrifugal unit used in all PW100 series engines.

Statistical relation for PW100 series engine

The same regression equation as the handbook methods will be used to fit the EASA data. The standard error determines the goodness of the fit. The standard error represents the distance between the reference data and the regression line. The regression line for the PW100 series engine, with m_{eng} in kg, has a standard error of 1.93 and is given as:

$$m_{\text{eng}} = 10 P_{\text{max}}^{0.266} \tag{7.2}$$

This regression line is plotted against reference data in Figure 7.2.

7.2. Gear box mass estimation

The bounds of engine design have been set to the PW100 series engine. The low pressure spool connected to the gearbox of the PW100 series spins at 28800 rpm +/- a small margin (1%). The output rpm for all engines of the PW100 series is set to 1212 rpm with the exception of the PW119B/PW119C, which is fitted to the Dornier 328. This engine's output shaft rotates at 1339 rpm when at maximum take-off rpm. For the design of the propulsion system the propeller rpm is included as a design variable. This means that the gearbox is sized separate from the engine. The gearbox mated to the PW100 series is assumed to be supplied by a constant input rpm of 28800. For design purposes in this thesis it is assumed that a gearbox of variable size and weight can be mated to the rubber engine of the PW100 type.

In order to determine the gearbox mass four methods are assessed. Some of these methods include all gearbox subsystems in the mass estimation, others do not. Turboprop aircraft like the ATR72 are fitted with a clutch. This allows the drive to be separated from the propeller on the ground to allow the motor to operate in hotel mode. This eliminates the need for an APU. The clutch assembly is part of the gearbox and will have to be included in the mass estimation. The methods assessed in this chapter are depicted in Table 7.2

Table 7.2: Gearbox mass estimation methods.

Method	Year	$f(X)$	Derived from	Inc. accessories
NASA '15 [69]	2015	$f(P_{\text{motor}}, \omega_{\text{motor}}, \omega_{\text{rotor}})$	Empirical data	Yes
Havey & Kline [70]	1989	$f(P_{\text{motor}}, \omega_{\text{motor}}, \omega_{\text{rotor}})$	Empirical data	No
NASA '83 [71]	1983	$f(P_{\text{motor}}, \omega_{\text{motor}}, \omega_{\text{rotor}})$	Empirical data	Unknown
Willis [72]	1963	$f(P_{\text{motor}}, \omega_{\text{motor}}, N_{pl}, K)$	Physics, empirical calibration	No

NASA '15

This gearbox mass estimation method is based on empirical data of 52 rotorcraft. The average error of the mass estimation method is 8.6%. This method includes the gearbox accessories' mass. As described by Johnson[69, p. 136]: "The conventional rotor drive system clutch and free wheeling device weights are included in the gear box equation." m_{gb} is given in lbs.

$$m_{\text{gb}} = 95,7634 N_{\text{rotor}}^{0.38553} P_{DS\text{limit}}^{0.78137} \frac{\omega_{\text{eng}}{}^{0.09899}}{\omega_{\text{rotor}}{}^{0.80686}} \tag{7.3}$$

Havey & Kline

This method is developed for STOVL vehicles, which use wet clutches. The mass of the clutch is excluded in the mass estimation method. The method is based on Hamilton Standard and Allison APET empirical data. This data stems from 1963. With m_{gb} in lbs and Q in pound-foot:

$$m_{gb} = 0.0801 Q^{0.84} \tag{7.4}$$

NASA '83

A gearbox mass estimation method for propeller powered aircraft. Valid for inline gearboxes designed to operate on engines between 1000 to 2500 shaft horsepower. There is no mention of gearbox accessories or the nature of the empirical data source. m_{gb} is given in lbs, Q in pound-foot.

$$m_{gb} = (0.0174Q + 45)\left[\frac{0.118}{GR}\right]^{0.5} \tag{7.5}$$

Willis 1963

Willis determines the gearbox mass by the assumption that the mass is proportional to the volume of the gears. The optimum number of planets in a planetary gear set resulting in minimal gearbox mass can be estimated by:

$$N_{pl} = \frac{16.3677}{3\sin^{-1}\left(\frac{GR-1}{GR+1}\right)\cdot 1.1736} \tag{7.6}$$

The gearbox mass can then be determined by:

$$m_{gb} = 0.5\frac{P}{K\cdot\omega_{eng}}\left(\frac{1}{N_{pl}} + \frac{1}{N_{pl}\cdot GR_s} + GR_z + GR_z^2 + \frac{0.4\cdot GR^2}{N_{pl}\cdot GR_s} + \frac{0.4\cdot GR^2}{N_{pl}}\right) \tag{7.7}$$

with,

$$2GR_s^3 + GR_s^2 = \frac{0.4GR^2 + 1}{N_{pl}} \tag{7.8}$$

The Willes method includes a correction factor to calculate the gear box mass to the state-of-the-art. The correction factor is the surface durability. This is calibrated to be $K = 0.774\frac{\text{m}^2}{\text{s}^2}$ [73]. m_{gb} is given in lbs, P as foot-pound. The calculated mass is not including gearbox auxiliaries/clutch.

Evaluation of gearbox mass estimation methods

The four gearbox mass estimation methods are plotted in Figure 7.1 for a range of power transmittances and gear ratio's. The Havey & Kline method calculates gearbox mass without auxiliaries. The Willis method also excludes this mass. While it is mentioned that NASA '15 method includes the mass of the auxiliaries, this is not stated in the NASA '83 paper. When it is assumed that the difference between the methods is caused by the gearbox auxiliaries, good agreement between the methods is found. The methods are in closest agreement between 1100 and 1400 rpm for the case where the input rpm is maintained at 29900. This is the operating range of most turboprop aircraft. There exists a variance in slope between the methods for the range of gear ratios evaluated. NASA '15 and Havey & Kline predict a less rapid increase in mass then the other methods.

The NASA '15 method is selected as the gearbox mass estimation method because it uses a large data set, with acceptable average error and has a recent publication date. However, the source and age is of the reference data is not known. Using the other methods in the tool can be done to research the effect of gearbox mass on propeller design. This research is not performed in this thesis.

7.3. Gas turbine mass estimation

In Section 7.2 the NASA '15 method is selected to calculate gearbox mass. To determine the gas turbine mass separate from the gearbox, a new mass estimation method for the gas turbine is made. The reference data of the PW100 has its calculated gearbox mass subtracted by the NASA '15 method and the result is used to calibrate the gas turbine mass estimation equation. The gas turbine mass estimation follows the same model as the engine mass estimation and the equation is established, with m_{gt} in kg, as:

$$m_{gt} = 1.26 P_{max}^{0.378} \tag{7.9}$$

The average error of this regression is 1%. The gas turbine mass estimation method is plotted against calculated data in Figure 7.2

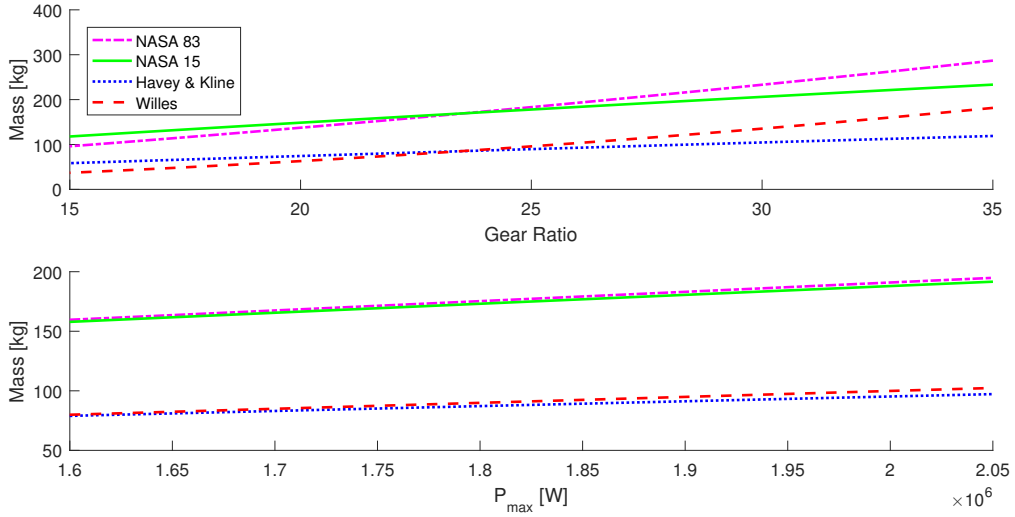

Figure 7.1: Gearbox mass variation with GR and Power. The typical GR of PW100 = 24.

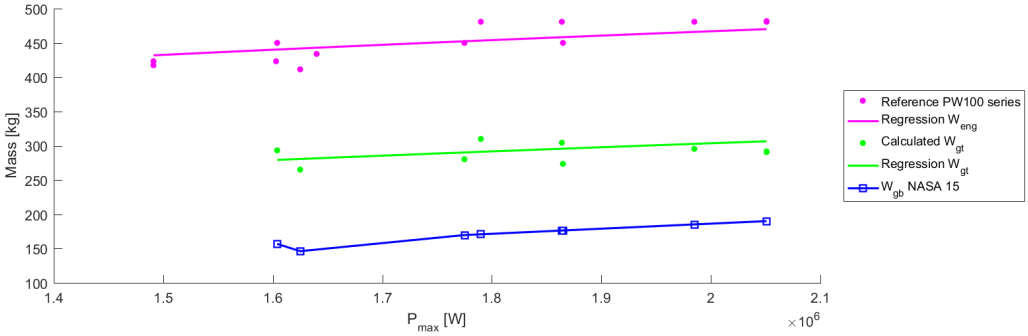

Figure 7.2: Mass estimation of gearbox, gas turbine and their sum: the total engine mass.

7.4. Propeller mass estimation

This section evaluates existing propeller mass estimation methods. The methods are rejected because a new mass estimation method for propellers based on recent propeller data can be made.

Torenbeek propeller mass estimation

The Torenbeek method is an empirical relation for installed propeller mass as a function of the power adsorbed by the propeller. The data used by Torenbeek for this regression is some what dated. Relying on older generation aircraft such as the Fokker F27 and Grumman Gulfstream I.

$$m_{\text{prop}} = 0.108(N_{\text{prop}})^{0.218}\left[D_p P_{TO}\sqrt{B}\right]^{0.782} \tag{7.10}$$

With m_{prop} in lbs and D_p in ft.

NASA mass estimation

This method is also based on empirical data and stems from 1983. The method calculates propeller mass without the system mass. To use the mass estimation method the activity factor of the propeller needs to be known. The activity factor is a function of the propeller blade geometry. Because the activity factor influences the mass estimation, the method can calculate propeller mass with higher fidelity. However, it is not possible to calibrate the method with the data of Table 7.3 due to the geometry of these propellers being unknown. A further disadvantage of using a mass estimation method based on activity factor is that it favours designs with a low activity factor. The structural limitations of a propeller blade with a low activity factor are not

calculated. The NASA propeller mass estimation is:

$$m_{\text{prop}} = K_W \left[\sqrt{M+1} \left(\frac{D_p}{10} \right)^2 \left(\frac{B}{4} \right)^{0.7} \left(\frac{AF}{100} \right)^{0.75} \left(\frac{\text{rpm } D_p}{2 \times 10^4} \right)^{0.5} \left(\frac{\text{SHP}}{10 D_p^2} \right)^{0.12} \right] \tag{7.11}$$

With the scaling parameter $K_W = 355$ and the propeller diameter D_p in feet, m_{prop} in lbs.

Torenbeek adjusted

The choice is made to adjust Torenbeek's regression to one for the propeller weight excluding systems. Table 7.3 is used for this adjustment. The following regression is found:

$$m_{\text{prop}} = 1.1 \left[D_p \, P_{\text{max}} \sqrt{B} \right]^{0.52} \tag{7.12}$$

which has a good accuracy for the data points. The goodness of the fit is determined to be a standard error of 1.73%.

Table 7.3: Propeller mass database.

Propeller	Aircraft	B	D_p [m]	rpm	P_{max} [kW]	m_{prop} [kg]	source
Hamilton F568	ATR72-500/600	6	3.93	1200	2050	165	[57]
Hamilton 14SF-5	ATR42-300	4	3.96	1200	1470	142	[57], [1]
Dowty R408	Dash-8	6	4.12	1020	3782	252	[74]
Dowty R352/R410	Fokker 50	6	3.65	1200	1864	172	[57]
Dowty R381	Saab-2000	6	3.81	1100	2786	227	[57]
Harzell HC-E5N	Piaggo Avanti	5	2.16	2000	634	81	[57]
Harzell HC-B3TN-3D	de Havilland DHC6	3	2.59	2110	462	50	[57]

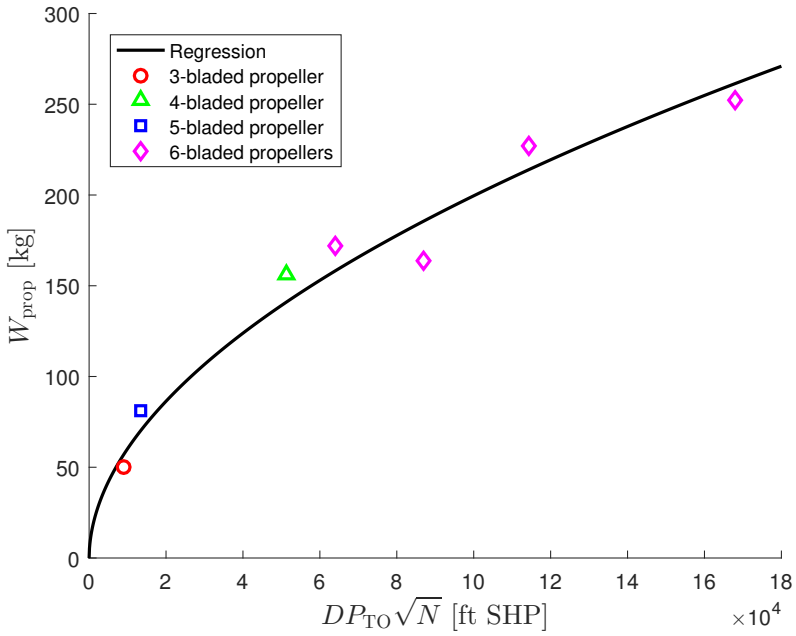

Figure 7.3: Propeller mass estimation.

7.5. Mass of propulsion systems

This section describes the propulsion control systems mass break down taken from Raymer[4]. The system masses consist of: engine controls mass m_{ec}, starting systems mass m_{ess}, propeller control systems m_{pc} and

the engine provisions (oil system and oil cooler) m_{osc}. With m is in lbs, P_{TO} in hp and D_p in ft, the total system mass is given as:

$$m_{\text{p}} = m_{\text{ec}} + m_{\text{ess}} + m_{\text{pc}} + m_{\text{osc}} \tag{7.13}$$

with,

$$m_{\text{ec}} = 56.84 \left[\frac{(l_{\text{fuselage}} + b) N_{\text{eng}}}{100} \right]^{0.514} \tag{7.14}$$

$$m_{\text{ess}} = 50.38 \left[\frac{m_{\text{eng}}}{1000} \right]^{0.459} \tag{7.15}$$

$$m_{\text{pc}} = 0.322 B^{0.589} \left[\frac{B D_p P_{TO}}{1000 N_{\text{eng}}} \right]^{1.178} \tag{7.16}$$

$$m_{\text{osc}} = 0.07 m_{\text{eng}} \tag{7.17}$$

8 Verification

In this chapter a verification of the mass estimation module is performed. Subsequently, the calculations of the structural stresses on the blade root are verified for a given blade geometry. The verification of the blade normal stress calculation is done by comparison to a finite element analysis. Finally, the aerodynamic tool developed in Chapter 3, discretized the propeller blade in a number of aerodynamic sections. The influence of the defined number of sections is investigated.

8.1. Verification of the propulsive mass

The computation of the propulsive mass can be verified by a mass break down performed in Obert [52]. The result of the verification is given in Table 8.1. Based on this verification case it is established that the mass estimation module produces the correct outputs.

Table 8.1: Mass verification of the propulsive unit.

	Reference mass [kg] [52]	Mass estimation tool [kg]
Gas turbine	-	270
Gear box	-	148
Start systems	-	22
Propeller controls	-	10
Provisions	-	29
Propeller	-	141
Total equipped engine	606	620
Nacelle	183	125
Engine control system	37	46
Total propulsive mass	826	791

8.2. Verification of the structure module

The structural module is verified by a finite element analysis. The FEA is performed in ANSYS. Two models of a propeller blade are used. As described in Chapter 6, the structural module models the blade as a cantilever beam with airfoil shaped elements. This model is constructed in ANSYS and it is shown in Figure 8.1a and will be called 'Section FEA'. It is a representation of the geometry as implemented in Matlab. An actual propeller blade will have a smooth transition between the sections. To determine the difference this has on the structural properties this type of blade is modeled as well. This blade is depicted in Figure 8.1b and will be called 'Loft FEA'. The verification is done for one propeller blade geometry and one load case. The conditions of this case are given in Table 8.2 and 8.3.

8.2.1. Second moment of area verification

The second moments of area determined in the Matlab script are verified separately with SolidWorks. This program offers the option to calculate the second moment of area from a supplied set of coordinates. The

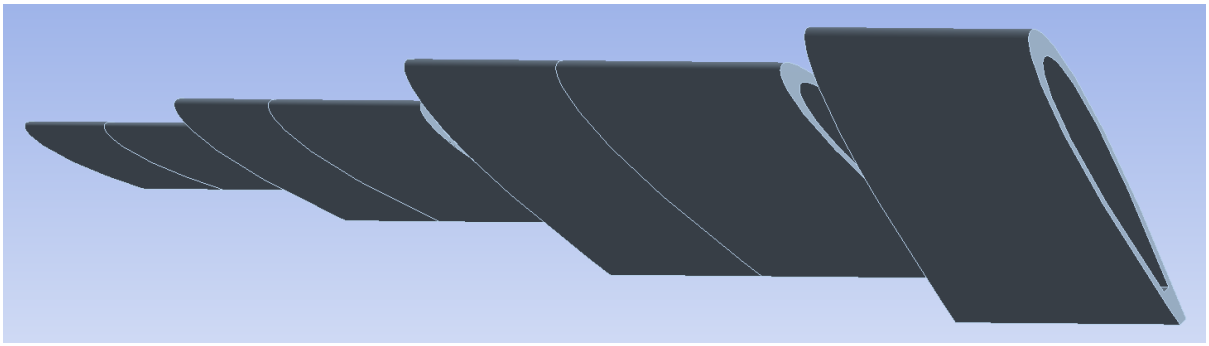

(a) Section FEA.

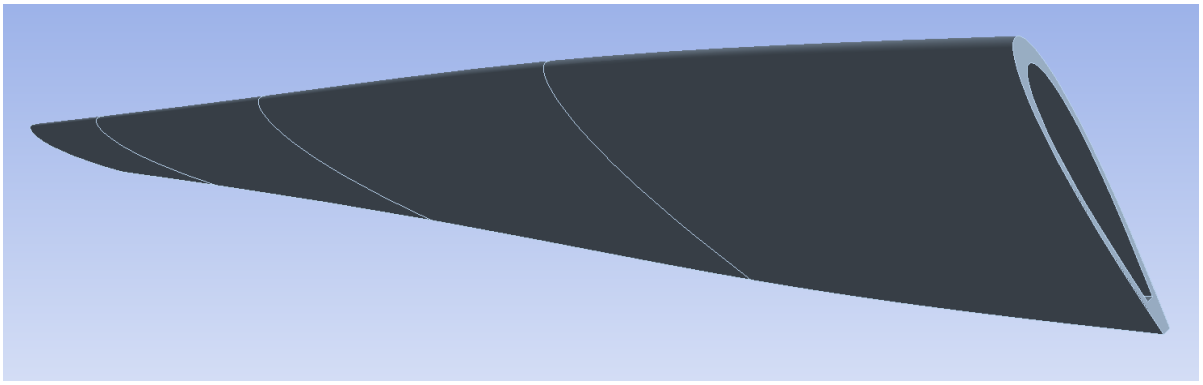

(b) Loft FEA.

Figure 8.1: Blade geometries in ANSYS.

Table 8.2: Propeller blade properties.

Parameter/variable	Value
Number of sections	4
β angles (hub to tip)	[53 35 25 20]
Section chord length [m]	[.4 .4 .3 .2]
Airfoil (all sections)	NACA 0012
Diameter [m]	4
RPM	1100
Hollow chord fraction	0.8

results are depicted in Table 8.4. The second moments of area are calculated from the centroid with respect to the global x and y axis such that $\beta = 0$ when the chord line is equal to the x-axis. The results show that the Matlab calculations are accurate.

8.2.2. Verification of root section normal stresses

The propeller blade root stresses are verified for two cases. Case 1 shows the blade root normal stress when thrust and torque are applied. For Case 2 the centrifugal forces are added. The centrifugal forces were originally thought to be included in the structure tool. Ultimately the centrifugal loads are not included due to absence of blade mass data. Because the verification procedure is performed for a given blade geometry, the mass of the blade can be calculated. The centrifugal forces are therefore included in the verification procedure.

For the mass calculation the density of the aluminum alloy is set at 2770 $\frac{kg}{m^3}$. The mass of the propeller blade Section FEA model is the same as calculated in Matlab. The lofted blade shows an increase in mass of 2.5%. This difference will vary with the number of sections and the β-angle distribution. In Table 8.5 the mass results are given.

The computed stresses are depicted in Figure 8.2 and summarized in Table 8.6. The magnitude of stress

Table 8.3: Forces on the nodes of the blade.

Forces & nodes	
Node location from hub [m]	[.31 .83 1.17 1.41]
Thrust force vector [N]	[8500 11500 7000 3500]
Torque force vector [N]	[7000 5500 2500 1500]
Centrifugal force vector [N]	[32500 95600 48800 18000]

Table 8.4: Second moments of area calculations.

	Matlab			SolidWorks		
	Ixx	Iyy	Ixy	Ixx	Iyy	Ixy
Airfoil section 1	4.0×10^{-5}	2.3×10^{-5}	2.9×10^{-5}	4.0×10^{-5}	2.3×10^{-5}	2.9×10^{-5}
Airfoil section 4	5.1×10^{-6}	3.4×10^{-6}	1.2×10^{-6}	5.1×10^{-6}	3.5×10^{-6}	1.2×10^{-6}

Table 8.5: Blade mass calculation results.

Propeller mass	
Loft FEA	14.3 kg
Section FEA	13.9 kg
Matlab	13.9 kg

varies between the methods. However, the variation is acceptable when it is considered that the Matlab method does not iterate between the bending solution and the stress solution and that some of Eulers assumptions are violated. The asymmetry of stress, the difference between the delta of minimum stress to zero and maximum stress to zero, is large for the Matlab calculation. This asymmetry is graphically depicted in Figure 8.2 as the location between minimal en maximal stress. This difference is suspected to be caused by the bending of the member included by the ANSYS calculation but not in Matlab. The superposition assumption for centrifugal stresses can be assumed valid. When the Loft FEA and Matlab calculation are considered it is shown that the centrifugal stress can be added to the stress solution of pure bending. The Section FEA solution shows a curious result as the addition of the centrifugal produces a large asymmetry in the stress at the blade root. This fortifies the suspicion that bending influences the stress results and is the cause for some of the discrepancies between the Matlab and ANSYS method.

Table 8.6: Calculated blade root stress in ANSYS and Matlab.

	Case 1		Case 2	
	Maximum stress [Pa]	Minimum stress [Pa]	Maximum stress [Pa]	Minimum stress [Pa]
Loft FEA	7.2×10^8	-7.2×10^8	7.5×10^8	-6.8×10^8
Section FEA	6.8×10^8	-6.9×10^8	8.1×10^8	-6.9×10^8
Matlab	6.4×10^8	-5.2×10^8	6.8×10^8	-4.8×10^8

8.3. Influence of the number of aerodynamic blade sections

A propeller blade is parameterized into a number of sections to allow the selected BEM method to calculate propeller performance. The influence of the number of sections on the performance is determined in Figure 8.3. The number of sections is varied for a single analysis point of the N250 propeller. Two spacing methods are investigated: a linear distribution of sections over the span as well as a half cosine spacing. The latter spacing method features a decrease in section length from hub to tip.

The number of sections and the distribution of section length has two main implications on the accuracy of the representation of a propeller. First, the number of sections determines the accuracy of the geometry representation. For example, a curvy propeller would require more sections to accurately describe its varying geometry then a propeller which is straight and tapered towards the tip. Second, the number of sections is also used to approximate the integral of thrust and torque over the blade span. Again the number of sections that is best to approximate the integral is dependent on the variation of thrust and torque distribution across the span. Typically maximum circulation is present around 75% blade span measured from the blade hub.

Table 8.7: Deviation from mean C_T , half cosine spacing, analysis point: scaled N250 propeller, J = 0.7, rpm=1200, D_p=3.93m, NACA 4-series equivalent airfoils.

Deviation C_T coeffient with half cosine spacing									
Number of sections	2	3	4	5	6	7	8	9	10
Deviation from mean %	-56	-5.9	-4.1	-1.5	-2.6	-1.4	0.3	0.4	-0.3

The circulation distribution from hub to the maximum follows an approximately linear development, past its maximum the circulation intensity quickly falls to zero towards the tip. The exact shape of the curve past maximum is dependent on the tip loss factor. However, it can be deduced that the maximum curvature of the circulation distribution line lies some where around its maximum for typical circulation distributions.

The number of sections evaluated directly impacts optimization time. This can be seen in Figure 8.3. The half cosine spacing shows a more stable convergence as the calculation time varies linearly with the number of sections. A linear spacing distribution shows a more erratic behavior. The reason for this is unknown. The BEM module is the most computationally expensive module in the optimization routine. The number of sections has a large impact on the total time of the optimizer. It is therefore of interest to the designer to select as few sections as possible. For this research the following assumption is made: A propeller design for conventional turboprop aircraft will not result in novel designs. Therefore a conceptual blade can be designed with 5 sections distributed along the span at radial locations r/R = [hub .54 .77 .88 .99]. The significance of the error introduced by using 5 sections has to be accounted for in assessing the results of the optimization.

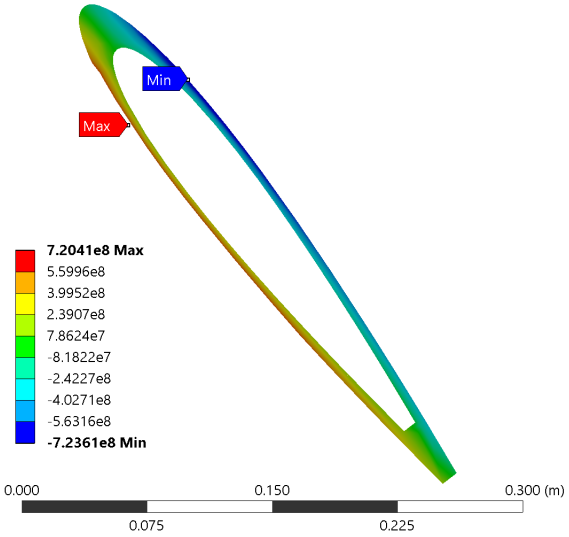

(a) Loft FEA, Case 1.

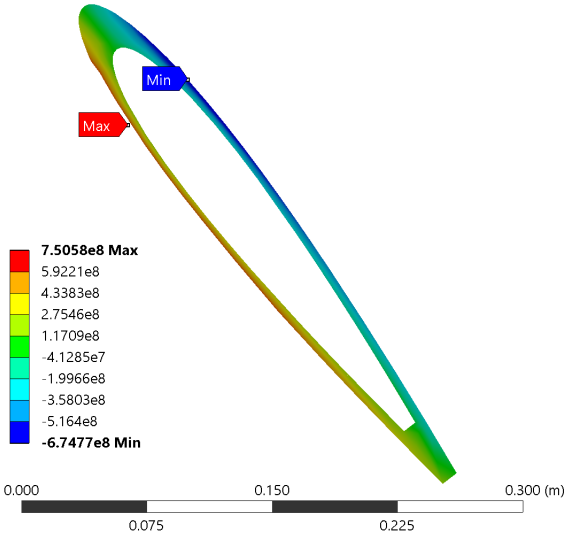

(b) Loft FEA, Case 2.

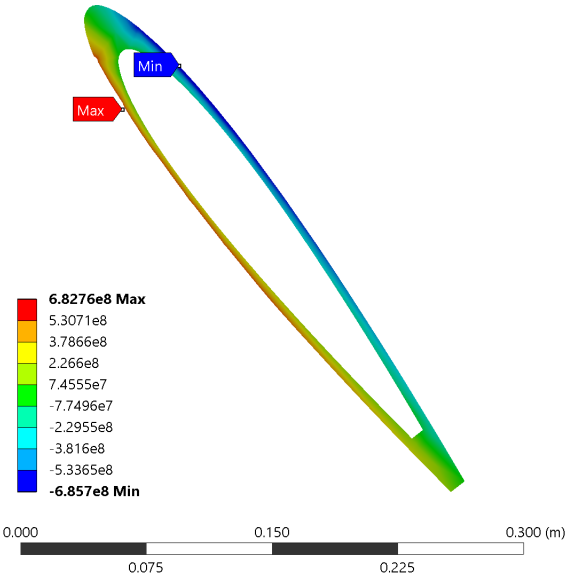

(c) Section FEA, Case 1.

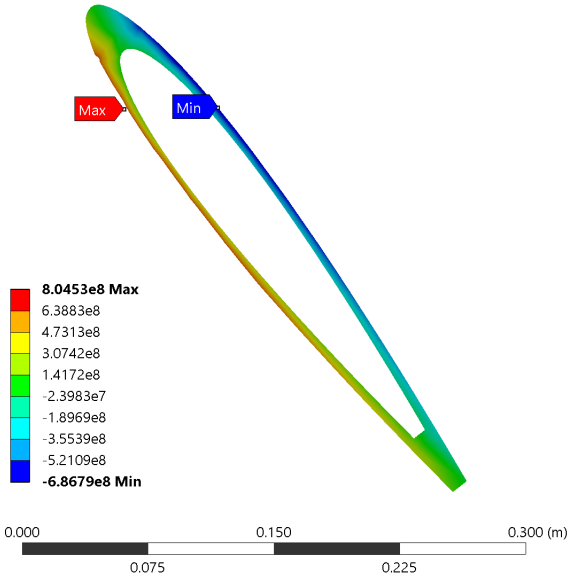

(d) Section FEA, Case 2.

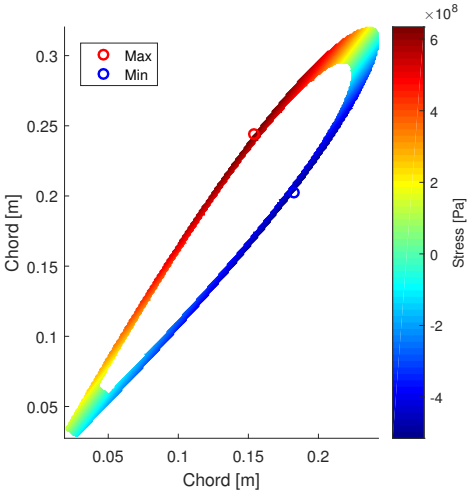

(e) Matlab, Case 1.

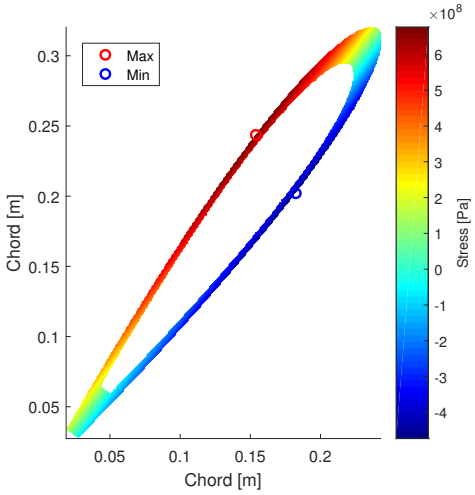

(f) Matlab, Case 2.

Figure 8.2: Normal stresses calculated at blade root.

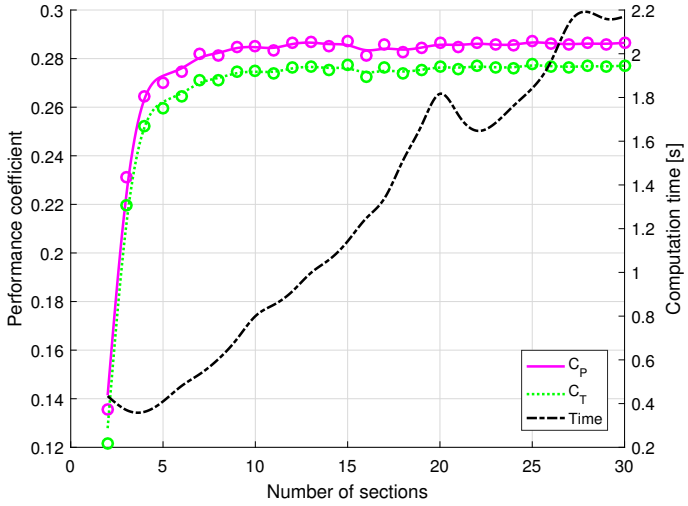

(a) Linear spacing of sections.

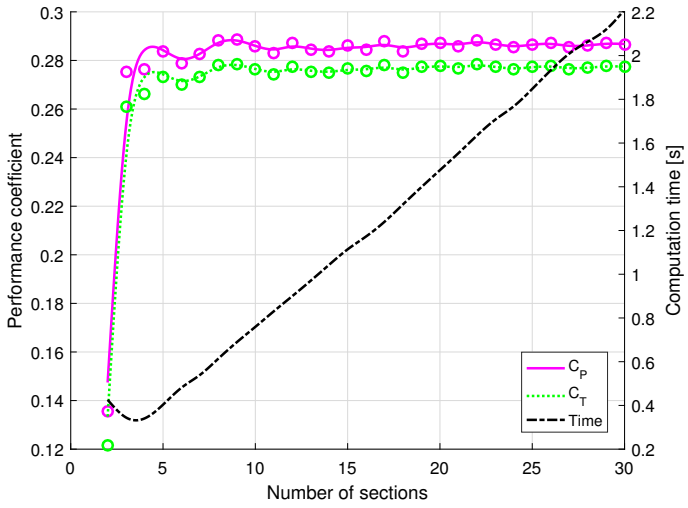

(b) Half cosine spacing of sections.

Figure 8.3: Influence of the number of sections on the performance coefficients, analysis point: scaled N250 propeller, $J = 0.7$, rpm=1200, $D_p = 3.93$m, NACA 4-series equivalent airfoils.

II

Results

9

Results of optimization strategies

A number of optimization routines are performed to assess the possible gains in performance of an optimized propeller and propulsive architecture for the selected aircraft and mission. Two reference cases are established for comparison to the optimization results. Different optimization algorithms are used in the experiments. For the gradient based optimization the 'SQP' algorithm in Matlab is used. This is a robust algorithm that can recover from unfeasible points. For the global optimization the 'GA' genetic algorithm of Matlab is used. GA can cope with unfeasible points and discrete non-integer variables (such as the number of propeller blades). The chapter is closed with a discussion on the optimization strategies. In this discussion the findings of the different strategies are compared. From this comparison a conclusion on the confidence of optimality of the different strategies is made.

9.1. Reference aircraft

The tools and optimization strategies of the previous part are used to determine the propellers influence on the ATR72-600 maximum take-off mass. In order to assess the improvements of the propeller design a reference case is established. As mentioned in the introduction, the conceptual design of turboprop aircraft rely on an assumption for the propulsive efficiency for sizing the propulsion of the aircraft. Torenbeek[2, p. 165] established these efficiencies as $\eta_p = 73\%$ for the critical climb condition and $\eta_p = 85\%$ in cruise. This estimation is used to determine a reference case for sizing the propulsive unit with handbook methods sizing the ATR72-600 with these assumptions for the propeller performance results in an aircraft of Table 9.1. In this table the key figures of the resulting aircraft are given. This case allows the validity of the assumptions for propeller performance as well as the improvements of an optimized propeller design to be evaluated.

Another method for sizing the propulsive unit in the conceptual design phase would be to use an existing propeller. This method is of higher fidelity. It relies on a calculation of propeller performance. An advantage of using an existing propeller to calculate the propulsive efficiencies for the sizing requirements is a more accurate prediction for a specific aircraft. The propulsive efficiency for the critical climb condition may vary between aircraft. For example due to a different thrust requirement or flight speed in the climb condition. A downside is that the propeller geometry must be supplied and this geometry may not represent an optimum. For the ATR72-600 the rpm and diameter are known, together with the geometry of a propeller, in this case the N250, the propulsive efficiencies are calculated. The resulting aircraft sized with the calculated efficiencies is given in Table 9.2.

9.2. Results of gradient based optimization

Experimentation performed with the gradient based algorithm resulted in significant insight in the applicability of gradient descent optimization for propeller design. In this section, the type of results that can be expected from this optimization strategy are discussed. In addition to this, the influence on optimality of some propeller parameters is determined. The optimization strategies established in Chapter 2 resulted in special cases for the aerodynamic model and the take-off field length.

Table 9.1: Reference Aircraft parameters sized with Torenbeek's assumption for propeller propulsive efficiencies.

Parameter/variable	Value
MTOM [kg]	22900
OEM [kg]	12700
Mass propulsive unit [kg]	919
Fuel mass [kg]	2690
Engine power P_{max} [kW]	2170
Cruise propulsive efficiency	0.850
Climb propulsive efficiency	0.730

Table 9.2: Reference Aircraft parameters sized with propeller propulsive efficiencies calculated from a scaled N250 propeller.

Parameter/variable	Value
MTOM [kg]	22900
OEM [kg]	12800
Mass propulsive unit [kg]	987
Fuel mass [kg]	2610
Engine power P_{max} [kW]	2190
Cruise propulsive efficiency	0.873
Climb propulsive efficiency	0.716
TOFL [m]	1150

In this section the influence of a detailed or simplified aerodynamic model in the optimization routine is described. The take-off field length result of each propeller design is found not to differ much between optimization cases. Therefore the take-off field length will not be set as a constraint. Rather only a TOFL analysis is performed after the propeller is designed. Finally the choice of the MTOM for a propeller design objective is discussed.

9.2.1. Influence of the starting point on design

Experimentation showed that the minimum found by a gradient descent optimization is very dependent on the initial design. Moderate improvements can be found when the N250 propeller is used as an initial condition. However a better strategy is defining the initial condition with a overly thin propeller blade. A thin blade has good aerodynamic properties but will not meet thrust and structural constraints. The optimization algorithm will follow a routine to satisfy constraints as well simultaneously assessing the optimality of the result. This will result in a more optimal design then supplying an actual propeller as initial condition but care has to be taken that a feasible initial design is supplied.

The optimization routine of a propeller optimization with a thin propeller blade as an initial design is investigated. The initial conditions and bounds can be found in Table 9.3. The airfoils were not included in the optimization routine. For this case a simplified aerodynamic model was used. Instead of optimizing the airfoil parameters, the airfoils of the N250 propeller were maintained. However the influence of the Reynolds number variation is included in the calculation of each function evaluation. The optimized blade geometry is given in Figure 9.1. The optimization routine results in a moderate improvement in the efficiencies in both cruise and climb. This results in almost unnoticeable changes in the key aircraft parameters. The mass of the overall aircraft hardly changes. The propeller parameters are given in Table 9.5 along with the resulting aircraft parameters in Table 9.4.

Table 9.3: Optimization conditions, showing the initial design and the constraints

	Initial design	Lower bound	Upper Bound
Chord vector $\left[\frac{r}{R}\right]$	[0.11 0.11 0.11 0.11 0.055]	[0.08 0.05 0.05 0.03 0.02]	[0.2 0.2 0.2 0.2 0.1]
β vector [deg]	[47.9 32.3 22.713 19.7 17]	[40 20 20 10 8]	[60 40 38 30 22]
Diameter [m]	3.93	3.5	4.5
Rpm	1200	1000	1400
β_p [deg]	2	0	10

Table 9.4: Resulting aircraft parameters from performed gradient descent optimizations for different objectives: MTOM & η_p.

	MTOM (Simplified aero-model)	MTOM (Detailed aero-model)	$\eta_{p,\text{cruise}}$	$\eta_{p,\text{climb}}$
MTOM [kg]	22900	22900	22900	22900
OEM [kg]	12800	12800	12800	12900
Propulsive unit mass [kg]	984	984	988	1000
Fuel mass [kg]	2580	2580	2540	2550
Engine power P_{max} [kW]	2150	2150	2100	2050
Take-off field length [m]	1150	1150	1160	1150

Table 9.5: Resulting propeller parameters from performed gradient descent optimizations for different objectives: MTOM & η_p.

	MTOM (Simplified aero-model)	MTOM (Detailed aero-model)	$\eta_{p,\text{cruise}}$	$\eta_{p,\text{climb}}$
Cruise propulsive efficiency	0.883	0.884	0.893	0.891
Climb propulsive efficiency	0.727	0.726	0.741	0.761
Rpm	1180	1190	1130	1050
Diameter [m]	4.01	4.00	4.17	4.50
Blade activity factor	76.9	76.8	62.6	68.2

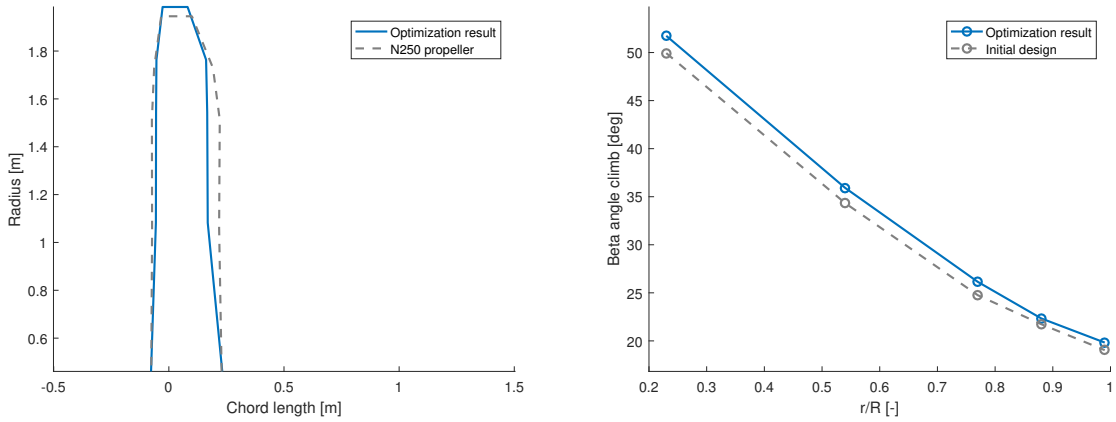

(a) Untwisted blade planform.

(b) β distribution.

Figure 9.1: Result of gradient descent optimization, blade geometry.

9.2.2. Optimization with detailed aerodynamic model

The results so far show that the improvements found in propeller performance have a marginal effect on the aircraft. In order to determine the effect of the airfoil choice on propeller design a new optimization procedure is started. The optimization case is the same as given in Table 9.3 with the addition of the airfoil thickness and camber in the design vector. For the initial design the airfoil distribution of the N250 is selected. The addition to the design vector is given in Table 9.6. The optimization routine resulted in a slightly modified thickness and camber distribution. The optimized propeller diameter does not differ significantly from the optimization routine with the fixed airfoil set, see Table 9.4 and 9.5. The optimized root section features a reduced camber and is slightly thicker. A reason for this could be to better cope with the structural stress and may allow more loading to be carried away from the root. However this is not checked and remains abductive reasoning. At higher radial locations the thickness is slightly decreased. It is probable that this is to improve transonic behaviour because supercritical technology factor in this research is set conservatively at $\kappa = 0.87$. Including the airfoil choice in the optimization routine does not produce significant improvements in propeller performance when compared to the case with a fixed set of airfoils. However, choosing to optimize the airfoils along with the propeller geometry greatly complicates the design space. Including the airfoils in the design vector increases its size and allows more local minima to exist. This means that finding a set of optimal airfoils is hindered by the optimization technique.

Table 9.6: Additional design variables of detailed aerodynamic model.

	Initial design	Lower bound	Upper Bound
Airfoil thickness %	[24 10 6.02 6.02 7]	[20 9 6.01 6.01 6.01]	[25.99 19 10 10 10]
Airfoil camber %	[1.5 4.5 4.98 4.5 3]	[0.01 0.01 0.01 0.01 0.01]	[4.99 4.99 4.99 4.99 4.99]

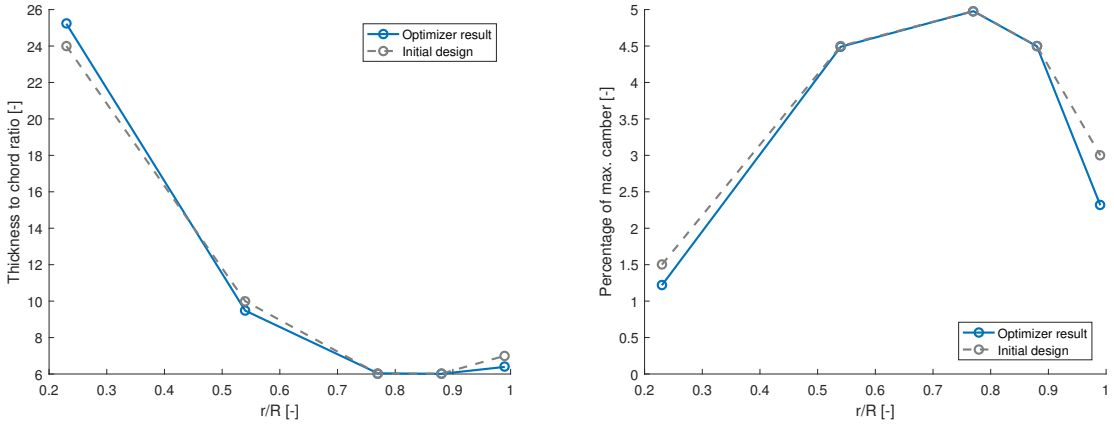

(a) Optimized thickness distribution.

(b) Optimized camber distribution.

Figure 9.2: Gradient decent optimization result with detailed aerodynamic model.

9.2.3. Optimizing for different design objectives

In this section the consequence of setting a different design objective is investigated by optimizing for a maximum propulsive efficiency instead of minimal aircraft MTOM.

Maximize cruise propulsive efficiency

Optimizing for maximum cruise efficiency results in the lowest MTOM by 30 kg compared to all cases discussed until now. The optimization case is the same as the case in Section 9.2.1 with the same initial conditions and bounds. However the optimization routine increased propeller diameter to 4.17m and this results in large propulsive efficiencies in both cruise and climb. The increased propulsive efficiencies results in a low fuel and engine mass. The increased mass of the propeller and gearbox due to the large diameter did not negate these gains. The resulting propeller is plotted in Figure 9.3.

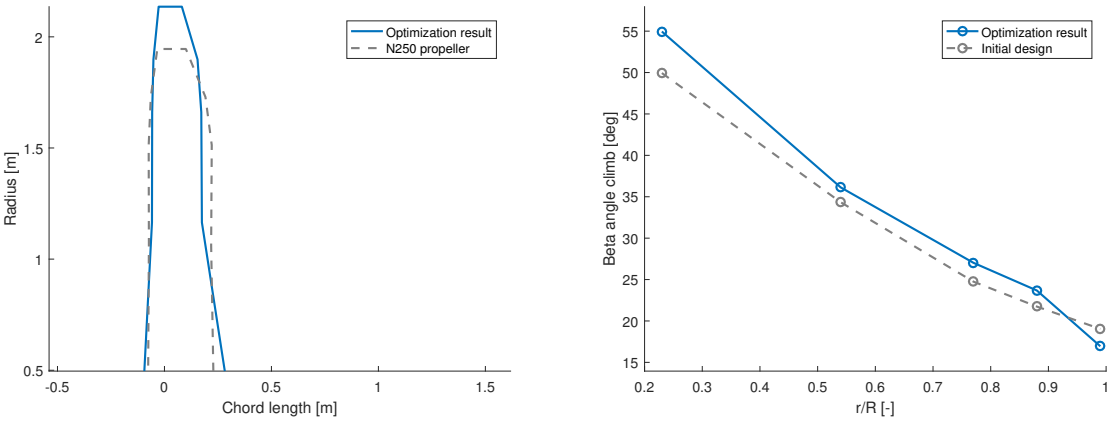

(a) Untwisted blade planform.

(b) β distribution.

Figure 9.3: Optimized blade geometry with cruise propulsive efficiency as objective.

Maximize climb propulsive efficiency

In case the climb propulsive efficiency is maximized a large aircraft MTOM results. The optimization routine results in a propeller which reaches the upper bound for propeller diameter at 4.5m. This increased the propulsive mass drastically with both a higher propeller and gearbox mass. The increased climb efficiency and thereby lowered engine mass is not able to offset this. The result is a high MTOM. The propeller geometry can be found in Figure 9.4. Note that the section pitch angles in climb are reduced, thereby increasing the lift over drag in the climb condition. The optimization results obtained until now all raised the climb pitch angle so the effective chord length could be reduced to allow an increase in the blade aspect ratio.

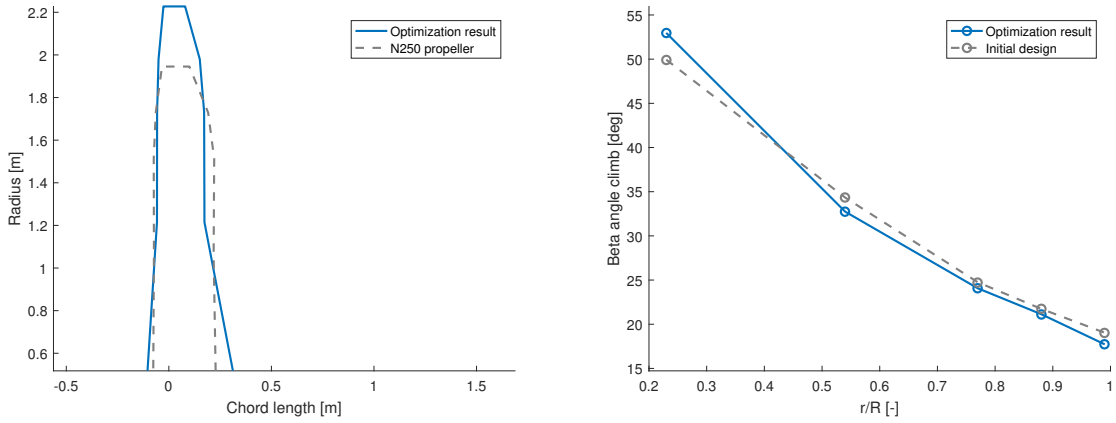

(a) Untwisted blade planform.

(b) β distribution.

Figure 9.4: Optimized blade geometry with climb propulsive efficiency as objective.

Discussion on changing the design objective

In this thesis an optimal propeller design is defined as a design which will result in a minimum aircraft MTOM. Yet optimizing for cruise propulsive efficiency results in a minimum MTOM. This is a puzzling result. In Chapter 2 a methodology is developed to arrive at a minimum MTOM. The objective of a minimum MTOM was thereby established as a function of cruise propulsive efficiency and the propulsive mass($f(\eta_{p,\text{climb}})$). This means that a point on the objective field can only be found if the BEM code converges for both flight segments. If one of the convergences fails no point on the objective field can be found. This makes the optimization procedure inherently more unstable then if the objective relies on only one convergence. In case the objective only depends on the cruise condition a failure of convergence in the climb condition means a constraint violation for the optimizer. The optimization algorithm is able to take this information into account when selecting its next step on the objective field. However in the case the objective is dependent on the convergence of both conditions a failure will result in rejection of that design. The optimization algorithm cannot determine its location on the objective and will therefor select a new design point thereby losing the optimization information. The more stable optimization procedure allows a better optimum to be found by the optimizer.

9.3. Results of genetic optimization

In Chapter 2 a genetic algorithm is selected to determine a global optimum for the propeller design. The Matlab user manual defines genetic optimization as: 'a method for solving both constrained and unconstrained optimization problems that is based on natural selection, the process that drives biological evolution. The genetic algorithm repeatedly modifies a population of individual solutions. At each step, the genetic algorithm selects individuals at random from the current population to be parents and uses them to produce the children for the next generation. Over successive generations, the population "evolves" toward an optimal solution.' The main advantages of using the genetic algorithm for propeller design are:

- Allows the number of blades to be part of design space.
- Is better equipped to handle large non linearity in the design space

- Unfeasible points and discontinuities in the design space can be better traversed
- Better change of finding the global optimum versus getting stuck in a local optimum

These advantages come at a cost of computational time. This is because the optimization method requires a very large number of function evaluations. To decrease the computation time, the simplified aerodynamic model is further simplified. The interpolation for the Reynolds number is removed to increase calculation speed. For the aerodynamic model one set of Reynolds numbers and airfoils is chosen. The Reynolds number chosen for each section is the average of the Reynolds number encountered during cruise and climb for the propeller designed with N250 airfoils given in Table 9.7. This results in a typical optimization time, depending on optimizer settings, of around 30 minutes.

Table 9.7: Airfoil and Reynolds number set over the blade span for genetic optimization.

Airfoil radial location (r/R)	Reynolds nr.	Airfoil NACA nr.
0.23	1.6×10^6	2424
0.54	2.4×10^6	5410
0.77	2.4×10^6	5406
0.88	1.7×10^6	5406
0.99	1.0×10^6	3407

A genetic optimization provides no guarantee that a global optimum is reached. The optimization routine contains randomness, both in generation of the initial population as the the following generations. The initial population in this thesis is generated using latin hypercube design. A population of 300 individuals is established and an optimum is reached in around 250 generations.

In this section two optimizations are performed. With the objective set as a minimum MTOM, both obtained a better optima then found with the gradient descent optimization. However the absolute improvement in MTOM remains marginal.

9.3.1. Optimization with large diameter

The initial genetic optimization was performed with the same conditions as given in Table 9.3 with the an additional variable for the number of blades (Table 9.8). The upper and lower bound for the number of blades follow from the establishment of the mass estimation of the propeller in Section 7.4. Additionally a constraint is added for the blade activity factor:

$$g_{\text{add}}(\overline{x}) = 1 - \frac{AF(\overline{x})}{65} \leq 0 \tag{9.1}$$

This is done to ensure a realistic blade design. If the blade activity factor is allowed to become to small a structurally questionable design may result. The blade activity factor AF is determined by the following integral:

$$AF = \frac{10^5}{D_p^5} \int_{r_{hub}}^{R} \frac{c}{D_p} \left(\frac{r}{R}\right)^3 d\left(\frac{r}{R}\right) \tag{9.2}$$

The result of the global optimization is given in Figure 9.5 and Table 9.9 & 9.10. The design optimization results in a 4 bladed propeller. The decreased number of blades result in a lower MTOM by trading aerodynamic efficiency for a decreased propeller mass. However the aerodynamic efficiency is not severely decreased as the large diameter allows the blades to have a significant aspect ratio. If a large diameter is not allowed by, for instance, by constraints in ground clearance, it is expected that the optimal blade number will change.

Table 9.8: Additional design variable for the number of blades, allowed by genetic optimization.

	Initial design	Lower bound	Upper Bound
Number of blades	6	3	6

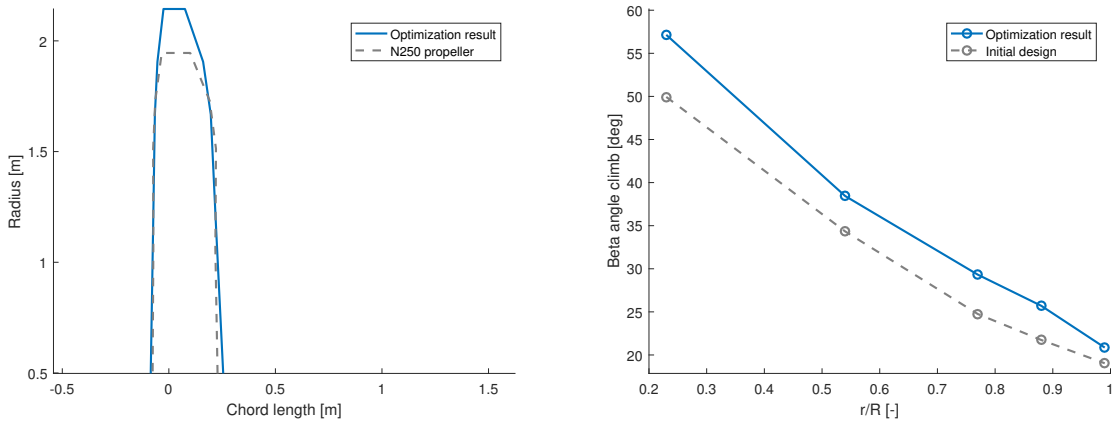

(a) Untwisted blade planform.

(b) β distribution.

Figure 9.5: Global optimization result for unconstrained diameter - propeller geometry.

Table 9.9: Global optimization result for unconstrained diameter - aircraft parameters.

Main aircraft parameters	
MTOM [kg]	22900
OEM [kg]	12800
Mass propulsive unit [kg]	980
Fuel mass [kg]	2580
Engine power P_{max} [kW]	2110
TOFL [m]	1140

Table 9.10: Global optimization result for unconstrained diameter - propeller parameters.

Propeller parameters	
Cruise propulsive efficiency	0.882
Climb propulsive efficiency	0.732
Rpm	1107
Diameter [m]	4.33
Number of blades	4
Blade activity factor	79.3

9.3.2. Optimization with a diameter constraint

In the previous section the optimum propeller design resulting in a minimum MTOM featured 4 blades. This optimum did not encounter a constraint for the propeller diameter. This may not resemble real world design conditions as the aircraft geometry may impose a constraint on propeller diameter. In this section such a constraint is added and the resulting propeller optimum is evaluated. The optimization case of the previous section is altered by setting the maximum propeller diameter to that of the ATR72-600 shown in Table 9.11.

Table 9.11: Diameter design constraint.

	Initial design	Lower bound	Upper Bound
Diameter [m]	3.9	3.5	3.93

As expected the number of blades is increased. It is found that the AF remains similar between the two cases. The diameter limits the aspect ratio and it becomes favourable to add another blade. In Section 10.1 a more detailed discussion on the influence of propeller parameters on the optimum is performed. A more in depth discussion on the interaction between the number of blades, the diameter and aspect ratio will follow there.

9.4. Discussion on optimization techniques

In this section the different optimization techniques are evaluated. The results of the gradient optimizations is compared to the results of the genetic optimization. It must be noted that the global optimization uses a different aerodynamic model by excluding the Reynolds number influence. The results are therefore not fully comparable.

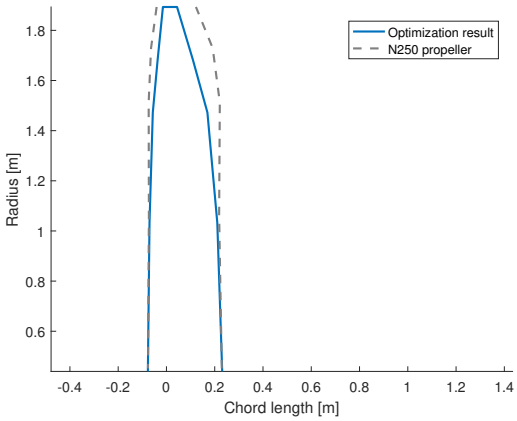

(a) Untwisted blade planform.

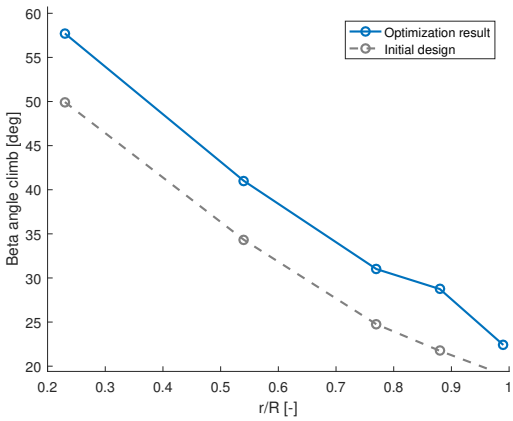

(b) β distribution.

Figure 9.6: Global optimization result for constrained diameter - propeller geometry.

Table 9.12: Global optimization result for constrained diameter - aircraft parameters.

Main aircraft parameters	
MTOM [kg]	22900
OEM [kg]	12800
Mass propulsive unit [kg]	969
Fuel mass [kg]	2600
Engine power P_{max} [kW]	2200
TOFL [m]	1140

Table 9.13: Global optimization result for constrained diameter - propeller parameters.

Propeller parameters	
Cruise propulsive efficiency	0.876
Climb propulsive efficiency	0.700
Rpm	1258
Diameter [m]	3.82
Number of blades	5
Blade activity factor	72.2

9.4.1. Comparison of optimization results

The optimization strategies result in different optima, the global optimization determines a minimum with a low propulsive mass with detrimental effects to the fuel mass. Local optimization - which is not able to alter the blade number - optimizes aerodynamic efficiency resulting in low fuel mass but at a cost to the propulsive mass. The optimization results are given in Table 9.14. In Table 9.15 the relative difference in optimization time is given. This time comparison is relative, absolute times are dependent on optimizer settings and initial conditions. The results show a marginal decrease in MTOM for both optimization techniques when compared to the reference case.

Table 9.14: Optimization results of different optimization techniques with minimum aircraft MTOM as objective.

	Gradient descent optimization	Genetic optimization	Non optimized N250 reference
MTOM [kg]	22890	22880	22940
Propulsive unit mass [kg]:	984	969	987
Fuel mass [kg]	2580	2600	2610

9.4.2. Exploration of propeller design space

The difference between the result of the genetic and gradient based algorithms is due to the gradient descent optimization evaluating a very limited portion of the design space. In Figure 9.7 the gradient descent optimizations performed discussed in the beginning of this chapter are displayed. For this figure the design objective established in Chapter 2 is used to indicate the MTOM of the aircraft. On top of that surface the evaluated designs are plotted. It shows that, when optimizing for aircraft MTOM, an even smaller portion of the design space is evaluated then for the other objectives. Optimizing for either propulsive efficiency allows the optimizer to evaluate a larger portion of the design space. Setting the objective for minimum MTOM prohibits the optimization routine to 'backtrack' on itself and thereby finding a better solution. It is easy for this

Table 9.15: Optimization times of the different optimization cases.

Optimization time	
Gradient descent simplified aero-model	30 s
Gradient descent detailed aero-model	90 s
Global optimization	30 min

optimization to get stuck in a local minimum.

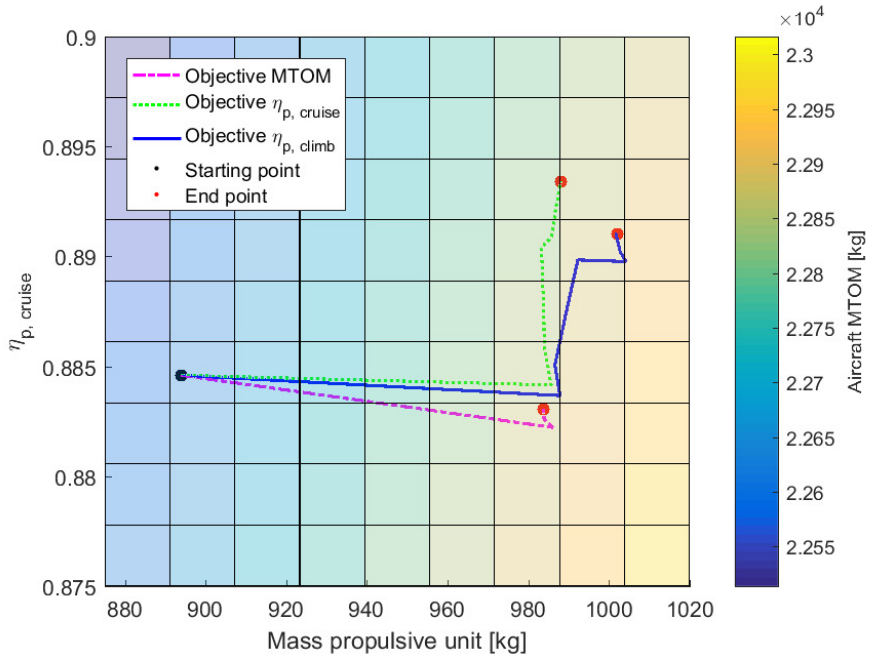

Figure 9.7: Optimization paths of gradient descent optimizations.

The genetic algorithm performs a thorough sampling of propeller designs over the design space. In Figure 9.8 each evaluated propeller design is marked with a dot. Two trends can be found in this figure, these have been indicated by the white lines. The dashed line shows the trend of minimum propulsive mass required to obtain the climb thrust requirement. The top line shows the limitation for cruise propulsive efficiency that can be found. The maximum cruise efficiency that can be found increases with a decreasing propulsive mass. This is a counter intuitive result because a high cruise efficiency generally requires a propeller with large diameter and number of blades and is subsequently heavy. The reason the cruise efficiency grows with decreasing propulsive mass is the following: A high cruise efficiency is obtained with a low loading on the propeller. This means a low power consumption by the propeller. This low power requirement means a light engine, light nacelle as it is scaled by the engine size and even the propeller mass estimation implemented determines propeller mass as a function of power. This means that as cruise efficiency increases the propulsive mass decreases up to the the climb thrust constraint. If the slope of both lines is studied it follows that the optimal propeller design resulting in minimal MTOM can be found at the intersection of the two lines. From this graph it can be concluded that optimizing for maximum cruise efficiency results in minimum MTOM.

However this conclusion is presumptuous. Plotted in Figure 9.9 is the result of a global optimization with maximum cruise efficiency as objective. In this figure it can be seen that optimizing for maximum cruise efficiency will not result in an aircraft with the lowest MTOM. Optimal cruise efficiency is possible in an aircraft configuration of higher mass. What this means is that the propeller performing optimally in cruise is not propelling an aircraft with minimum MTOM. However an aircraft with minimum MTOM requires the min-

Table 9.16: Individual with minimum MTOM, satisfying all constraints, selected from an optimization with $\eta_{p,\text{cruise}}$ objective

Minimum MTOM, $\eta_{p,\text{cruise}}$ as objective	
MTOM [kg]	22860
Propulsive unit mass [kg]	988
Fuel mass [kg]	2550

imal cruise thrust to fly(see Figure 2.5b). The lower the trust required by the propeller means the propeller operates on a lower loading, and generally, this is beneficial for the performance. What Figure 9.9 shows is that a propeller can have a better propulsive efficiency, even though it has to produce more thrust, by having a heavier but more aerodynamically favourable design.

Again it is found that on optimization with the objective set for optimal cruise efficiency, is better equipped to find propeller designs at the threshold of cruise efficiency. The procedure established in the methodology is not well suited for exploring the entire design space of propeller design. The design resulting from Figure 9.9 with the maximum cruise efficiency does not result in a minimum MTOM. If however, the individual with the lowest MTOM is selected from this population the best result until now is found(Table 9.16). This result has a high propulsive mass and a very low fuel mass as can be expected from the optimization routine. The designs considered in the optimization have a good spread near optimal cruise efficiency and lightest propulsive design for optimal cruise efficiency. This is concluded from the clear cross of constraint violating designs and satisfying designs in this area. The optimal cruise efficiency with lightest propulsive unit mass is quite certainly reached as moving further to the right of this point results in climb thrust violations with a good density in designs considered. Moving to the top from this cross there is a good density of designs with a cruise thrust violation. Towards the top left corner again a good density of considered designs that do not meet constraints. However the density of designs considered with sub-optimal cruise efficiency but a light propulsive unit is poor. This prohibits the conclusion that optimizing for optimal cruise performance will allow a design resulting in minimum MTOM to be found.

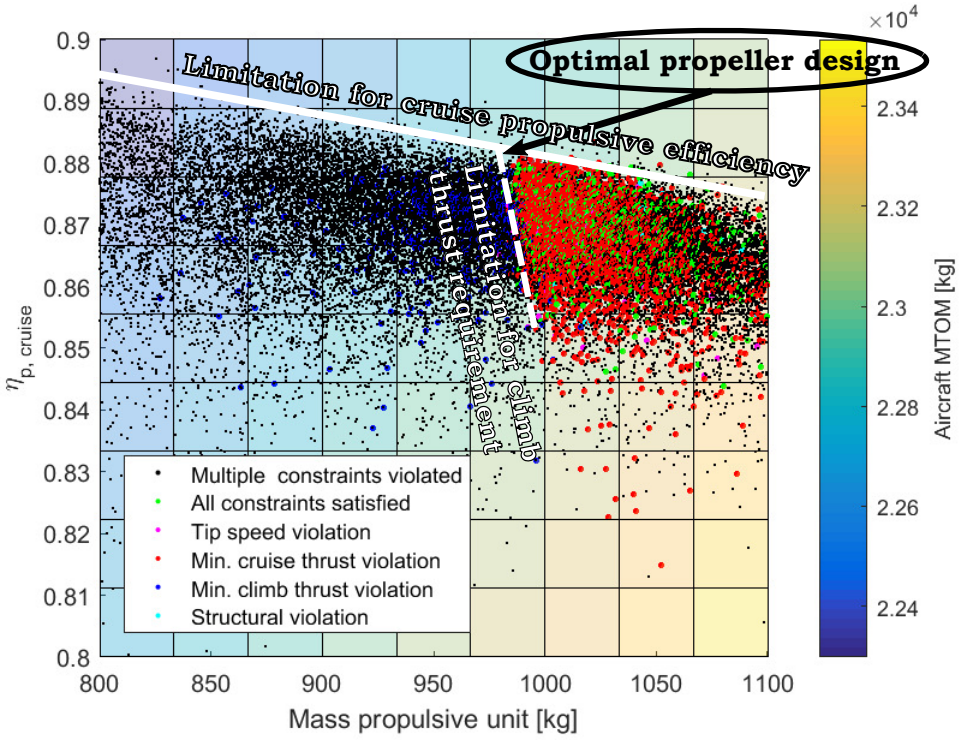

Figure 9.8: Global optimization result with minimum MTOM as objective.

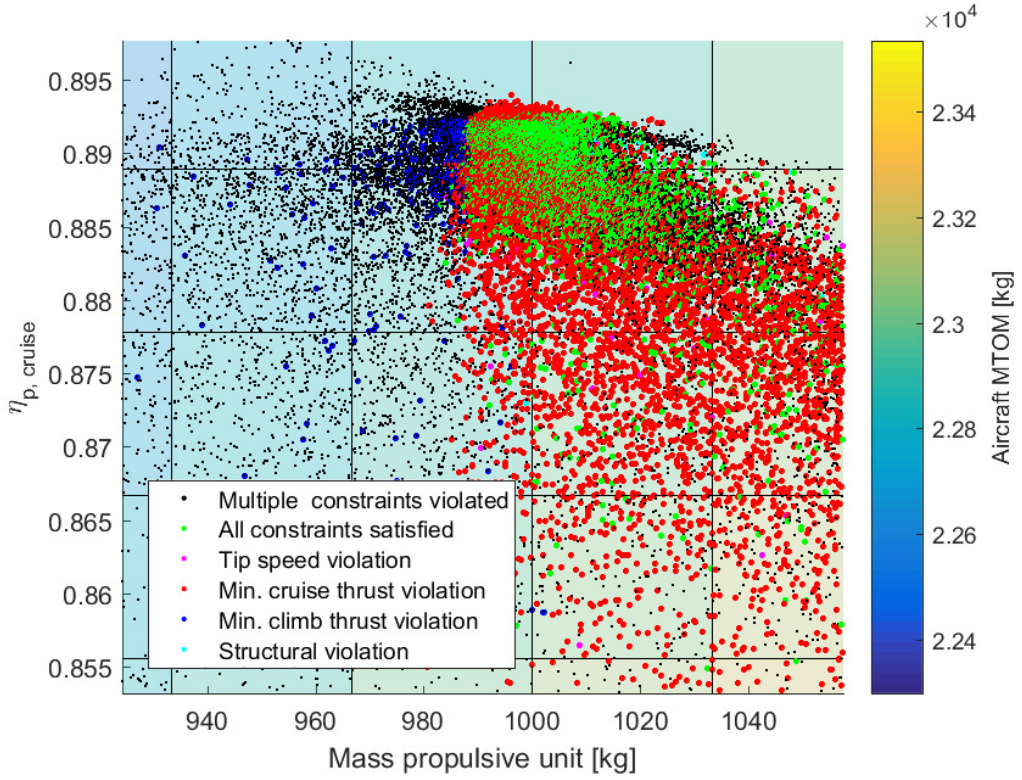

Figure 9.9: Global optimization result with maximum $\eta_{p,\,\text{cruise}}$ as objective.

10

Dependence of variables

In the previous chapter different optimization strategies were used to determine an optimal propeller design. The influence of different propeller parameters is determined in this chapter. This is done by keeping parameters of interest constant while performing a gradient descent optimization. Propeller parameters are investigated in the first section, the influence of the take-off field length in the second section.

10.1. Dependence of propeller parameters

This section investigates the influence of propeller parameters. Three parameters are varied: The Activity Factor AF, the Diameter D_p and the number of Blades B. For these variables a gradient descent optimization is performed for a minimum MTOM. For the initial point of the optimization the values of Table 9.3 are used. The airfoils of the N250 were maintained throughout the optimization.

10.1.1. Blade activity factor

The blade activity is a non-dimensional measure of a propeller's power absorbing capacity. It is influenced by the ratio of blade area in the propeller disk and the radial distance this from the hub. The Blade Activity Factor[2] AF is determined by the following integral:

$$AF = \frac{10^5}{D_p^5} \int_{r_{hub}}^{R} \frac{c}{D_p} \left(\frac{r}{R}\right)^3 d\left(\frac{r}{R}\right) \tag{10.1}$$

The blade activity factor is mostly influenced by the radial location of the chord. This is because the increased dynamic pressure towards the tip allows more power to be absorbed there. The total activity factor is the blade activity factor multiplied with the number of blades on the propeller.

The diameter is maintained at $D_p = 3.93$m to determine the effect of the AF. This is done to prevent the optimization routine from increasing the diameter to absorb the required power. By setting the diameter of the propeller at 3.93 m only the results that occur due to a changed planform are evaluated.

In Figure 10.1 the dependence between the activity factor and the propulsive efficiency is plotted. As AF increases the efficiency drops. This is due to the increased loading towards the tip and an effective decrease in blade aspect ratio. In the same Figure it can be seen that increasing the blade number for the same total activity factor increases propulsive efficiency. Particularly in climb, a high loading condition, adding a blade is beneficial to propulsive efficiency. This is because of the increase in aspect ratio that occurs when a blade number is increased for the same total activity factor[75]. Weick states that an increase of the blade chord equals an increase in the slipstream velocity, which is detrimental to propulsive efficiency.[76]. The rotational rate drops with the activity factor even though the diameter is kept constant. This means that the tip speed is decreased. Less dynamic pressure is required for the same thrust due to the chord increase. However, due to the increase in gearbox mass this is unfavorable. A lighter solution is a decrease of the pitch angle of the propeller in climb. In this case it is decreased by 2.1 degrees.

10.1.2. Number of blades

The number of blades has a significant influence on the efficiency and weight of the propeller. According to the chosen propeller mass estimation method, the number of blades increase the mass of the propeller by a

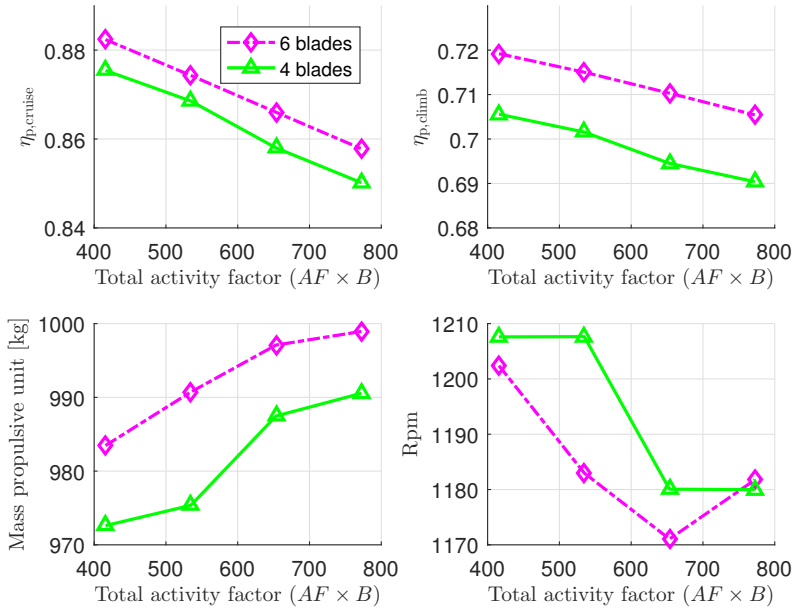

Figure 10.1: Propeller performance for different total activity factor, propeller diameter maintained at 3.93 m.

factor of $\sqrt{B}$. The aerodynamic efficiency is impacted in a number of ways. First, the addition of a blade will mean an additional source of 3D losses at the tip. However, this loss is offset by the reduced loading on the blades. Adding a blade means that each blade has to absorb less power and can therefore reduce its chord length. This results in an effective increase in blade aspect ratio.

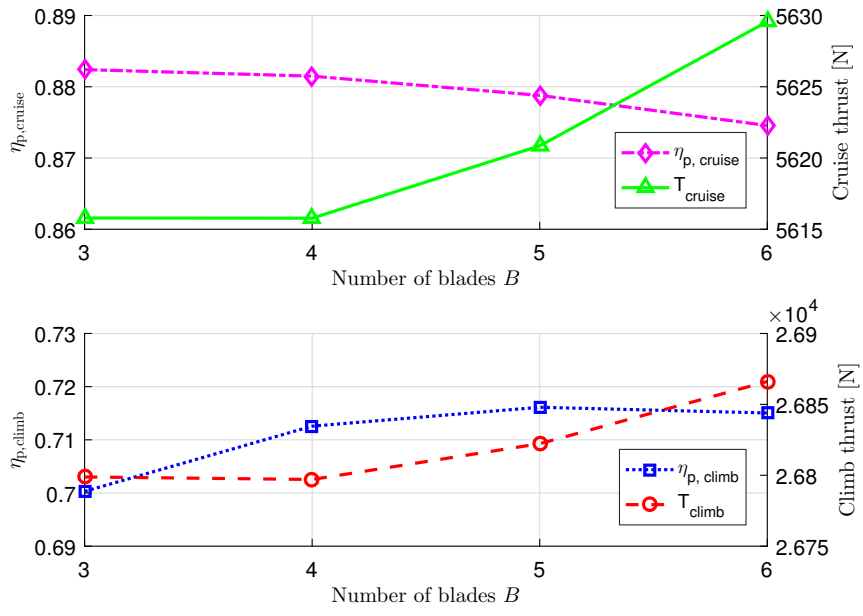

Figure 10.2: Propulsive efficiency and delivered thrust as a function of the number of blades.

Figure 10.2 shows that for an equal thrust, in the case of 3 and 4 blades, the addition of a blade will yield an increase in propulsive efficiency. The addition of a blade is most effective for improving the high loading climb condition. However, the improvement in $\eta_{p,\text{climb}}$, which will result in a lower gas turbine mass, will be

offset by the increased propeller mass.

In this optimization case, 3/4 blades represents an optimum. In the case of 4 blades the reduction in gas turbine mass is sufficient to counter the increase in propeller mass due to an extra blade. This conclusion can be drawn from Figure 10.3.

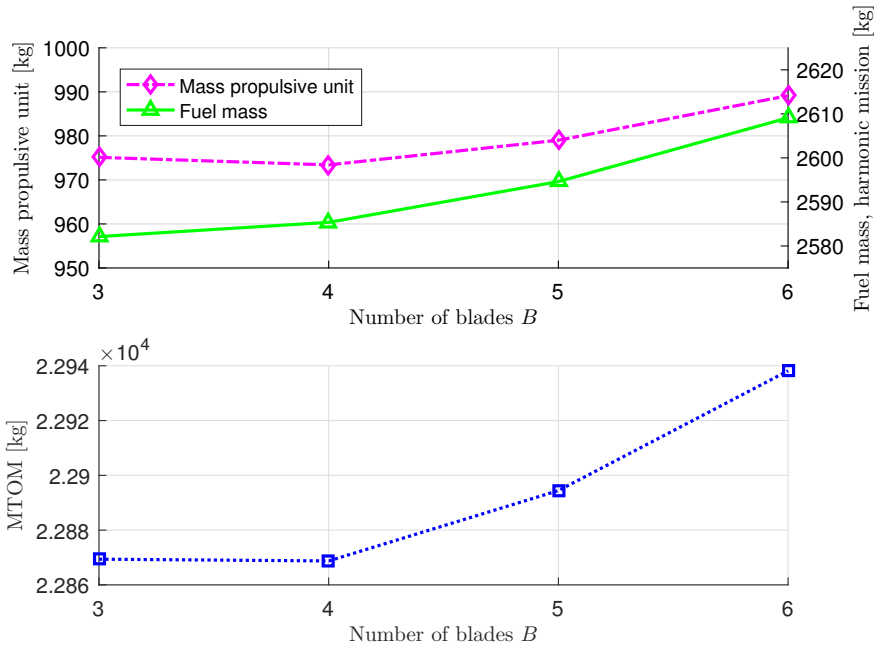

Figure 10.3: Mass of the propulsive unit, fuel and aircraft as a function of the number of blades.

The influence of the blade diameter and the activity factor are shown in Figure 10.4. The propeller diameter decreases with the addition of a blade. A diameter increase allows the increase of the blade aspect ratio. This means that if the diameter is constraint due to the geometry of the aircraft, a propeller with more blades may be beneficial.

10.1.3. Propeller diameter

The propeller diameter is an important constraint in propeller design. Often increasing the propeller diameter is beneficial as it increases the aerodynamic efficiency due to the increase in aspect ratio of the blades (Figure 10.5). However an increase in diameter is detrimental to the mass of the propulsion unit. The mass of the propeller grows with the diameter(Figure 10.6). Furthermore, the tip speed constraint ($M = 0.8$) dictates that the rotational rate of the propeller must decrease as the diameter grows. This requires an increase in gear ratio which increases gearbox mass. Summarizing, a larger diameter increases propulsive efficiency with a detrimental effect to the mass of the propulsive unit. The minimum MTOM is reached for a diameter where these conflicting effects meet, in this case between 3.5 and 4 meter, see Figure 10.7.

10.2. Take-off field length sensitivity study

In Chapter 5 the take-off field length of the ATR72-600 with reference propulsion architecture ($P_{max} = 2050$ kW) and a scaled N250 propeller is established as 1240 m. In Chapter 9.1 a reference case is re-established that meets the thrust requirements itemized in Section 2.1.2. The obtained TOFL for this reference case is 1150 m.

Optimization of the propeller in previous sections shows that the margin for a reduction in take-off mass by optimization of the propeller design is quite slim. In addition, it is found the the take-off field length of the aircraft does not change significantly between designs and remains around 1150 m. In this section the take-off field length requirement is varied. A local optimization is performed to determine an optimum propeller that satisfies the imposed TOFL constraint. In order to asses the propeller and propulsion architectures at TOFL larger then 1150 m, the climb gradient constraint active in previous sections is lifted for this analysis.

Varying the TOFL requirement has a large effect on the engine power of the aircraft. Figure 10.8 shows a

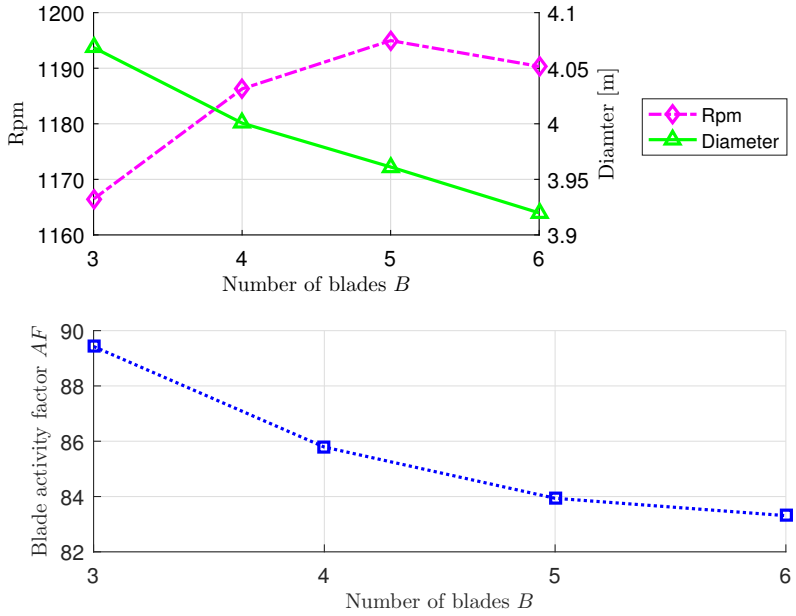

Figure 10.4: Above, the influence of the number of blades on the rotational rate and diameter. Below, the influence on blade activity factor is plotted.

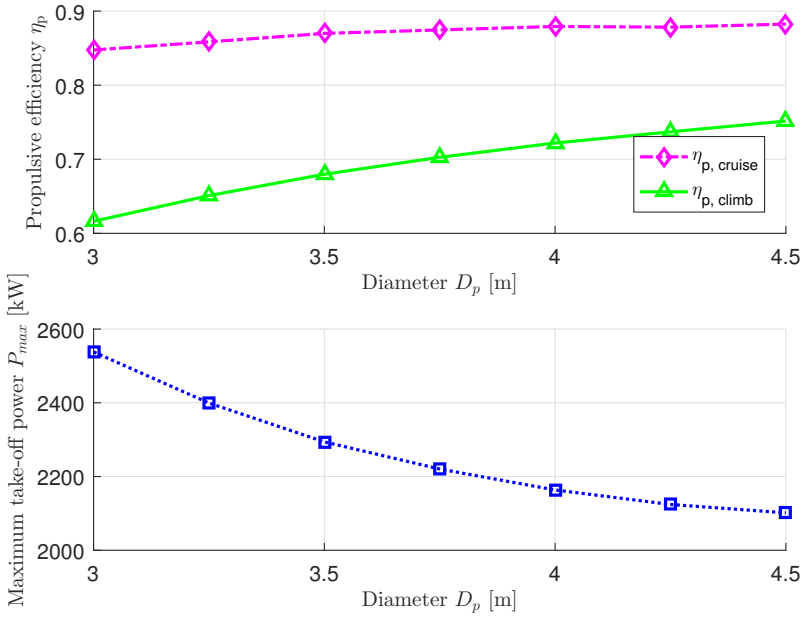

Figure 10.5: Propulsive efficiency and generated power as a function of diameter, 6 propeller blades

linear relation between the engine power and the set TOFL constraint. The take-off power is the dominant factor in obtaining the required TOFL. The influence of the propeller is minimal. The same figure shows that the propulsive efficiency for cruise hardly changes. A moderate improvement in the propulsive efficiency during the take-off is found. This can be attributed to the lower loading on the propeller as the TOFL increases. As the TOFL decreases and the the thrust requirement of the propeller grows, the increased loading deteriorates efficiency. To absorb an increase in power the diameter grows and the AF increases, as shown in Figure 10.9.

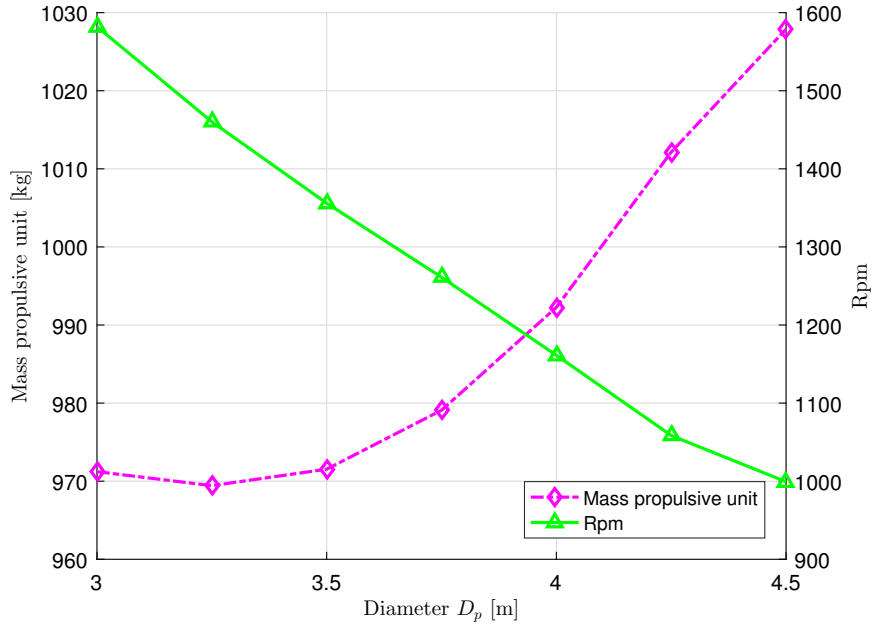

Figure 10.6: Influence of rotational rate on the propulsive mass as a function of diameter, 6 propeller blades.

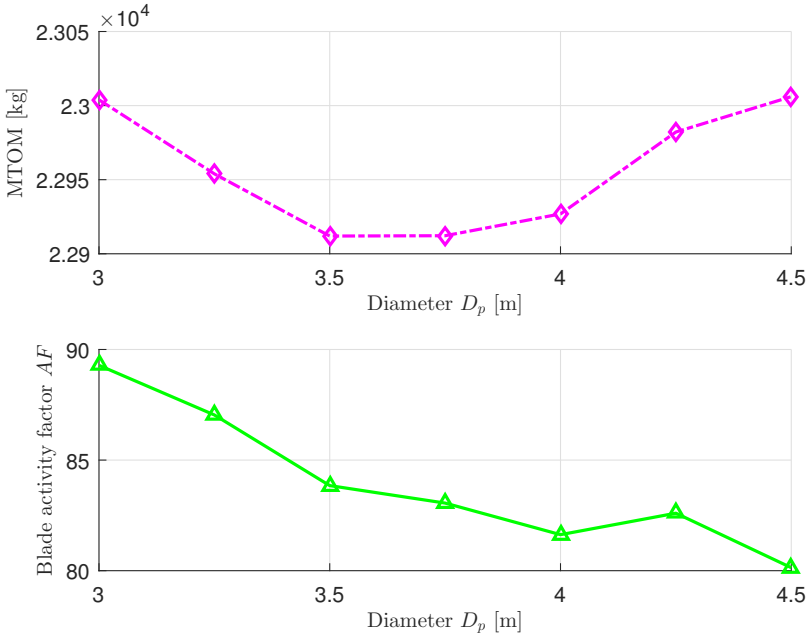

Figure 10.7: MTOM of the aircraft and blade activity factor as a function of the blade diameter, 6 propeller blades.

Over the analyzed range of TOFL, from 1075 m to 1225 m, the maximum take-off mass of the aircraft is reduced by 250 kg, an approximate 1% reduction. This is due to the decrease in mass of the propulsive unit mass by 100 kg (10%). Figure 10.10 shows the key masses of the aircraft. The fuel mass of the aircraft hardly changes as the MTOM decreases. The propulsive efficiency in cruise does not change significantly between cases. However, if the Breguet range equation (Equation (2.2)) is evaluated, it is found that a 1% reduction in MTOM should yield a 1% reduction in fuel mass. The reason the fuel mass in not reduced by this amount is a decrease in lift over drag as the aircraft becomes lighter. This decrease negates the expected fuel mass decrease.

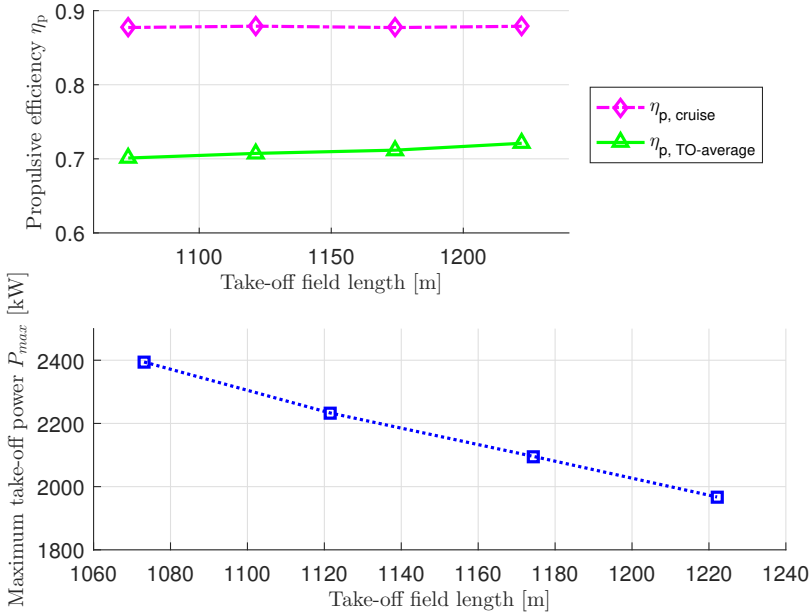

Figure 10.8: Influence of the take-off field length requirement with, on top: Propulsive efficiency in cruise and the average and take-off propulsive efficiency calculated at $V_{\text{TO-average}} = V_2/\sqrt{2}$. Below: Maximum take-off power requirement. Constant: 6 propeller blades.

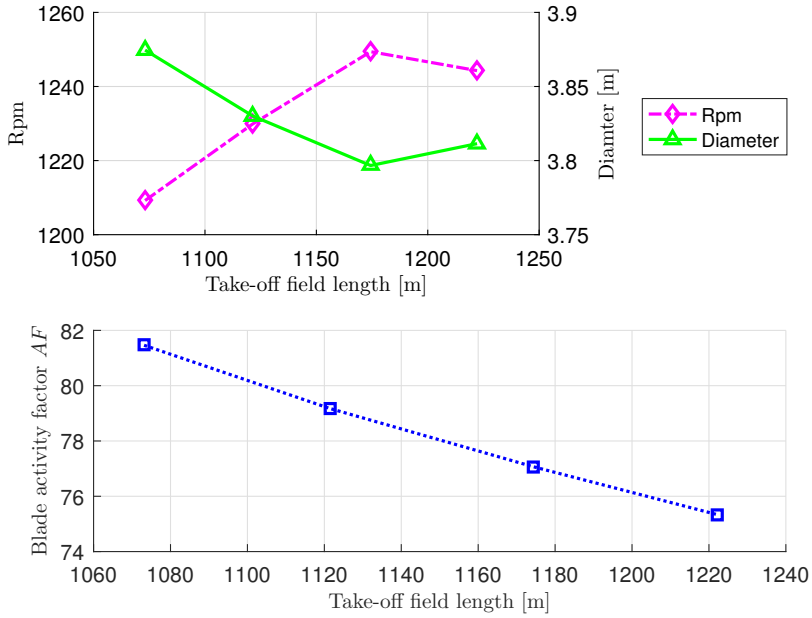

Figure 10.9: Influence of the take-off field length requirement on propeller, on top: Propeller rpm and diameter. Below: Blade activity factor. Constant: 6 propeller blades.

The optimization performed in this section showed that the take-off power, propulsive mass and MTOM varied linearly and proportional to one another. The take-off power is the dominant factor on the optimized MTOM.

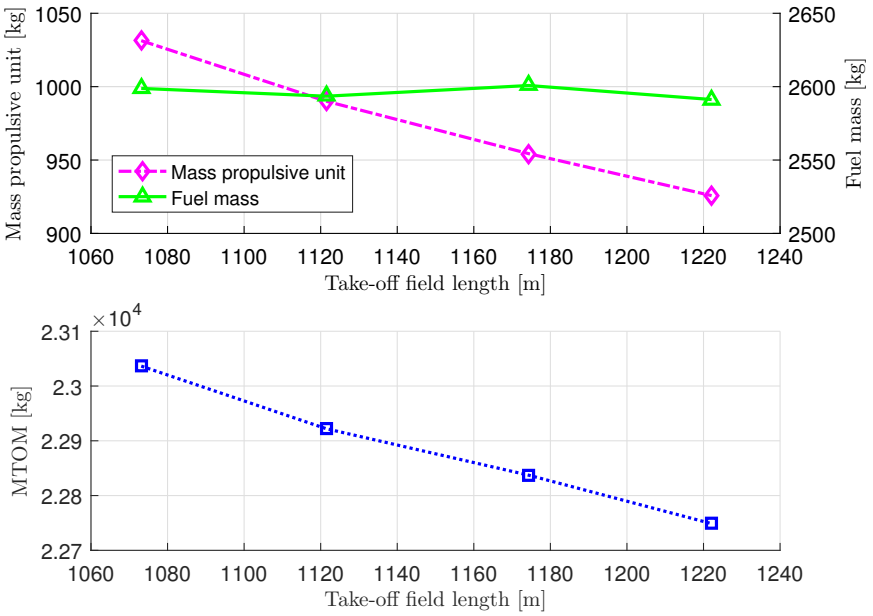

Figure 10.10: Influence of the take-off field length requirement on aircraft mass. Constant: 6 propeller blades.

11

Discussion on the results, accuracy of the tools and applicability of the research

The accuracy of the tools and objective are summarized in this chapter. The applicability of this research is then assessed. A discussion follows that places this work into a broader context. It aims to answer how the work performed in this thesis can be expanded upon and what applications it can serve.

11.1. Accuracy of the tools

Design objective

The design objective (Figure 2.4) shows the influence of the propulsive unit on the aircraft's MTOM. Comparing performance under- and overestimations a difference in MTOM of about 1000 kg is found. This is between a worst case scenario $W_{\text{propulsive}} = 1100$ & $\eta_{p,\text{cruise}} = 0.8$ and a best case scenario $W_{\text{propulsive}} = 900$ and $\eta_{p,\text{cruise}} = 0.9$. If the aircraft designer selects a reference propeller design or follows Torenbeek's assumptions for propeller design a very good first approximation of the propeller performance can be made. By selecting a good initial design the margin for improvement is drastically reduced to around 100-150 kg. This means that choosing the MTOM as a propeller design objective may not be suitable for the optimization. By selecting the MTOM the designer is looking for improvements of less then 1%.

By using the Initiator to establish the optimization objective some neglections in the objective are present. The propulsive mass and fuel mass are varied by changing the propulsive efficiency of the propeller. For a detailed explanation see Chapter 2. This method of establishing the objective neglects how the propulsive mass is distributed i.e. which percentage is propeller mass or nacelle mass etc. Thereby the influence of the propeller geometry on the aircraft is neglected. Among other effects, the propeller geometry and placement on the wing has an influence on sizing the control surfaces and thereby their mass. Turboprop design in the Initiator is not developed far enough for these effects to be included. However as the margins for improvement in MTOM are so small, these effects are significant.

Aerodynamic tool

The aerodynamic analysis of the propeller is performed for an isolated propeller. The installation effects of the propeller are not taken into account. The efficiencies obtained trough optimization are therefore not a true representation of the propeller on the aircraft and the calculated performance will not be met.

In Chapter 8 the influence of the number of blade sections used to define a propeller blade is described. The chosen number of blade sections is expected to present an underestimation in propeller performance of around 2%. This is a significant error margin.

Structure & mass

The structure module is used only to calculate the root normal stress. This stress is calculated from the forces of thrust and torque. The neglections of the structure tool can be found in Section 6.4.2. The consequence of having a very limited structural analysis is that a design might not be able to cope with the forces of flight. Meaning, a geometry is found which is unable to be designed from a structural perspective. The aerodynamic

performance of such a design cannot be achieved. A propeller with small chord lengths along the radius typically has good aerodynamic but poor structural properties. Neglecting if it is possible to design the structure for such blade, it is certain the structure would become heavier compared to typical designs. In this thesis, mass estimation of the propeller relies on a regression line established from reference propellers. This means that the mass estimation module is not suited for estimating the mass of novel designs. Propeller designs with small chord lengths or thin airfoils will be underestimated in mass. The error resulting from an under estimation of propeller mass of designs with small chords lengths is unknown.

Optimization

In Chapter 9 the complexity of the propeller design space is shown. The design space features a lot of local minima. Furthermore, the number of blades can only be defined as an integer number. A global optimization strategy is therefore needed if a full optimization for the main propeller parameters is to be performed. This requires a simplification of the aerodynamic model. The inaccuracies that result from this have not been established.

11.2. Relevance of this thesis

This thesis shows the implication of propeller design choices on the aircraft MTOM. The influence of the main propeller parameters is clearly described. A description of the propeller design space shows the challenges of propeller optimization. Thereby it provides information on how future optimizations of propellers can be better set-up. However, the optimization routines show that including the propeller design at the conceptual level does not produce significant changes to the design of the aircraft. The applicability to conceptual design is limited for this reason. Lower fidelity design is perhaps just as useful in the conceptual design phase.

This work can serve as a conceptual design suite for propellers. A lower fidelity propeller design method recommended in the previous paragraph is hindered by a lack of basic propeller sizing rules. The literature study[14] preceding this thesis, showed for instance, that scaling rules for the diameter of a propeller are reliant on the power absorbed by the propeller and rotational rate of the engine. However, this research showed that the diameter is a design freedom that is not dependent on these two variables alone. The diameter can be chosen by the designer with implications on other propeller design aspects.

Top-level parameters like diameter and number of blades are of interest for a conceptual designer. It may be possible to develop a set of low fidelity design rules from this thesis work. By first improving the accuracy of the tools to arrive at a medium fidelity propeller design suite. Then by performing a range of analyses on different turboprop types, a set of low fidelity design rules may be developed.

Incorporation of this work in the Initiator

The propeller designed by the methodology of this thesis is an optimal propeller for turboprop aircraft. To obtain this optimum a design routine separate from the Initiator design convergence loop is preformed. It is beneficial to users of the Initiator to be able to design an aircraft and propeller at once, without first establishing the influence of the propeller on the aircraft. This requires that this tool be incorporated within the design convergence of the initiator. This presents a problem which is addressed in this section.

The propeller design module can be incorporated within the wing power loading module. At that point in the design convergence loop the thrust requirements of the aircraft are known. These thrust requirements result from data of the previous iteration. This means that feedback on how the propeller and engine influence the aircraft design is lacking. Thus, the problem lies with the objective that drives propeller design. An objective must be established such that a balance between propulsive efficiency and propulsive mass is found.

Although it is concluded in Chapter 9 that optimizing for optimal cruise propulsive efficiency will deliver a good propeller design. Implementing this work in the Initiator with the cruise efficiency as objective will not work. It might be imagined that if cruise efficiency is selected as design objective no information on the aircraft mass is needed. This is not the case and reason for this is as follows. For sake of simplicity imagine optimal cruise efficiency dependent on two factors, the cruise thrust requirement and the geometry of the propeller. Optimizing the propeller for cruise means lowering the cruise thrust requirement and/or, adjusting the blade geometry to increase blade aspect ratio. Both adjustments will decrease the loading on the blade and increase propulsive efficiency. Decreasing the cruise thrust requirement requires decreasing the drag of the aircraft, which can be accomplished by lowering the MTOM.

Increasing the effective blade aspect ratio of the propeller can be accomplished by increasing the diameter of the propeller or adding a blade. This in turn increases the mass of the propeller. By now the conflict that arises from the structure of the Initiator has become apparent: If cruise efficiency is selected as objective, the optimization routine will increase the mass of the propeller. This means that the MTOM of the aircraft grows. The next iteration the cruise thrust requirement has grown under the increased MTOM. The propeller optimization will then further increase the mass of the propeller. This is because the increase in cruise thrust means an increase in loading unless, a blade is added or the diameter is increased. Implementing the propeller design tool in this way in the Initiator, will result in a design spiral that reaches the upper bounds of the propeller design geometry.

Concluding the propeller design tool of this thesis can be implemented if the information that contains the required balance between propulsive efficiency and propulsive mass is supplied to the tool. This can be done by design rules or, as is done in this thesis, by an objective surface.

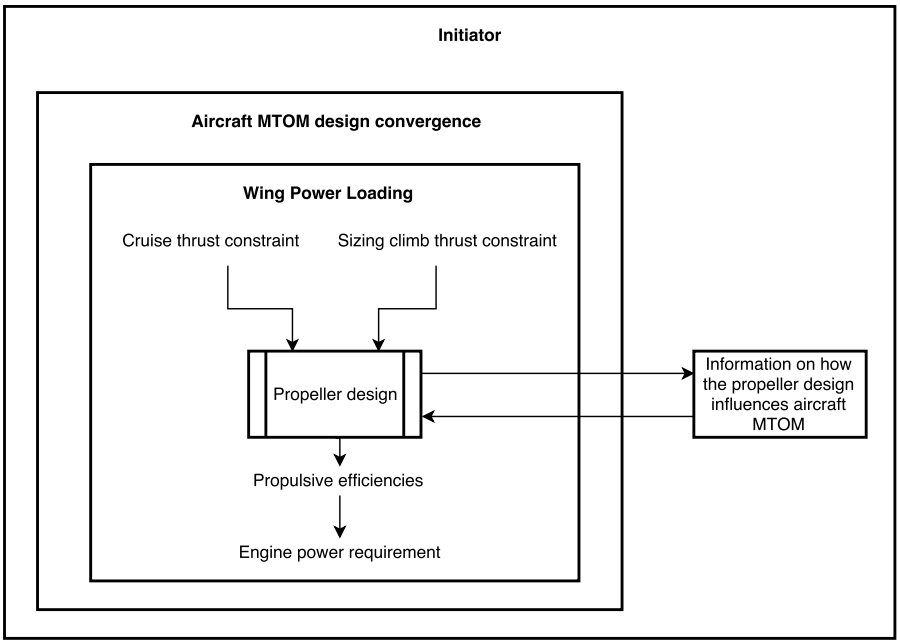

Figure 11.1: Incorporation of propeller design tool in the Initiator.

12

Conclusions and recommendations

The conclusions and recommendations of the research performed in this research are presented in this chapter. Conclusions are stated in Section 12.1 and recommendations for future work are given in Section 12.2.

12.1. Conclusions

Optimization methodology and tools

In this work propeller design for conceptual turboprop aircraft is investigated. The maximum take-off mass (MTOM) of the conceptual turboprop aircraft is selected as a performance metric by which propeller design is evaluated. The MTOM of the turboprop concept is determined in class II design. At this stage of the design basic geometry, performance and weight are determined. This design procedure is automated in an aircraft conceptual design tool "the Initiator", developed conjointly by researchers of the Delft University of Technology. The influence of the propeller on the MTOM of turboprop aircraft at this stage of design is determined as the mass of the propeller as well as the cruise propulsive efficiency and the propulsive efficiency of the propeller in the sizing condition for the engine. This is established as follows:

> The cruise efficiency determines the fuel mass that needs to be carried by the aircraft for it to complete its mission.
>
> Performance requirements established by regulatory agencies dictate a minimal thrust that must be developed in certain flight scenarios in order to ensure the safety of the aircraft. The propulsive efficiency in the critical condition determines the thrust that is developed from the power that is available. Thus, the propulsive efficiency in the critical condition determines the required engine power to meet thrust constraints. The mass of the sized engine together with the propeller and auxiliaries' mass determine the mass of the propulsive unit.

Thereby, the influence of the propeller on MTOM is established as the influence of the propeller on fuel and propulsive unit mass. A design objective is constructed by repeating a class II design convergence for combinations of fuel and propulsive unit mass. In this research the fuel mass is only dependent on the propeller propulsive efficiency in cruise. To optimize a propeller design a set of tools is developed that calculate the propulsive efficiency in cruise and mass of the propulsive unit.

A study into different propeller aerodynamic solvers results in the selection of BEM theory developed by Glauert with a tip correction of Prandtl. It is concluded that this allows accurate calculation of propeller performance for the required operating regimes at acceptable computation times. The airfoil distribution along the propeller blade radius is included in the design optimization of the propeller. For the aerodynamic polars of the airfoils to be available rapidly, a curve fitting model is used. The lift and drag curves are collected in a database. The lift polar $c_{l_{max}}$ is corrected for delayed separation experienced by rotor airfoils. The model used for this correction is developed by Snell et al. for wind turbine airfoils. It is concluded that no suitable model for the post $c_{l_{max}}$ development of lift and drag exists. Therefore, an assumption for the development is made. A structural constraint is implemented by placing a limit on the root normal stress. This limit is determined from a reference case. The mass of the propulsion unit is defined as the summation of masses of the following components: gas turbine, gearbox, propeller, nacelle and auxiliary systems. The gas turbine and propeller

mass are determined by a regression line established from reference designs. Remaining components are determined from equations established by other researchers. The take-off field length(TOFL) is identified as a potentially sizing condition for the propulsive mass. A study into the empirical methods for determining the TOFL concluded that the available methods are of to low fidelity for propeller design. A method for simulating the take-off is established and used to asses the take-off performance of propeller designs.

The established tools, analysis methods and conclusions allows the following research question to be answered:

What propeller design parameters are relevant and feasible to include in the propeller design space?

The design parameters of the propeller follow from the selection of the aerodynamic solver. The propeller can be described by B number of blades. The propeller with diameter has its blades radius divided into a number of aerodynamic sections. For each aerodynamic section the geometric pitch angle and chord length is determined. The research performed to determine an aerodynamic model to describe the aerodynamic sections concluded that the thickness of and camber of the aerodynamic section is relevant and feasible to include. These two parameters are selected as they are the major contributors to the variance of lift and drag polars. A study into the number of blade sections concluded that it is favourable for the accuracy of the BEM tool to locally increase the number of sections describing the blade around 0.75% radius. The number of aerodynamic sections used in this research is set to 5. This number is chosen as it results in minimal computation time with an inaccuracy of approximately 2%.

The developed methodology determined the entire mass of the propulsive unit as an optimization variable. The propulsive unit consist of the propeller and an engine together with systems supporting both. The engine is described as a gas turbine and a gearbox. This differentiation is made because the rotational rate rpm is included in the propeller parameterization. The rpm has an influence on the aerodynamic performance of the propeller as well as the mass of the gearbox. Finally the engine mass is included in the design parameterization. The engine mass is derived from the maximum take-off engine power.

The propeller design parameters and an optimization objective are known. A reference case for these parameters is established from which the optimality of new designs is determined. A number of optimization procedures are used to draw further conclusions on the relevance of design parameters. A number of gradient descent optimization are performed and it is concluded that the initial conditions have a large impact on the optimum reached. This leads to the conclusion that it is easy to arrive at a local optima for the propeller design. A global optimization using a genetic algorithm is employed to make definitive statements on the optimality of the results. The aerodynamic model of the blade sections is evaluated and it is concluded that it is of little significance to the results if a good set of initial airfoils is chosen for the propeller.

A conclusion regarding the role of the design objective on the optimization result is formed by modifying the objective. Setting the objective to have optimal propulsive efficiency in the critical climb condition results in a propeller with large diameter and a heavy propulsive unit and a non-optimal propeller design. Setting the objective for propulsive efficiency in the cruise condition and performing a gradient descent optimization results in a lower MTOM compared to an optimization which has its MTOM set as design objective. The reason for this is believed to be a better optimization stability. A genetic optimization produces the most optimal designs and has as an advantage that the number of blades can be included in the optimization routine and do not have to be selected by the designer. By performing genetic optimizations it is concluded that the blade number has a causal relation ship with the blade diameter and the aspect ratio of the propeller blade.

A study into the design objective and optimization paths revealed that it is improbable that the developed methodology results in a propeller design with an optimal aircraft MTOM. By evaluating all points considered during an optimization for optimal cruise efficiency the best propeller design of all performed optimizations is found. This is not the design with optimal cruise efficiency but a design found during the search for an optimal cruise efficiency. An investigation of the design space and the points considered during this optimization shows that there is a good density of points considered near optimal cruise efficiency. But it cannot be concluded that the global optimum is reached.

The influence of design parameters: blade activity factor, number of blades and diameter is determined. These factors are chosen as they are of large influence on the propeller performance by determining the blade shape, its aspect ratio and thereby the aerodynamic performance. The increase of the blade aspect ratio is

found to be detrimental to the mass of the propulsive unit.

A sensitivity study performed for the take-off field length requirement shows that the take-off power is the main parameter of influence. The optimization routine prioritized sizing the engine power to meet the TOFL constraint. The geometry of the propeller is subservient to the take-off power in satisfying the TOFL constraint.

The results of the optimization routines and the established dependence of propeller design parameters on optimality allows the following research questions to be answered:

What level of of improvement can be expected from a propeller and propulsion optimization routine?

What is the influence of the propeller design parameters on the sizing of the propulsive unit and the maximum take-off mass of a conceptual turboprop aircraft?

The influence of propeller parameters on MTOM is a complicated relationship between aerodynamic performance and mass of the propulsive unit. An optimization routine must be used to find the best propeller design. It is concluded that a gradient descent optimization is poorly suited for propeller optimization. This type of optimization is prone to getting stuck in a sub-optimal local minima. The improvements found by this type of optimization are therefore relatively small. Global optimizations are performed to explore the propeller design range and used to make statements on the level of expected improvements obtained by an optimization routine with some confidence. The range of improvement in MTOM is determined to be less then 1% when compared to estimations by handbook methods or a reference propeller. The prediction of the fuel mass and propulsive mass are found to differ between -5% and +7.5% respectively when compared to the handbook method of Torenbeek. However if a reference propeller is used for the sizing, the prediction of these masses is already significantly improved.

12.2. Recommendations

Overall it is possible to improve the predictions made by the tools, establish a design objective of higher fidelity and increase the confidence of the optimization. The following is recommended for further research:

- Improve the structure tool by calculating the stress in the entire blade as well as incorporating all forces on the blade both steady state and dynamic.
- Increase the accuracy of the aerodynamic module by implementing a better aerodynamic model for the airfoil sections which corrects the drag as well as the lift for the radial effects in the boundary layer. Furthermore, it is recommended that the assumption for the development of lift and drag past $c_{l_{\max}}$ is further investigated and improved. Finally, the implementation of corrections for installation effects as well as incorporation of the propeller inflow angle when in climb.
- The mass estimation module has large dependence on the power of the engine. The mass of most components is derived from a relationship with engine power. The effect this has on the optimization routine is not investigated. A physical determination derived from the forces on each component will increase the confidence of the mass estimation.
- Perform an optimization routine for the take-off field length for the currently assumed take-off variables.
- The objective for the optimization can be improved by incorporating the changes the propeller geometry has on the aircraft. This will improve the prediction of the relationship between propeller diameter and aircraft mass. This relationship is present because the y-axis position of the engine on the wing sizes the empennage. In addition, the effects of the propeller slipstream contribute to this and could be incorporated.
- The optimization routine can be improved by changing the methodology to avoid unfeasible points, this will aid optimizer stability. Further, the optimization objective for global optimizations does not sample the entire design space. A new optimization objective can remedy this. Investigating if it is possible to merge two optimization routines, one for maximum cruise propulsive efficiency another for minimal propulsive mass could provide further confidence in that proper sampling of the design space is performed. Custom mutation and crossover functions can aid the genetic algorithm further in finding designs.

- In this thesis only one mission type is evaluated. Furthermore, the fuel burn in climb, decent and loiter is estimated with an empirical relation. Studying the influence of the mission type on the propeller design can provide further insights in the propeller design process.

Bibliography

[1] ATR. *ATR FAMILY Brochure*. http://www.atraircraft.com/products_app/media/pdf/FAMILY_septembre2014.pdf. Accessed: March, 2017.

[2] E. Torenbeek. *Synthesis of Subsonic Airplane Design*. Springer Netherlands, 1982.

[3] J. Roskam. *Airplane design*. DARcorporation, 1985.

[4] D. P. Raymer. *Aircraft design: A conceptual approach*. American Institute of Aeronautics and Astronautics, 1999.

[5] J.Y. Boersma. "Business Jet Design Using Laminar Flow". MA thesis. Delft University of Technology, 2016.

[6] Engineering Sciences Data Unit. *Estimation of cruise range: Propeller-driven aircraft*. Tech. rep. 1975.

[7] Engineering Sciences Data Unit. *Lost Range, Fuel and Time Due to Climb and Descent: Propeller-driven Aeroplanes*. Tech. rep. 1977.

[8] E. Torenbeek. *Advanced Aircraft Design*. John Wiley & Sons, 2013.

[9] P. P. Walsh and P. Fletcher. *Gas turbine performance*. John Wiley & Sons, 2004.

[10] B. Gunston. *Jane's aero-engines*. Jane's Information Group, 2006.

[11] E. S. P. Branlard, K. Dixon, and M. Gaunaa. "An improved tip-loss correction based on vortex code results". In: *Proceedings of EWEA 2012 - European Wind Energy Conference & Exhibition*. 2012.

[12] J. F. Manwell, J. G. McGowan, and A. L. Rogers. *Wind energy explained: theory, design and application*. John Wiley & Sons, 2010.

[13] O. Gur and A. Rosen. "Comparison between blade-element models of propellers". In: *Aeronautical Journal* 112.1138 (2008), p. 689.

[14] Y. Teeuwen. *Propeller modelling and optimization integration in conceptual aircraft design*. Literature Study, Delft University of Technology, 2016.

[15] L. Prandtl. *Applications of Modern Hydrodynamics to Aeronautics. [in Two Parts]*. Tech. rep. 113. NACA, 1923.

[16] A. Betz. "Schraubenpropeller mit geringstem Energieverlust. Mit einem Zusatz von L. Prandtl". In: *Nachrichten von der Gesellschaft der Wissenschaften zu Göttingen, Mathematisch-Physikalische Klasse* (1919), pp. 193–217.

[17] O. Anaya-Lara et al. *Wind energy generation: modelling and control*. John Wiley & Sons, 2011.

[18] T. Burton et al. *Wind energy handbook*. John Wiley & Sons, 2011.

[19] S.F. Ramdin. "Prandtl tip loss factor assessed". MA thesis. Delft University of Technology, 2017.

[20] S. Goldstein. "On the vortex theory of screw propellers". In: *Proceedings of the Royal Society of London. Series A, Containing Papers of a Mathematical and Physical Character*. Vol. 123. 792. 1929, pp. 440–465.

[21] T. Theodorsen. *Theory of propellers*. Vol. 3. McGraw-Hill, 1948.

[22] V. L. Okulov and J. N. Sørensen. "Optimum operating regimes for the ideal wind turbine". In: *Journal of Physics: Conference Series*. Vol. 75. 1. 2007, p. 12009.

[23] H. Glauert. "Airplane propellers". In: *Aerodynamic theory*. Springer, 1935, pp. 169–360.

[24] C. N. Adkins and R. H. Liebeck. "Design of optimum propellers". In: *Journal of Propulsion and Power* 10.5 (1994), pp. 676–682.

[25] E. E. Larrabee. *Practical design of minimum induced loss propellers*. Tech. rep. SAE, 1979.

[26] N. van Arnhem. "Design and Analysis of an Installed Pusher Propeller with Boundary Layer Inflow". MA thesis. Delft University of Technology, 2015.

[27] M. Drela and H. Youngren. *XROTOR user guide*. http://web.mit.edu/drela/Public/web/xrotor/xrotor_doc.txt. Accessed: November, 2016.

[28] Nationaal Lucht en Ruimtevaartlaboratorium. *N250 propeller Shoptest*. Tech. rep. NLR, 1993.

[29] W Mason. "Analytic models for technology integration in aircraft design". In: *Aircraft Design, Systems and Operations Conference*. 1990, p. 3262.

[30] O. Gur, W. H. Mason, and J. A. Schetz. "Full-configuration drag estimation". In: *Journal of Aircraft* 47.4 (2010), pp. 1356–1367.

[31] J. Dorfling and K. Rokhsaz. "Constrained and unconstrained propeller blade optimization". In: *Journal of Aircraft* 52.4 (2014), pp. 1179–1188.

[32] J. Stack. *Tests of airfoils designed to delay the compressibility burble*. Tech. rep. TN 976. NACA, 1943.

[33] C Lindenburg. "Modelling of rotational augmentation based on engineering considerations and measurements". In: *Proceedings of the European Wind Energy Conference*. 2004.

[34] W.A. Timmer and C. Bak. *Advances in wind turbine blade design and materials: 4. Aerodynamic characteristics of wind turbine blade airfoils*. Elsevier, 2013.

[35] H Himmelskamp. "Profiluntersucchungen an einem umlaufenden propeller". PhD thesis. Max-Planck-Inst. für strömungsforschung, Göttingen, 1950.

[36] R.P.J.O.M. van Rooij, A. Bruining, and J.G. Schepers. "Validation of some rotor stall models by analysis of the IEA Annex XVIII field data". In: *Proceedings of EWEC European Wind Energy Conference Madrid*. 2003.

[37] J.G. Schepers and R.P.J.O.M. van Rooij. "Final report of the Annexlyse project: Analysis of aerodynamic field measurements on wind turbines". In: *Wind Energy* (2005).

[38] S. Breton, F. N. Coton, and G. Moe. "A study on rotational effects and different stall delay models using a prescribed wake vortex scheme and NREL phase VI experiment data". In: *Wind Energy* 11.5 (2008), pp. 459–482.

[39] L.W. Traub. "Simplified propeller analysis and design including effects of stall". In: *The Aeronautical Journal* 120.1227 (2016), pp. 796–818.

[40] R Göran. "Static pressure measurements on a rotating and a non-rotating 2.375 m wind turbine blade. Comparison with 2D calculations". In: *Journal of Wind Engineering and Industrial Aerodynamics* 39.1-3 (1992), pp. 105–118.

[41] Mark Drela and H Youngren. "XFoil subsonic airfoil development system". In: *Software Package, available online at htt p://web. m it. edu/drela/Public/web/xfoil [retrieved May. 2016]* (2004).

[42] R.P.J.O.M. van Rooij. *Modification of the boundary layer calculation in RFOIL for improved airfoil stall prediction*. Tech. rep. IW-96087R. Delft University of Technology, 1996.

[43] L. E. Fogarty. "The laminar boundary layer on a rotating blade". In: *Journal of the Aeronautical Sciences* (1952).

[44] Engineering Sciences Data Unit. *Aerofoil maximum lift coefficient for Mach numbers up to 0.4*. Tech. rep. 1999.

[45] I. H. Abbott and A. E. von Doenhoff. *Theory of wing sections*. Dover Publications, 2012.

[46] R. E. Sheldahl and P. C. Klimas. *Aerodynamic characteristics of seven symmetrical airfoil sections through 180-degree angle of attack for use in aerodynamic analysis of vertical axis wind turbines*. Tech. rep. Sandia National Labs., Albuquerque, NM (USA), 1981.

[47] B. Montgomerie. *Drag Coefficient Distribution on a Wing at 90 Degrees to the Wind*. Ecn-c-95-061, Netherlands Energy Research Foundation, ECN, 1996.

[48] J. Dorfling and K. Rokhsaz. "Non-Linear Aerodynamic Modeling of Airfoils for Accurate Blade Element Propeller Performance Predictions". In: *32nd AIAA Applied Aerodynamics Conference*. 2014, p. 2998.

[49] L. K. Loftin Jr. *Subsonic Aircraft: Evolution and the Matching of size to Performance*. Tech. rep. NASA-RP-1060. NASA, 1980.

[50] W. F. Phillips. *Mechanics of flight*. John Wiley & Sons, 2004.

[51] G.J.J. Ruijgrok. *Elements of airplane performance*. 1990.

[52] E. Obert. *Aerodynamic design of transport aircraft*. Ios Press, 2009.

[53] M. F. Niţă. *Aircraft design studies based on the atr72*. Project work towards a thesis, Hochschule für Angewandte Wissenschaften Hamburg, 2008.

[54] Fokker. *Fokker 50 basics*. http://www.flyfokker.com/sites/default/files/FLYFokker/FlyFokker_PDF_Fokker50_Basics.pdf. Accessed: March, 2017.

[55] Fokker. *Fokker 50 performance*. http://www.flyfokker.com/sites/default/files/FLYFokker/FlyFokker_PDF_Fokker50_Performance.pdf. Accessed: March, 2017.

[56] European Aviation Safety Agency. *TYPE CERTIFICATE DATA SHEET - Pratt & Whitney Canada - PW100 series*. Tech. rep. 2014.

[57] A. Filippone. *Advanced aircraft flight performance*. Cambridge University Press, 2012.

[58] Engineering Sciences Data Unit. *Undercarriage drag prediction methods*. Tech. rep. 79015. 1987.

[59] Engineering Sciences Data Unit. *ESTIMATION OF DRAG ARISING FROM ASYMMETRY IN THRUST OR AIRFRAME CONFIGURATION*. Tech. rep. 88006. 1988.

[60] R.J. Schoustra. "Modelling and Analysis of a Ground Assisted Take-off for Commercial Aircraft". MA thesis. Technical University Delft, 2013.

[61] E.P. Hartman and D. Biermann. *The aerodynamic characteristics of full-scale propellers having 2, 3, and 4 blades of Clark y and RAF 6 airfoil section*. Tech. rep. 640. NACA, 1938.

[62] O. A. Bauchau and J. I. Craig. *Structural analysis: with applications to aerospace structures*. Springer, 2009.

[63] J. Sodja et al. "Design of flexible propellers with optimized load-distribution characteristics". In: *Journal of Aircraft* 51.1 (2014), pp. 117–128.

[64] T. Beléndez, C. Neipp, and A. Beléndez. "Large and small deflections of a cantilever beam". In: *European Journal of Physics* 23.3 (2002), p. 371.

[65] T. H. G. Megson. *Aircraft structures for engineering students*. Elsevier, 2012.

[66] H.J. Sommer. *Polygeom*. https://nl.mathworks.com/matlabcentral/fileexchange/319-polygeom-m. Accessed: November, 2016.

[67] R Soerjadi. "On the Computation of the Moments of a Polygon, with Some Applications". In: *Heron* 16.5 (1968), pp. 43–58.

[68] J. W. R. Taylor and P. Jackson. *Jane's All the World's Aircraft*. Jane's Publishing Company, 1995.

[69] W. Johnson. *NASA Design and Analysis of Rotorcraft*. Tech. rep. TP–2009-215402. NASA, 2015.

[70] C. Havey and M. Kline. "Propulsion optimization for conceptual STOVL aircraft". In: *Aircraft Design and Operations Meeting*. 1989, p. 2020.

[71] R.M. Plencner, P. Senty, and T.J. Wickenheiser. *Propeller performance and weight predictions appended to the Navy/NASA engine program*. Tech. rep. NASA-TM-83458. NASA, 1983.

[72] R.J. Willis. "New equations and charts pick off lightest-weight gears". In: *Product engineering* 5 (1963), pp. 64–75.

[73] P. Lolis. "Development of a Preliminary Weight Estimation Method for Advanced Turbofan Engines". PhD thesis. Cranfield University, 2014.

[74] European Aviation Safety Agency. *TYPE CERTIFICATE DATA SHEET - Dowty Propellers - R408 series propellers*. Tech. rep. March 2008.

[75] C. A. Negulescu. "Airbus AI-PX7 CROR design features and aerodynamics". In: *SAE International Journal of Aerospace* 6.2013-01-2245 (2013), pp. 626–642.

[76] Fred Ernest Weick. *Aircraft propeller design*. McGraw-Hill Book Company, inc., 1930.

[77] ATR. *Flight crew operating manual ATR42 Model: 500*. https://www.scribd.com/doc/86840836/FCOM-ATR42-500. Accessed: September, 2017.

[78] D. Scholz and M. Niţă. "Preliminary sizing of large propeller driven aeroplanes". In: *Czech Aerospace Proceedings* 2 (2009), pp. 41–47.

A

Propeller speed governing

Most turboprop and powerful piston propeller aircraft allow for the propeller to be pitched in flight. The geometric pitch angle β of the blades is changed to adjust the propeller blade to the varying free stream speed U_∞ of the aircraft. This change in pitch angle ensures an optimal angle to the relative velocity on the blade.

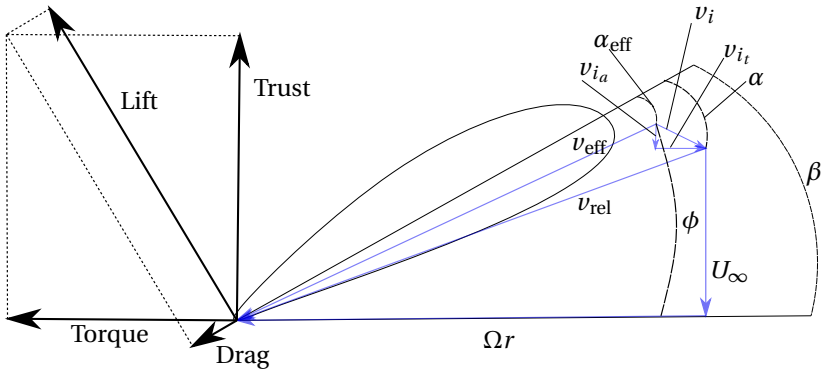

Figure A.1: Sketch of a propeller blade 2D cross section.

The scheduling of the pitch can be done in a number of ways. The prevalent operation is that a control loop governs the propeller pitch to absorb changes in power at a constant rotational rate. This allows the power plant and propeller to operate at their most efficient speed. Power changes are accomplished by changing the turbine inlet temperature through fuel flow. The increased energy available at the turbine is available to the propeller as an increase in torque. This is absorbed by the propeller by pitching the blades, increasing the effective angle of attack on the propeller sections. Thereby, the thrust of the propeller can be increased without increasing the rotational rate of the propeller or the turbine.

The pitch governing mechanism of the ATR42-500 is used to model a pitch governing method for this research. Variations in pitch governing between aircraft exist. This control scheme is selected because the ATR42-500 aircraft uses a PW100 series power plant. In addition the flight crew operating manual (FCOM) is available online and has a good description of the pitch scheduling mechanism.

A.1. ATR42-500 propeller governing

The power control parameter of the ATR42-500 propulsive unit is the torque Q:

$$Q = \frac{P}{\omega} \tag{A.1}$$

The toque is calculated for each flight condition and displayed to the flight crew. The torque delivered is a function of the fuel flow. The fuel flow is controlled by the power lever, the power management selection

condition (TO, MCT, CLB, CRZ) and the engine bleed. The power management selection is set by the pilot depending on the flight segment. This setting determines the propeller rpm that will be maintained. The TO, Take-off and MCT, maximum continued thrust setting, maintain the propeller at 100% rpm. Reserve take-off power (RTO) is selected automatically if one engine fails during take-off and is equal to MCT. For the CLB, climb and CRZ, cruise the propeller rpm is maintained at 82%.

The required propeller rpm is maintained by a hydraulic pitch change mechanism. The power lever angle is used together with flight conditions to predict the pitch angle required by the propeller to absorb the set torque. If the power lever is moved the propeller is pitched to absorb the expected torque and at the same time fuel flow to the engine is changed according to the power lever. A blade angle positive feedback to the propeller pitch control unit ensures the propeller rpm is maintained at the level of the power management selection. The pitch governing of the ATR42-500 is simplified in Diagram A.2. For more information on the pitch governing and detailed control diagrams the reader is referred to the FCOM[77].

Note: At low power and low flight speed the system operates in transition mode, which allows propeller speed to fall below set point down to 70.8% rpm. This is allowed to prevent a too low blade pitch angle in flight. On the ground at low speed the propeller is fuel governed to maintain propeller rpm at 70.8%. These flight operations are not applicable to the research in this thesis and are not incorporated in the tools.

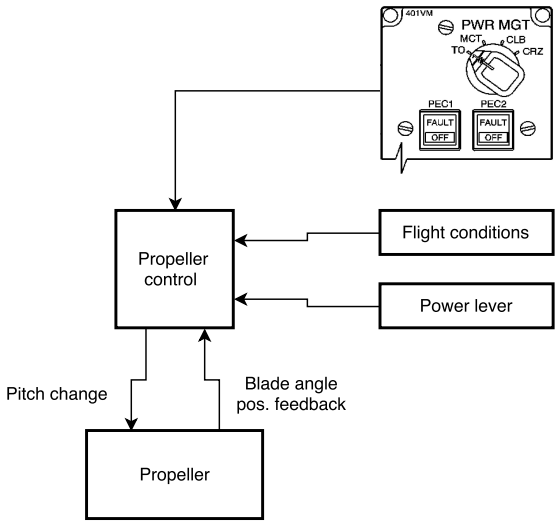

Figure A.2: Simplification of the propeller pitch governing mechanism of the ATR42-500.

A.2. Pitch governing mechanism model

To model the pitch governing mechanisms in the optimization tools the logic explained in the previous section is further simplified. The propeller rpm is maintained at 100% of the rpm design variable for the take-off and climb with OEI condition. For the cruise the propeller rpm is set at 82% of the rpm design variable.

In the optimization Case 1 (see Section 2.2) the engine is sized for one condition. The climb with OEI determines the power requirement of the engine. Because one condition sizes the engine, the blade pitch can be calculated to absorb all power. This is done as follows: the blade pitch angle is set at an arbitrary level for the cruise condition. The optimization routine determines a blade twist distribution to deliver the required thrust in cruise for the set pitch angle. For the climb condition the determined blade twist distribution is pitched relative to the set pitch angle in cruise to deliver the climb thrust requirement. The power requirement of the propeller in this condition is equal to the engine size. Thus, the engine size is not a direct optimization variable. The influence of the engine size and power on the optimization objective is addressed via the sizing climb condition.

Note: Although it is mentioned that the twist angle distribution of the blade is designed for the cruise condition, in reality the optimization routine determines the optimal twist distribution for all conditions at once. The description above is chosen to clarify how the blade pitch angle is determined.

In the optimization Case 2 (see Section 2.2) the sizing condition for the engine is not known. Therefore the engine power is an optimization variable. Again the pitch angle in cruise is set at a fixed level and the blade twist distribution is determined to satisfy the cruise thrust requirement. For the OEI climb and take-off

condition maximum power is used. The maximum available power follows from the optimization variable. In climb or take-off the determined twist distribution is pitched to absorb all available power. This is done as follows: the rpm of the propeller and power available is taken from the design variables. Equation (A.1) is used to calculate the torque available. The propeller blade is given an initial pitch angle and the required torque to spin the propeller is calculated. The difference in torque available and propeller torque is used to establish a pitch angle for which all available torque will be absorbed by the propeller. The performance of the propeller at this pitch angle determines the propeller thrust and efficiency. The pitch governing method used in the optimization tools is depicted schematically in Figure A.3

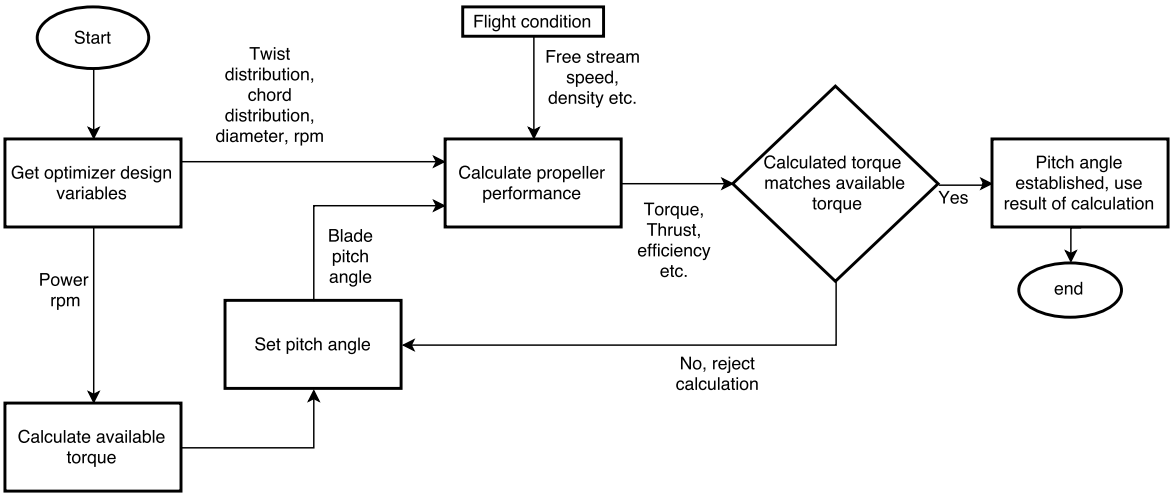

Figure A.3: Pitch governing method used within the optimization routine.

B

Note on the stress relief due to blade bending

The mass estimation tool in this research applies a regression line to determine the propeller mass. Originally the mass of the propeller was to follow from the structure module. The assumption was that a section hollow chord fraction could be made an optimization variable (Figure B.1). The geometric properties of the blade sections could then be used to determine the blade mass. This procedure has not been incorporated due to the performance of the structure module. The structure module determined blade stresses of a very high magnitude. This meant that the optimization routine would result in a very small hollow chord fraction and that subsequently, the blade mass would be overestimated. The reason for the overestimation of stresses is the neglection of the restoring moment generated by the centrifugal forces. In this chapter the restoring moment will be calculated for a blade geometry equal to the verification case of Chapter 8. This is done by first determining the mass of the blade and the generated centrifugal forces. Next, estimating the bending of the blade by simplifying the 3D bending of the blade due to thrust and torque to a 2D representation. The restoring moment, generated by the centrifugal force and the blade bending deflection, is determined for this deflection. The restoring moment generated by the deflection can be reiterated back to the calculation of bending deflection to arrive at the true stresses on the blade with the restoring moment included.

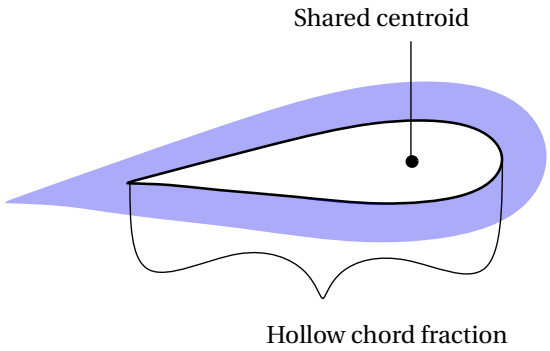

Figure B.1: Definition of the hollow chord fraction on the cross section of a propeller blade element.

B.1. Element mass and centrifugal force

The blade discretization is performed in the same manner as described in Section 6.2. The blade mass can be determined from the section properties. When the area and length of the element are known the mass for each element m_i can be determined by the density of the propeller material chosen. A centrifugal force results from the mass of each element, swung around the hub. The centrifugal force on each node is the summed contribution of all elements that are attached to it and can be computed for each node. The centrifugal force

on the hub, with r_i the radial location of an element's center of gravity, is given as:

$$F_{c_{\text{hub}}} = \sum_{i=1}^{i} m_i (r_i - r_{\text{hub}}) \omega^2 \tag{B.1}$$

The stress due to the centrifugal force is computed as:

$$\sigma_{hub} = \frac{F_{c_{hub}}}{A_{hub}} \tag{B.2}$$

and is added to the bending stress via the superposition principle.

B.2. Description of restorative moment

How a restorative moment is generated by centrifugal force is best explained by imagining a mass on a string. In this example the propeller blade is represented with the string and the thrust acting on the propeller blade is represented by the gravity pulling on the mass. If one starts spinning this mass above one's head the centrifugal force acting on the mass will keep the string taught. The centrifugal force will prevent the mass from hitting the ground under the effect of gravity.

The same effect is significant in relieving the stresses on the propeller blade root. In Sketch B.2 a propeller blade is represented in 2D. The blade bends from its original position in light grey under either a torque or thrust force to a deflected position. If the centrifugal force F_c on a blade element is decomposed, the restorative force $F_{\text{restorative}}$ becomes apparent. This force opposes the thrust and drag. 6.3.2.

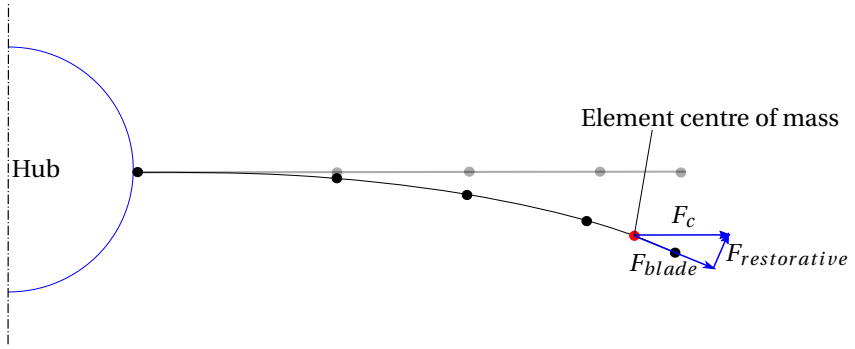

Figure B.2: Bending of a propeller blade and resulting restorative force, represented in 2D.

B.3. Calculation of blade bending displacement

The displacements of the propeller blade are difficult to calculate as the twist and airfoil shape of each element results in a deflection that cannot be predicted with simple Euler beam bending theory. To allow a simple analysis the blade has to be assumed to have no twist. This means that the principle axis of all the blade elements are positioned in the same way. The forces on each node are decomposed along the principle axes of the element cross sections. Then, the deflection for a single element of length L can be calculated from this stiffness matrix:

$$\begin{Bmatrix} F_1 \\ M_1 \\ F_2 \\ M_2 \end{Bmatrix} = (EI) \begin{bmatrix} 12/L^3 & 6/L^2 & -12/L^3 & 6/L^2 \\ 6/L^2 & 4/L & -6/L^2 & 2/L \\ -12/L^3 & -6/L^2 & 12/L^3 & -6/L^2 \\ 6/L^2 & 2/L & -6/L^2 & 4/L \end{bmatrix} \begin{Bmatrix} u_1 \\ \theta_1 \\ u_2 \\ \theta_2 \end{Bmatrix} \tag{B.3}$$

The stiffness matrix can be expanded to calculate the influence of each element upon each other. This is where the simplification of a non twisted blade produces an error. The influence of forces upon other elements is not properly transferred. For an untwisted blade the force vectors are aligned and perpendicular to the principle axis. But for a twisted blade the principle bending axes are not aligned. The deflection of an untwisted blade is calculated by constructing a stiffness matrix containing all elements. And solving for the deflections and angle. With the restorative force calculated from F_{c_i} and the deflection angle θ_i, an iterative approach is followed to determine the ultimate deflection. For the deflection u_{ultimate} the thrust and torque forces on the blade are in balance with the restorative force due to rotation of the blade.

B.4. Simplification of verification case

The distribution of the torque and thrust forces of the verification case are depicted in Figure B.3. The centrifugal forces are not pictured in this figure. To calculate the bending, the forces have to be decomposed on the principle axis of the structural elements. This is shown in Figure B.4. Once the forces are decomposed on the principle axis, the blade is untwisted. By untwisting the blade the bending of the blade can be solved in 2D. The bending over each principle axis is determined separately with the 2D representation of the blade shown in Figure B.2.

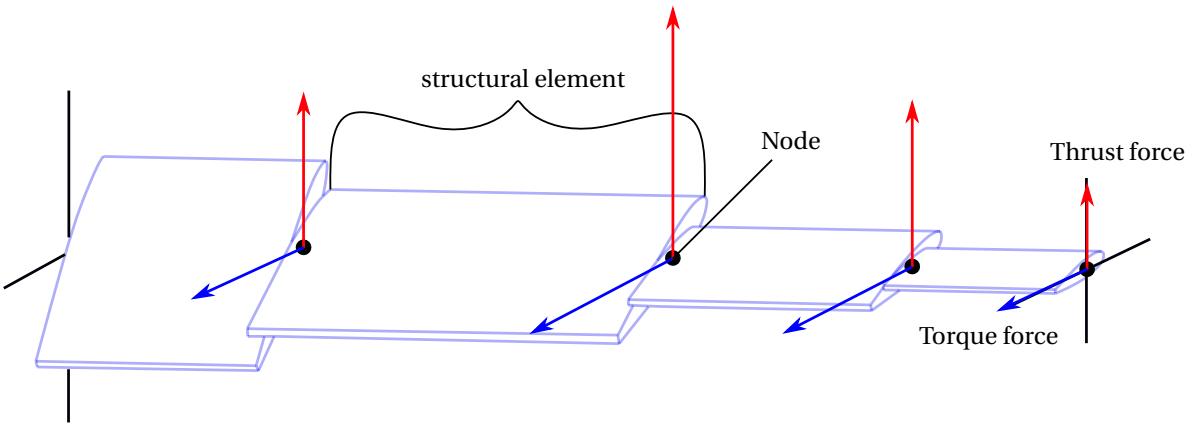

Figure B.3: Blade of the verification case with the thrust force in red and torque force in blue. Not shown is the centrifugal force.

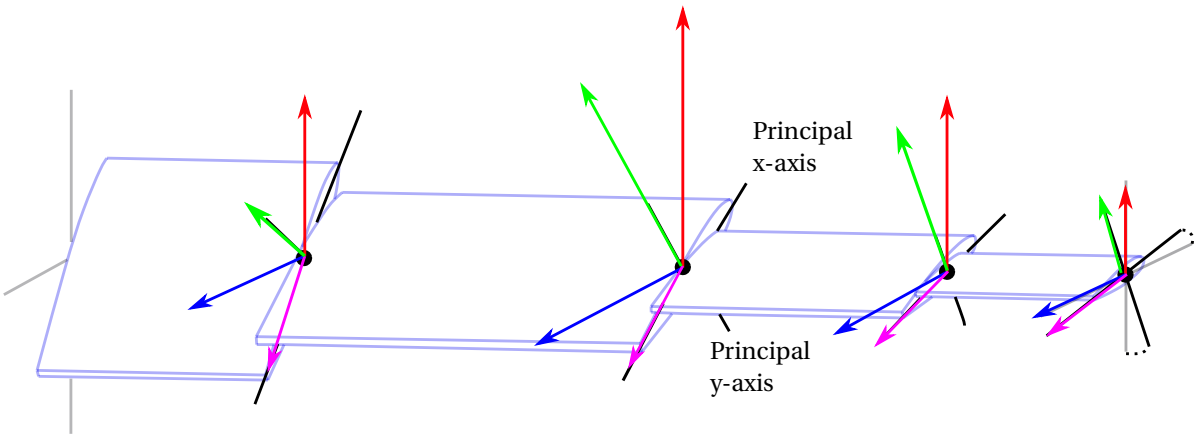

Figure B.4: Blade of the verification case with the thrust force in red and torque force in blue. The decomposition of the thrust and torque of each structural element on the principle x-axis in magenta and the principle y-axis in green.

B.5. Magnitude of stress relief due to bending

In this section the propeller blade deformation is calculated over its principle axis as if the blade has no twist. In reality the force vector of element $i+1$ is acting on an angle with respect to element i. Thereby its magnitude is changed with respect to the principle axis of bending. This reduction is not considered. The magnitude of the error will depend on the twist angle distribution and will increase for a more highly twisted blade.

B.5.1. ANSYS bending results

The magnitude of the error is estimated by the bending results of the verification procedure. The deflection is verified for the Loft FEA and sectional FEA geometry (see Section 8). The bending deflection is determined in ANSYS for Case 2, thrust, torque and centrifugal loads considered. Table B.1 shows the result of the finite

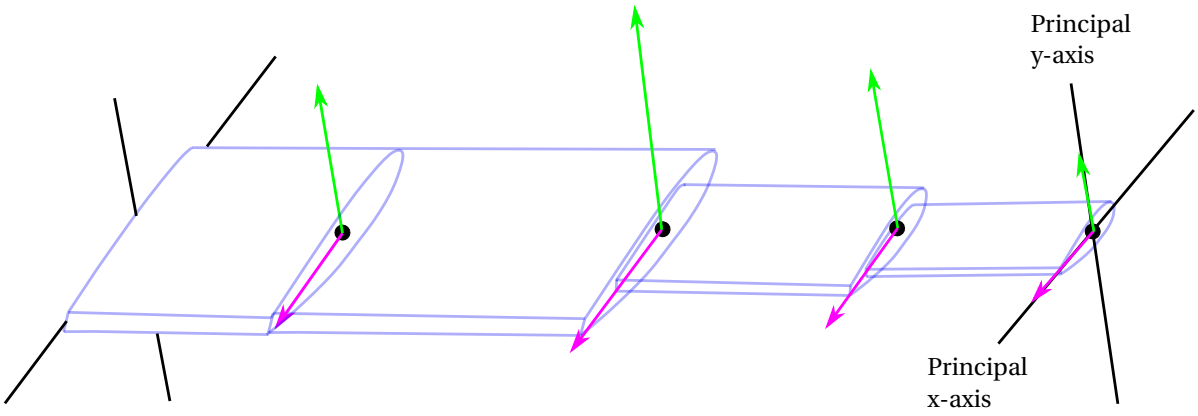

Figure B.5: Untwisted blade for the determination of the bending deflection. The decomposed forces of each structural element on the principle x-axis in magenta and the principle y-axis in green.

element analysis. The Section FEA geometry produces a large deflection, as expected. The Section FEA has a small surface area where the sections connect. This will increase the elongation of the material locally and subsequently produce inaccurate bending results. This result can be explained by Hookes law which states that a change in length may be expressed as:

$$\Delta L = \frac{FL}{AE} \tag{B.4}$$

A decrease in surface area A will result in an increase in elongation ΔL. The bending results of the Section FEA geometry are not thus not reliable. The bending calculation of the Loft FEA is reliable and is used to asses the calculated bending result.

Table B.1: ANSYS bending results for the verification case.

	Loft FEA	Section FEA
Deflection in x [m]	0.123	0.250
Deflection in y [m]	0.132	0.270
Max. deflection in x-y-z-plane [m]	0.180	0.368

B.5.2. Matlab calculation of bending and conclusion on stress relief due to bending

To determine the magnitude of the stress relief the root normal stress for the untwisted blade with the forces in the principle directions is determined as a reference. For this first analysis the effect of bending relief is not included. The forces and geometry of the blade are the same as the reference case of Chapter 8. The moment generated at the blade root by the forces in the principle y direction (see Figure B.5) is 37600 Nm. The maximum and minimum normal stress are given in Table B.2 and the location of the maximum and minimum can be found in Figure B.6a. The deflection of the untwisted blade is given in Table B.3.

For the comparison the restorative forces are included in the calculation with an iterative approach. The calculated restoring moment has a magnitude of 8900 Nm. This means the blade root bending moment experiences a 31% smaller moment then the reference case. This results in a significant relief of blade root stress given in Table B.2. The deflection of the blade is reduced by more than half. The stress relief is of such a large magnitude that it cannot be ignored. A static steady state analysis of the blade stresses is not sufficient for the calculation of magnitude of the blade root stress.

Table B.2: Calculated root normal stress.

	Without bending relief	With bending relief	Δ
Maximum stress [Pa]	5.83×10^8	3.7383×10^8	-36%
Minimum stress [Pa]	-6.05×10^8	-3.96×10^8	-35%

Table B.3: Calculated bending deflection for the 2D propeller blade.

	Without bending relief	With bending relief	Δ
Maximum deflection in y-direction [m]	0.1995	0.071845	-64%

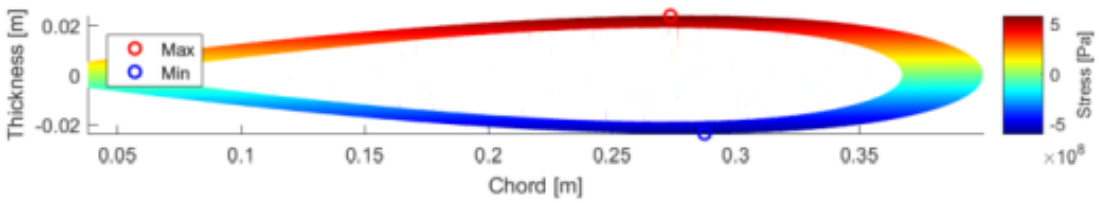

(a) Normal stress on the blade root without bending relief.

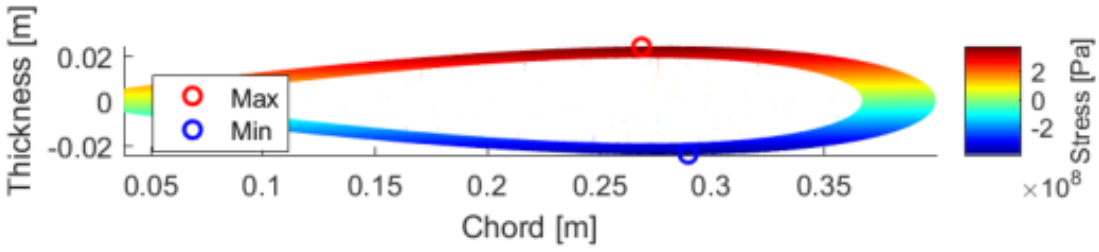

(b) Normal stress on the blade root with bending relief.

Figure B.6: Normal stress on the blade root calculated in Matlab.

C

Empirical estimation of take-off power requirement

Sizing for the take-off requirement can be performed with an empirical formulation. Several researchers have developed methods for determining the engine power required in order to obtain a desired take-off field length.

C.1. Methods

Loftin

Loftin derives the following equation for estimating the take-off field length for jet aircraft [49, p. 111-115]:

$$l_T = \frac{W/S}{(\rho/\rho_0)C_{L_{TO}}(T/W)} \tag{C.1}$$

Whereby Loftin provides curves to match the parameter $\frac{W/S}{(\rho/\rho_0)C_{L_{TO}}(T/W)}$ to a field length. The researcher rewrites this formula to include the power-to-weight ratio instead of the thrust-to-weight ratio under the assumption that the two are proportional to one another.

$$l_T = \frac{(W/S)(W/P)}{(\rho/\rho_0)C_{L_{TO}}} \tag{C.2}$$

Curves for estimating the take-off run are given for the term $\frac{(W/S)(W/P)}{(\rho/\rho_0)C_{L_{TO}}}$, for propeller aircraft. However, the relation made by Loftin is only valid for small general aviation propeller aircraft. The curves established by Loftin are valid for ground runs up to 2000 ft.

Schotls

Schotls alters the equation posted by Loftin and chooses to incorporate the propeller efficiency. The researcher establishes the power required for the take-off field length as:

$$l_T = \frac{k_{TO}V(W/S)(W/P)}{(\rho/\rho_0)C_{L_{TO}}\eta_{p,\,TO}} \tag{C.3}$$

For the efficiency an estimation graph that is posted as a function of the flight speed and the propeller disk loading is used from [53]. The flight speed at which the efficiency is determined is taken as the average flight speed during the take-off run $V_{\text{avg}} = \frac{V_2}{\sqrt{2}}$. Scholts calibrates the function of Loftin with the correction factor $k_{TO} = 1.805\frac{\text{m}^3}{kg}$ for l_T in m. This correction factor is based on large modern turboprops[78]. The validity of taking the average propeller efficiency during the take-off run for the estimation of the power loading is not addressed.

Roskam

Roskam [3] also uses the parameter established by Loftin and calibrates it for the trust loading of a jet aircraft. This thrust loading is then re-calibrated again by statistical data to find the power loading for propeller aircraft up to 3000 SHP. The date and aircraft's used are not specified. With l_T in ft. the power loading is calculated by:

$$C_{\text{jet}} = l_T/37.5 \tag{C.4}$$

$$(T/W) = \frac{(W/S)}{(\rho/\rho_0)C_{L_{TO}} * C_{\text{jet}}} \tag{C.5}$$

$$(W/P) = \frac{2.9}{(T/W)} \tag{C.6}$$

Torenbeek

Torenbeek [8] provides an equation for determining the minimum trust for a given take-off field length.

$$(T/W) = 0.78\left(\frac{N_{\text{eng}}}{0.89N_{\text{eng}} - 1}\frac{W/b^2}{l_T\rho g}\right)^0.5 + \frac{42}{l_T}\frac{N_{\text{eng}}}{0.89N_{\text{eng-1}}} \tag{C.7}$$

This formula has been calibrated by two constants: 0.78 and .89 for l_T in m. Torenbeek states that these constants should be improved with statistical information. The data used for the initial calibration is not given. This formula is used to determine the take-off run in more detail as it separates the air distance and the ground distance (see FAR sec. 25.111) in the calculation. This formula is rewritten to turboprop aircraft in the manor of Scholts and defined as 'Torenbeek1'. In a previous book of Torenbeek [2] an empirical method for determining the mean propeller thrust at $V_{LOF}/\sqrt{2}$ is given as:

$$\overline{T} = 5.75 * P_{TO}\left(\frac{(\rho/\rho_0)N_{\text{eng}}D_p^2}{P_{TO}}\right)^{\frac{1}{3}} \tag{C.8}$$

With P_{TO} in HP and D_p in ft. This is used to derive the power loading from the trust-to-weight ratio of Torenbeek and defined as 'Torenbeek2'.

C.2. Comparison of methods

The methods in section C.1 are used to calculate the required power loading to comply with a take-off field length requirement given in Table C.1. The wing loading and other data required for the equations are taken from the reference aircraft. The data used is given in Table C.1. Loftin's method is not included in the comparison as the empirical data used to calibrate the equation is not valid for the Fokker 50 or ATR72-600. The results of this comparison of the power loading are plotted in Figure C.1& C.2. If it is assumed that the methods determine $\frac{W}{P_{max}}$, the methods of Roskam and Scholts show acceptable agreement with the reference case. These are the methods calibrated for turboprops. Torenbeek's method is not suited for the calculation of turboprops of this size without further calibration with empirical data.

Table C.1: Main aircraft reference data for take-off analysis.

	ATR72-600	Fokker 50
MTOM [kg]	22800 [1]	20820 [52]
$C_{L_{\text{max}}}$ in take-off condition	2.44 [53]	2.2 [52]
Wing span [m]	27.05 [1]	29 [54]
Aspect ratio	12 [1]	12 [54]
Wing surface [m^2]	61 [1]	70 [54]
Take-off field length (MTOM, ISA-SL) [m]	1333 [1]	1190 [55]
Take-off power (normal/max.) [kW]	1846/2051 [1]	1678/1864 [56]
Propeller diameter [m]	3.93 [1]	3.65 [57]

To establish a power loading required for the take-off run an empirical method is not suited. In two methods Scholts and Torenbeek1 the efficiency of the propeller is incorporated. This does allow the propeller geometry to influence the power required for the take-off. However, unlike the requirements that are posed for

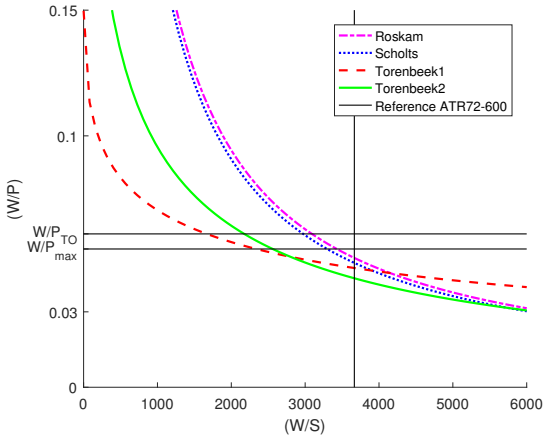

Figure C.1: Power loading calculated for the take-off requirement of the ATR72-600, calculated with data of Table C.1.

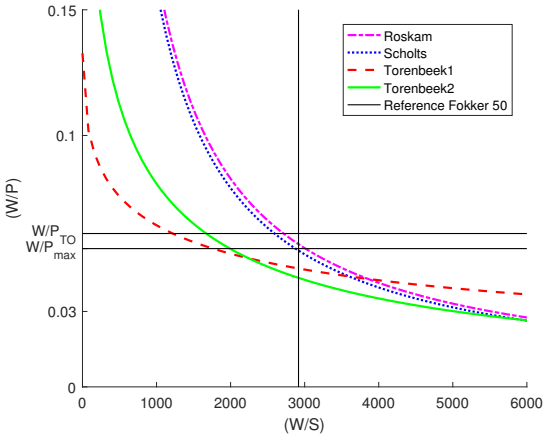

Figure C.2: Power loading calculated for the take-off requirement of the Fokker 50, calculated with data of Table C.1.

Table C.2: Calculated power loading requirement to obtain TOFL stated in Table C.1.

	ATR72-600	**Fokker 50**
Roskam	0.051	0.057
Scholts	0.050	0.055
Torenbeek1	0.048	0.047
Torenbeek2	0.043	0.043
Reference aircraft W/P		
$(W/P_{\max})$	0.055	0.055
(W/P_{TO})	0.061	0.061

a minimum gradient in different conditions the take-off cannot be derived from single condition. The conditions that impact the propeller efficiency vary over the take-off run. The assumption of an average efficiency for the whole run is questionable. Roskam does not incorporate the propeller performance. This makes this method unsuitable for propeller design as it relies purely on statistical calibration and assumes the engine power the only variable for the take-off run. The influence of the propeller is not considered. Torenbeek2 only considers the propeller diameter for the influence of propeller design on the take-off run. Al these methods are of to low fidelity for propeller design Furthermore, most methods use an average thrust to calculate the take-off run. As shown in Table C.1 the turboprop engines have an increase in power 'maximum take-off power' available for 5 minutes in case an engine failure occurs during take-off. It is not specified in any of the methods if this is taken into account nor for which engine power these methods size: normal or maximum take-off power. Table C.2 shows the computed power loading for the different methods. It is concluded that most methods overestimate the power required for the take-off run. This can be seen from the actual power loading of the turboprops. **Note:** The sizing requirement of the engine for the reference aircraft is not known. It is possible that a different performance requirement posed by the FAR determined the engine size.